Title

Environmental Regulation of Cell Differentiation and Behavior in the Choanoflagellate Choanoeca flexa

Author

Reyes-Rivera, Josean M.

Publication Date

2024

Peer reviewed|Thesis/dissertation

Environmental Regulation of Cell Differentiation and Behavior in the Choanoflagellate *Choanoeca flexa*

By

Josean Reyes-Rivera

A dissertation submitted in partial satisfaction of the

requirements for the degree of

Doctor of Philosophy

in

Molecular and Cell Biology

in the

Graduate Division

of the

University of California, Berkeley

Committee in charge:

Professor Nicole King, Chair

Professor Michael Marletta

Professor Dipti Nayak

Professor Noah Whiteman

Spring 2024

Abstract

Environmental Regulation of Cell Differentiation and Behavior in

the Choanoflagellate *Choanoeca flexa*

by

Josean Reyes-Rivera

Doctor of Philosophy in Molecular and Cell Biology

University of California, Berkeley

Professor Nicole King, Chair

The evolutionary transition to complex multicellularity in the animal stem lineage remains a profound mystery. To gain insights into this puzzle, I focused on choanoflagellates, the closest living relatives of animals. Despite their significance, understanding of the environmental factors influencing choanoflagellate evolution, life history, and behaviors remains limited. My doctoral research focused on the characterization of *Choanoeca flexa*, a recently discovered colonial choanoflagellate. This enigmatic microorganism is an example of how, by exploring the diversity of choanoflagellates, we can uncover novel biological phenomena that help us reconstruct the biology of animal progenitors and better understand the origins of animals.

Chapter 1 reviews the history of *C. flexa* as an emerging model organism. *C. flexa* forms monolayered colonies capable of reversible inversions between *flagella-in* and *flagella-out* conformations, each with distinct multicellular behaviors. The colony inversion of *C. flexa* mirrors aspects of embryogenesis and behavioral escape responses in animals. Thus, this system offers a unique platform to investigate the evolutionary mechanisms underlying the origins of animal multicellular development and behavior. Additionally, its reliable presence in splash pools of the Caribbean island of Curaçao provides an opportunity to study its ecology, making *C. flexa* an appealing and promising model for eco- and evo-cell biology.

For the work in Chapter 2, I collaborated with Nuria Ros-Rocher (Pasteur Institute) to characterize the life history of *C. flexa* and its environmental influences. We discovered that *C. flexa* exhibits 'clonal-aggregative development', forming colonies through clonal division, aggregation, or a combination of both. Field and laboratory investigations revealed that *C. flexa* multicellularity is entrained by extreme salinity fluctuations typical of splash pools undergoing evaporation-refilling cycles. Upon gradual evaporation, colonies dissociate into solitary desiccation-resistant cells, which reform colonies after rehydration. We proposed that *C. flexa* clonal-aggregative development may offer a rapid and versatile route to multicellularity, which can be particularly advantageous in ephemeral habitats like splash pools. This discovery blurs

the line between clonal and aggregative multicellularity and expands our notion about the evolutionary trajectory leading to animals.

Finally, in Chapter 3, I demonstrate how studying choanoflagellate multicellular behavior can shed light on ancient animal signaling pathways. Specifically, I explored nitric oxide (NO) signaling in choanoflagellates and found that *C. flexa* and two other species express genes for canonical animal NO signaling. In *C. flexa*, NO induces colony inversion, partially mediated by the secondary messenger cGMP, similar to animals. Moreover, the behavioral output of NO signaling in *C. flexa* – contraction and regulation of feeding and swimming – parallels the effect of NO in certain animal groups. This discovery suggests that NO/cGMP signaling predates animals and may have regulated similar behaviors in their ancestors.

Together, these findings highlight the potential of choanoflagellates, particularly *C. flexa*, as a valuable system for unraveling the mysteries of multicellularity and animal evolution.

Table of Contents

List of Main Figures

Chapter 1

Chapter 2

Chapter 3

Acknowledgments

This journey has been one of profound discovery and growth, made possible by the support of an incredible community. Foremost among them is my advisor, Nicole King. Nicole, your consistency, and mentorship have been instrumental throughout my graduate program; I am profoundly grateful for your guidance and encouragement.

Nicole has guided me in effective science communication and rigorous scientific practice, but her mentorship extended far beyond scientific skill-building. She empowered me to conquer fears and perfectionism, holding a mirror to reveal my capabilities and reminding me of my potential for greatness. Moreover, through her example, she showed me what it means to be true to yourself and pursue joy through self-care in both work and life.

I also extend heartfelt thanks to Thibaut Brunet, who has been like a second mentor. Our shared enthusiasm for the natural world and evolutionary puzzles enriched my journey. Thibaut, thank you for your trust and guidance; you make science an exhilarating adventure.

I am privileged to have collaborated with an exceptional group of individuals who share my passion for science. Chapters 2 and 3 of my dissertation would not have been possible without the contributions of Núria Ros-Rocher, Yang Wu, Benjamin G.H. Guthrie, Michael A. Marletta, Yeganeh Foroughijabbari, Chantal Combredet, Ben T. Larson, Maxwell C. Coyle, Erik A. T. Houtepen, Mark J. A. Vermeij, Thibaut Brunet, and Nicole King. I want to acknowledge the incredible collaboration with Núria in particular; working with you has been a highlight of my graduate career—we are great teammates. Thank you for being an exceptional colleague and friend.

I am also grateful to the current and past members of the King lab, including Alain Garcia de Las Bayonas, Michael Carver, Jacob Steenwyk, Becca Arruda, Chrisa Staikou, Stefany Gonzalez, Flora Rutaganira, Tess Linden, Ben Larson, and David Booth. You have all helped me grow in more ways than you realize.

Additionally, I am deeply grateful to my past mentors, particularly Olga Cordero, Jose E. García-Arrarás, and David Weisblat, who recognized my potential long before I could see it myself.

Furthermore, I thank everyone involved in underrepresented minority (URM) research programs, especially those I participated in: NIH-RISE, NIH-MARC, NSF-REU, SDB Choose-Development, Leadership Alliance, and AMGEM Scholars. The training and exposure I received through these programs are immeasurable and continue to open doors for me. Your belief in a better world and your efforts to make it a reality are deeply appreciated and serve as fuel for my next endeavors.

Beyond the scientific community, I am deeply thankful for the love and support of my friends and family. Special thanks to my older siblings, Elsie and José Gabriel, who have been my life-long role models. My parents, Wanda and José, my aunt Mayra, and my godmother, Vanessa,

all have been pillars of strength, nurturing my well-being and reminding me to embrace imperfection. My heartfelt appreciation goes to my friends and chosen family, including Ana, María María, Victorio, Angel, Kyle, Monica, Caro, Nato, Hector, Pato, Ms. Vee, and many more, for their unwavering support. Lastly, I am grateful to all those who have crossed paths with me, especially the Banner Mountain Collective and my Bay Area queer community, for enriching my life with diverse perspectives and experiences.

Chapter 1

Choanoeca flexa: an emerging model for eco- and evo-cell biology

Introduction

Exploring the long-ignored diversity of microbial eukaryotes can reveal new mechanisms that underpin the evolution of life on our planet. Among this diversity, choanoflagellates stand out as a group of particular interest. As the closest living relatives of animals, they hold the possibility of illuminating the origin of animal cell biology and morphogenesis (Figure 1A) (Carr et al. 2008; Ros-Rocher et al. 2021; Ros-Rocher and Brunet 2023). Additionally, choanoflagellates fill an important ecological niche as one of the primary consumers of bacteria, viruses, and phytoplankton in marine and freshwater environments (Leadbeater et al. 2015).

Although studies of choanoflagellates date back to the mid-1800s, only two species (*Salpingoeca rosetta* and *Monosiga brevicollis*) have been subjected to the types of mechanistic studies historically reserved for animals, fungi, and plants. *S. rosetta* and *M. brevicollis* were each isolated from the environment only once; hence, little is known about their biology and ecology in nature. Instead, a recently discovered choanoflagellate, *Choanoeca flexa*, serves as an experimentally tractable organism that promises to reveal the connections among cell biology, ecology, and evolution in some of the closest living relatives of animals.

The dynamic life history and behaviors of *C. flexa*

C. flexa was serendipitously discovered during a survey of protistan diversity on the Caribbean island of Curaçao in 2018 (Brunet, Larson, and Linden et al. 2019). While examining water samples collected from splash pools on the windward side of the island, Thibaut Brunet, Ben Larson, and Tess Linden observed large multicellular colonies of choanoflagellates that formed a monolayer of polarized cells (a.k.a. “sheets”) (Figures 1B-C). Although the individual cells in these colonies were only ~3 μm in diameter, the sheets attained diameters exceeding 100 μm, comprising hundreds of constituent cells. Upon observing that the sheets could reversibly invert their curvature from convex to concave without separation of the component cells, Brunet, Larson, and Linden named the new species *C. flexa* (Brunet, Larson, and Linden et al. 2019).

As is typical for choanoflagellates, *C. flexa* cells have an ovoid cell body with an apical flagellum surrounded by an actin-filled microvillar collar (together known as the collar complex), features they also share with diverse animal cell types (e.g. epithelial collar cells and choanocyte cells from sponges) (Figures 1D-E) (Leadbeater et al. 2015; Brunet and King 2017; Larson et al. 2019). Cultures of *C. flexa* grown under temperate conditions in the lab contain both free-swimming single cells and multicellular sheets, with the latter being the predominant form. In *C. flexa* sheets, the cells adhere by their collars, imposing a cup-shaped monolayer morphology on the sheet, in which all cells exhibit the same apico-basal cell polarity (Figure 1D) (Brunet, Larson, and Linden et al. 2019). Through collective cell contractions of the component cells, *C. flexa* sheets can undergo reversible transformations (“inversions”) between a *flagella-in* and *flagella-out* conformation (Figure 1F), with each conformation exhibiting distinct behaviors (further discussed in *Sections IV and V*) (Brunet, Larson, and Linden et al. 2019).

C. flexa can also differentiate into a solitary sessile state by building an extracellular attachment structure called the “theca” (Figure 1F). *C. flexa* thecate cells differ from those of most other choanoflagellates by lacking the apical flagellum (Brunet, Larson, and Linden et al. 2019). Physical confinement, such as what might occur upon burial with sediment, causes *C. flexa* to transition into an amoeboid state that displays crawling cell motility (Figure 1F) (Brunet et al. 2021). Finally, under conditions in which evaporation leads to increased salinity, *C. flexa* sheets disassemble into single cells that subsequently differentiate into immotile, non-proliferative cyst-like cells that lack a collar complex (Ros-Rocher and Reyes-Rivera et al. 2024). Upon rehydration, these desiccation-resistant cells undergo a regenerative process: cells regrow their collar complex and regain their motility, proliferative capacity, and ability to form colonies (Figure 1F). The dynamic conversions among these many cell states and behaviors (and probably others that have not been observed) comprise the rich and diverse life history of *C. flexa* (Figure 1F).

Splash pools as field stations for the study of *C. flexa*

C. flexa stands out among choanoflagellates as one of the few species repeatedly found and isolated from the same location since its initial discovery. Its geographic persistence offers a unique opportunity to explore the ecological influences that shape its life history and behavior in both the field and laboratory.

Amidst Curaçao's semi-arid tropical climate with distinct dry and rainy seasons, *C. flexa* inhabits splash pools in the windward-exposed northern part of the island (Figure 1B). Prevailing winds and the rugged terrain of the rocky intertidal habitats foster an abundance of these splash pools. (Figures 1B and 2A). These pools vary considerably in size (ranging from a few centimeters to a few meters) and harbor diverse bacteria and eukaryotes (Figure 2B). Characterized by their cyclical evaporation and refilling cycles, they are intermittently filled by seawater from crashing waves and spray, and can be supplemented by rainwater during the rainy season. Splash pools also experience constant evaporation, which drives fluctuations in salinity and poses the risk of complete desiccation to resident organisms.

Within this dynamic and ephemeral environment, *C. flexa* exhibits remarkable resilience. Field studies revealed the organism's ability to survive complete desiccation: upon rehydration of soil samples obtained from dry splash pools (desiccated up to a week in the field), sheets of *C. flexa* regenerated within two to three days (Figure 2C) (Ros-Rocher and Reyes-Rivera et al. 2024). Laboratory experiments simulating the gradual evaporation of Curaçao splash pools confirmed these observations and provided further details about the life history of *C. flexa*. During exposure to gradual evaporation and increasing salinity, *C. flexa* sheets dissociated into single cells that subsequently differentiated into cyst-like cells that were resistant to osmotic stress and desiccation (Figure 2D). Rehydration of *C. flexa* desiccated samples induced the differentiation of cyst-like cells into flagellated free-swimming cells, which quickly reformed colonies (Figure 2E) (Ros-Rocher and Reyes-Rivera et al. 2024).

In light of both field and laboratory findings, the cyclical evaporation and refilling dynamics of splash pools represent an ecological context for the transition into and out of multicellularity in this species and provide an exciting natural stage for further exploration (Figure 2E).

The unusual and multifaceted colony development of *C. flexa*

C. flexa exhibits an unusual mode of multicellular development, termed “clonal-aggregative multicellularity," in which sheets arise from single cells through either cell division, aggregation of independent cells, or a combination of both (Figure 1F) (Ros-Rocher and Reyes-Rivera et al. 2024). Clonal and aggregative forms of multicellularity have evolved repeatedly across eukaryotic diversity (Lamża 2023) and historically have been perceived as mutually exclusive, each hypothesized to be driven by distinct selective pressures (Grosberg and Strathmann 2007; Brunet and King 2017; John Tyler Bonner 1998; Staps, Van Gestel, and Tarnita 2019). In choanoflagellates, the earliest documented observations of multicellular development trace back to 1867, when James-Clark described the formation of clonal colonies of *Codosiga botrytis* through serial cell divisions. Subsequently, clonal development has been consistently observed among the limited number of choanoflagellate species for which multicellular development has been studied (Brunet and King 2017; Leadbeater 2015; Fairclough, Dayel, and King 2010; Dayel et al. 2011; James-Clark 1867; S.A and S.J 1998; Leadbeater et al. 1983; Hibberd 1975; Pettitt et al. 2002).

Under conditions suitable for proliferation and of low cell density, *C. flexa* can initiate clonal multicellular development from a single founder cell (Ros-Rocher and Reyes-Rivera et al. 2024). Cell division occurs along a lateral axis, consistent with observations in other choanoflagellates. Sister cells maintain attachment to each other through the signature microvillar collar contacts of *C. flexa* colonies. Therefore, clonal divisions within established colonies facilitate colony expansion. However, *C. flexa* sheets can also grow through the integration of free-swimming single cells and small colonies; in these cases, the incoming cells align their apico-basal polarity with the pre-existing sheet (Ros-Rocher and Reyes-Rivera et al. 2024).

Remarkably, aggregation alone is sufficient for colony formation. The susceptibility of *C. flexa* sheets to shear allows us to experimentally dissociate them into single cells. In conditions of high population density, the individual *C. flexa* cells released by sheet dissociation promptly form small aggregates, initially lacking organization. These aggregates subsequently undergo self-organization and, within 24 hours, resolve into colonies exhibiting the characteristic polarized sheet morphology (Ros-Rocher and Reyes-Rivera et al. 2024).

This duality in developmental strategies challenges conventional assumptions regarding multicellularity in choanoflagellates and expands our notion about the evolutionary trajectories of multicellularity on Earth. *C. flexa* clonal-aggregative development may offer a fast and versatile route to multicellularity, which can be particularly advantageous in ephemeral habitats like splash pools (Figure 2E). The rapid establishment of multicellularity suggests inherent advantages for sheets under permissive conditions. Indeed, sheets exhibit greater efficiency at prey capture than free-swimming single cells, likely due to enhanced flow dynamics (Ros-Rocher

and Reyes-Rivera et al. 2024; Fung et al. 2023). The improved feeding capabilities of colonies may stimulate active proliferation, ensuring reproductive success before the onset of adverse conditions such as splash pool evaporation and desiccation (Figure 2E).

Box 1. How does *C. flexa* clonal-aggregative development compare to classical aggregative multicellular models?

Aggregative multicellularity, observed across various eukaryotic lineages (and certain bacteria), has emerged independently multiple times, often as an adaptive response to changing environmental conditions. Compared to clonal development, aggregative development offers rapid establishment of multicellularity, which can be particularly advantageous in fluctuating environments (La Fortezza, Schaal, and Velicer 2022). In the laboratory, certain organisms utilizing aggregative development (e.g., social amoebae) primarily exist in a unicellular state but quickly aggregate when faced with adverse conditions, such as limited nutrient availability (Márquez-Zacarías et al. 2021; Pentz et al. 2020). Chemical cues trigger the aggregation process, culminating in the formation of elevated spore-bearing structure that confer selective advantages (e.g., facilitated spore dispersal). These structures consist of cells in a non-motile, non-proliferative state, waiting to revert into active individual cells when conditions become favorable (La Fortezza, Schaal, and Velicer 2022).

The aggregative development observed in *C. flexa* stands apart from these mechanisms, as it occurs under conditions permissive to feeding, swimming, and proliferation. Contrary to other studied aggregative protists, *C. flexa* colonies transition out of multicellularity in response to harsh environmental conditions, hinting at distinct evolutionary pressures at play (Ros-Rocher and Reyes-Rivera et al. 2024).

Multicellular-to-unicellular transitions in *C. flexa* have only been studied in the context of high salinity. In this scenario, individual cells adopt a desiccation-resistant form that lacks a collar complex, which is essential for colony cohesion in *C. flexa* and likely for feeding as in other choanoflagellates. Thus, the shift to unicellularity in *C. flexa* under high salinity may represent a consequence of an adaptive strategy employed by individual cells to enhance their own survival under this adverse environmental condition.

C. flexa colony architecture and inversion: a link to animal morphogenesis

A fundamental distinction between choanoflagellates and animals lies in the nature of their developmental processes. While animal morphogenesis arises largely from irreversible developmental programs, multicellular development in choanoflagellates is facultative and reversible. One critical animal morphogenetic process involves the coordinated apical constriction of epithelial sheets, resulting in tissue deformations such as bending during gastrulation or neural tube development. Efforts to reconstruct the origins of these complex processes have often looked to simpler multicellular models like volvocales green algae, which exhibit inversion behavior during early development (Brunet and King 2017). However, due to

the considerable evolutionary gap between green algae and animals, establishing direct connections between these developmental programs has been challenging.

The ability of *C. flexa* to reversibly invert its curvature sparked significant interest regarding its potential relationship to animal morphogenetic processes. Colonies of *C. flexa* are composed of cells held together through direct collar-collar interactions, forming a concave monolayer with aligned apico-basal polarity, reminiscent of animal epithelia (Figures 3A-E) (Brunet, Larson, and Linden et al. 2019). This colony architecture is notably different from rosette colonies of the model choanoflagellate *S. rosetta* (Figures 3F-G), where cells are held together by intercellular bridges and attachment to an extracellular matrix (ECM) (Dayel et al. 2011; Larson et al. 2019).

Although microvillar interactions in *C. flexa* seem distinct from the junctional complexes found in animal epithelial sheets, *C. flexa* shares an important molecular feature with animal epithelia. At the base of the collar, cells have an apical actomyosin ring, a cytoskeletal hallmark of some contractile tissues in animals (Figures 3H-I) (Brunet, Larson, and Linden et al. 2019). The coordination of apical actomyosin contraction regulates colony inversion in *C. flexa*, mirroring tissue deformations during animal morphogenesis (Figures 3H-I). During inversion, the actomyosin ring of individual cells contracts, resulting in the opening of their collars (Figure H) (Brunet, Larson, and Linden et al. 2019). It is hypothesized that changes at the cell level contribute to the global change observed during inversion.

In the 1980s, similar observations were made in the choanoflagellate *Choanoeca perplexa*, the sister species of *C. flexa* (Leadbeater et al. 1983). Barry Leadbeater described colonies of *C. perplexa* as a monolayer of cells attached to each other through microvillar contacts, capable of inverting their curvature from concave to convex conformations. However, colony formation was lost in the domesticated cultures of this species soon after, making it impossible to study this behavior further in *C. perplexa*.

Although colony inversion seems to be unique to monolayered colony-forming species of the *Choanoeca* genus, the discovery of apical actomyosin constriction in individual *C. flexa* cells inspired the exploration of this phenomenon in other choanoflagellates. Apical actomyosin constriction is widespread in choanoflagellates and, thus, was likely present in the last common ancestor of animals and choanoflagellates (Brunet, Larson, and Linden et al. 2019). This finding suggests that apical actomyosin-mediated cell constriction evolved before animal origins, although the collective coordination of this process might have evolved independently in choanoflagellates and animals.

Environmental sensing and multicellular behavioral switches: from feeding to swimming

Animal behavior is characterized by the intricate coordination and cooperation among specialized cells and systems. Understanding the origins of such complexity can be partially facilitated by studying the cooperative dynamics and coordinated behaviors of simpler multicellular models, notably that of choanoflagellates. *C. flexa* sheets, like animals, exhibit coordinated responses to environmental cues, wherein they contract and invert (Figure H). This

ability enables *C. flexa* to transition between feeding and swimming states, resembling animal escape responses (Figure H) (Brunet, Larson, and Linden et al. 2019). Thus, this behavior offers an intriguing avenue for exploring the ecological implications of multicellular behavior in a system with less complexity than animals.

The behavioral switch of *C. flexa* — from a feeding to a swimming state — correlates with the orientation of the cells forming the colony in each of the two known colony conformations (Brunet, Larson, and Linden et al. 2019). In relaxed colonies, constituent cells are arranged with their flagella pointing inward (i.e., flagella-in) (Figure 3H), resembling the organization of the choanocyte chamber of some sponges (Figure 1E) (Riisgård et al. 2023). Colonies in this conformation swim slowly and often settle to the bottom of the flask. Like sponge choanocyte chambers, relaxed colonies exhibit enhanced feeding: cells within colonies generate a strong water flow by beating their flagella symmetrically (Ogawa et al. 2024; Fung et al. 2023), thus attracting bacteria to their collars where they are trapped and ultimately phagocytosed. Conversely, colony inversion swaps the arrangement of cells such that their flagella now point outwards (i.e., flagella-out) (Figure 3H) and beat in a distinct asymmetric pattern (Fung et al. 2023). Contracted colonies are active and swim faster but have limited prey-capture capabilities. Thus, colony inversion in *C. flexa* represents a trade-off between feeding and swimming (Brunet, Larson, and Linden et al. 2019).

What triggers colony inversion in *C. flexa*? At least four different types of environmental cues are known to induce colony inversion: light-to-dark transitions (Brunet, Larson, and Linden et al. 2019), the gas molecule nitric oxide (NO), heat shock, and mechanical stimulation (Figure 3H) (Reyes-Rivera et al. 2022). Comprehensive studies elucidating the multisensory-contractile behavior of *C. flexa* will contribute to reconstructing the biology of animal progenitors, shedding light on the evolutionary transitions preceding the emergence of specialized sensory and contractile cells.

Future Research Directions and Open Questions

Much remains to be discovered about the molecular mechanisms and ecological relevance of *C. flexa* colony inversion and mixed clonal-aggregative multicellular development. A deeper understanding will require developing genetic tools, which have only recently been established in *S. rosetta*, *M. brevicollis*, and *Diaphanoeca grandis* (Booth and King 2020; Woznica et al. 2021; Rubiao et al. 2018).

Investigating the mechanism of apical actomyosin constriction and colony inversion in *C. flexa* remains a key priority. Exploring the function of apical constriction in single cells of *C. flexa* and diverse choanoflagellates could provide more insights into its ancient function and its connection to colony inversion in *C. flexa* and morphogenesis in animals. Similarly, another area of interest lies in the ecological relevance of *C. flexa* inversion behavior. For instance, whether phototransduction and mechanosensation are used as predator avoidance mechanisms. Furthermore, understanding the primary input of NO signaling could shed light on adaptive strategies employed by *C. flexa* in response to environmental stimuli. Moreover, the potential

involvement of NO (or other unknown signaling molecules) in intercellular communication within and between colonies for the coordination of inversion presents an intriguing avenue for future research.

Many essential questions regarding the intricacies of *C. flexa* clonal-aggregative multicellular development remain unanswered. For example, is aggregation an active process? If so, what are the signaling molecules? What are the molecular mechanisms that mediate microvillar contacts in sheets? And how do cells align their apico-basal polarity during aggregative sheet development? Moreover, investigating potential kin recognition mechanisms and the presence of cheater mutants could provide insights into social dynamics within colonies and potential evolutionary conflict in *C. flexa*. Furthermore, the exploration of natural genetic diversity and dispersal mechanisms in *C. flexa* may help uncover hidden facets of its life history and ecology. Finally, identifying other selective advantages of multicellularity in *C. flexa* could provide more clues about the adaptive significance of clonal-aggregative multicellularity in its natural environment.

We anticipate ongoing communication between field and laboratory investigations to further elucidate the biology of *C. flexa*. Furthermore, expanding ecological studies may contribute to environmental conservation efforts and enhance our understanding of how protists respond to challenges posed by global climate change.

Figures

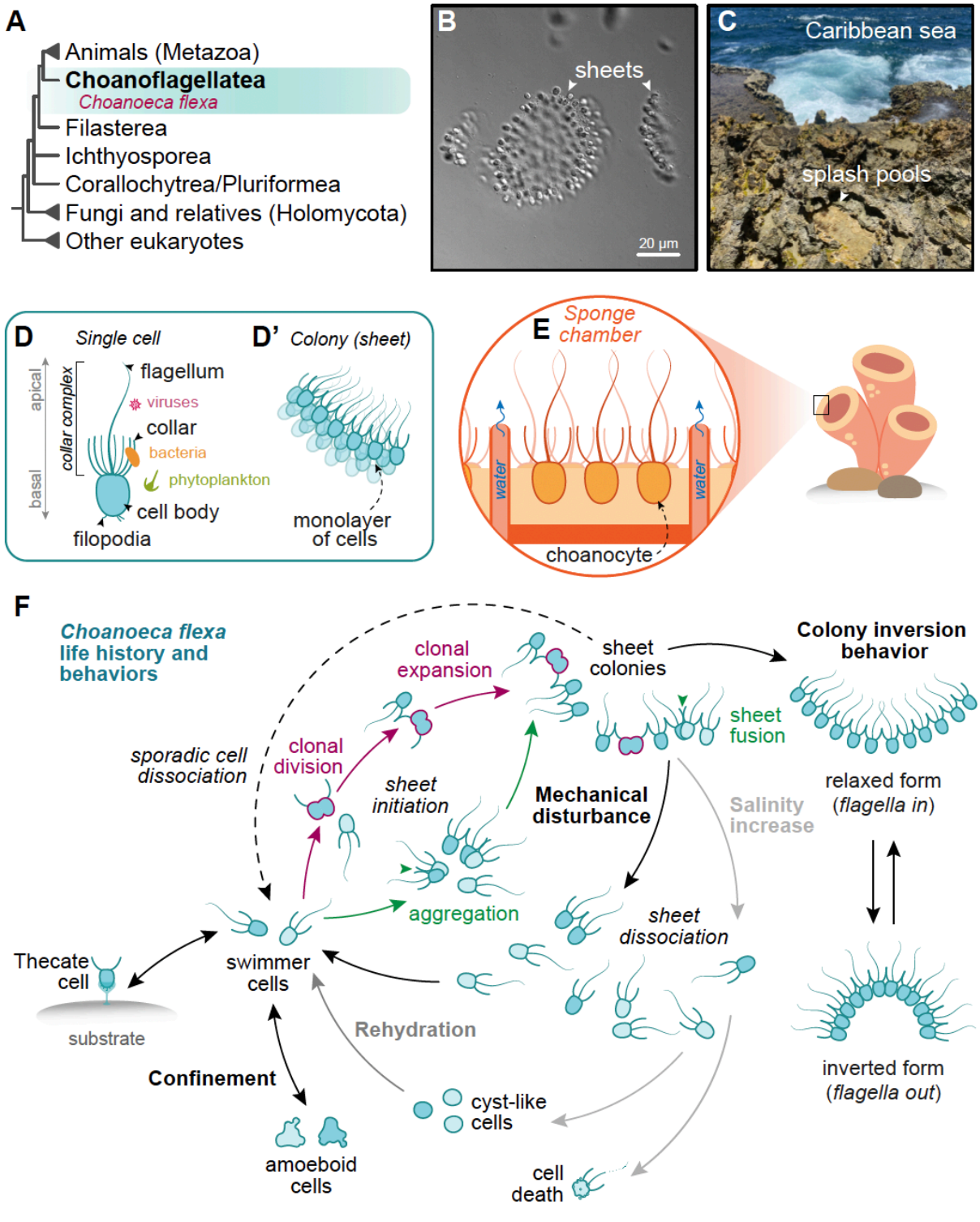

Figure 1.1. *Choanoeca flexa* morphology, habitat, life history, and behaviors.

(**A**) Phylogenetic tree highlighting choanoflagellates as the closest living relatives of animals. (**B**) Brightfield image of *C. flexa* sheets in the relaxed form (white arrowheads). (**C**) Photograph of Curaçao splash pools where *C. flexa* lives (white arrowhead). (**D**) Morphological characteristics of choanoflagellate cells and sheets. Choanoflagellates typically have a round cell body with basal filopodia and an apical flagellum surrounded by an actin-filled microvillar collar (together, the flagellum and collar make up the collar complex). Choanoflagellates are aquatic filter feeders, representing one of the primary consumers of bacteria, viruses, and phytoplankton. (**D'**) *C. flexa* forms polarized monolayer colonies, referred to as "sheets." (**E**) Choanocyte cells of sponges, like choanoflagellates, have a collar complex that they use for filter-feeding. (**F**) The life history and behaviors of *C. flexa*. *C. flexa* cells can form sheet colonies by clonal division, aggregation, or a combination of both. Sheets interconvert between two main conformations: the relaxed form (flagella-in) and the inverted form (flagella-out). Sheet colonies can dissociate into single cells by mechanical disturbance or sporadic cell dissociation (unknown cause). Moreover, under gradually increased salinity that occurs during splash pool evaporation, *C. flexa* sheets dissociate into single cells that later differentiate into cyst-like cells that lack a collar complex. (Some cells experience cell death in this condition.) Upon rehydration of cyst-like cells, they regain their collar complex and ability to form colonies. *C. flexa* can also differentiate into thecate cells, a sessile cell state characterized by an extracellular matrix structure used for attachment to substrates (called the 'theca'). Unlike other choanoflagellates, thecate cells of *C. flexa* lack an apical flagellum. Finally, when subjected to confinement, *C. flexa* transitions into an amoeboid state with crawling abilities. Schematics from panels A, D, and F were adapted from Ros-Rocher and Reyes-Rivera et al. 2024.

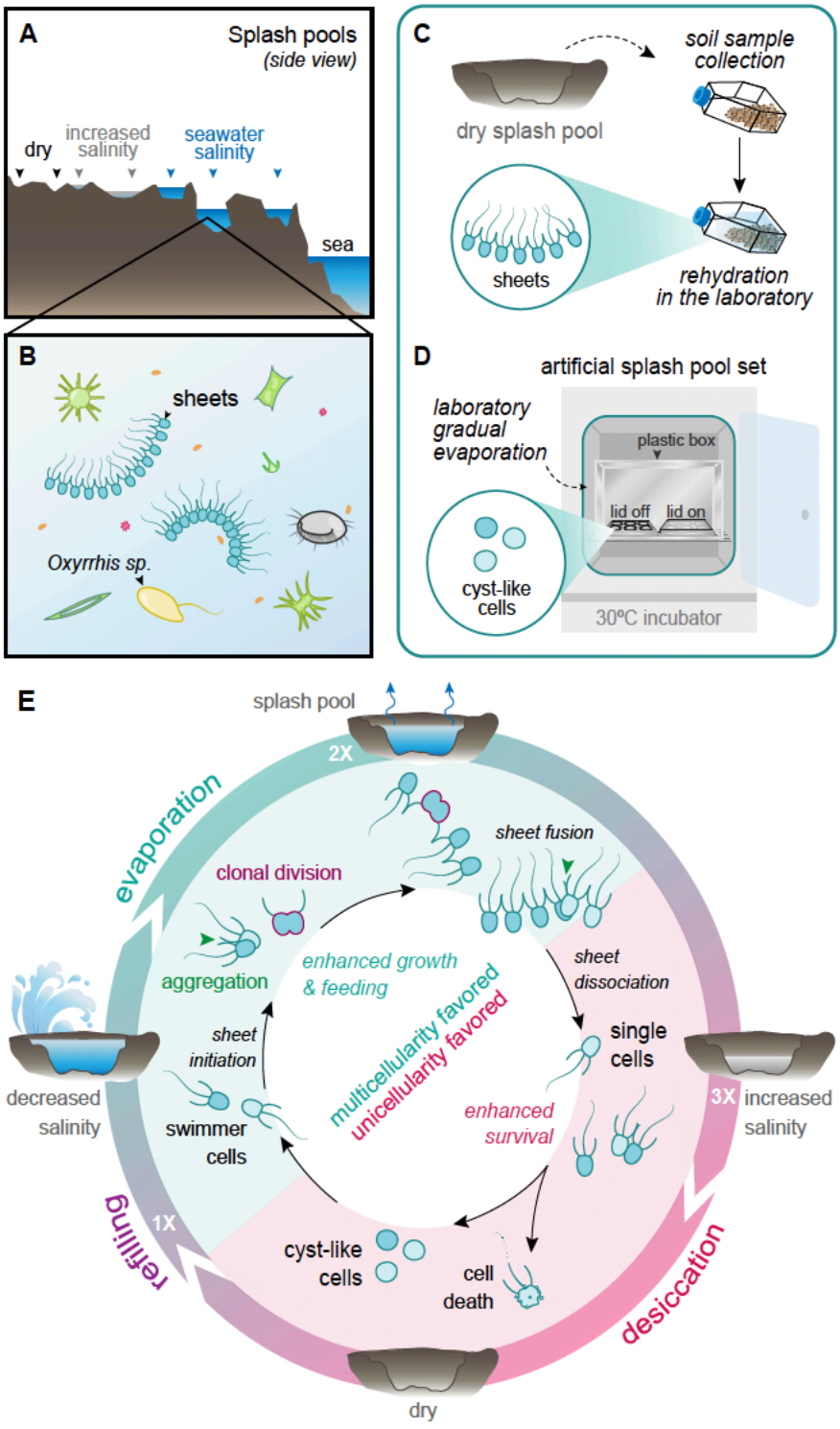

Figure 1.2. The environmentally entrained life history and unusual multicellular development of *C. flexa*.

(**A**) Schematic of splash pools on Curaçao's rocky shore (side view). Splash pools vary in size and environmental parameters like salinity levels. These pools experience constant evaporation and

intermittent refilling, leading to fluctuating salinity levels, and desiccation in some. (**B**) Sheet colonies are reliably found in a subset of splash pools of Curaçao, which are also home to diverse prokaryotes and eukaryotes. (**C**-**E**) Combining field and laboratory studies to characterize the life history of *C. flexa* in the context of their natural environment. (**C**) Sheets can be recovered from the rehydration of soil samples collected from dry splash pools, suggesting that *C. flexa* can survive desiccation in the wild. (**D**) By mimicking the gradual evaporation of splash pools in the laboratory, cultures of *C. flexa* sheets can be induced to differentiate into solitary cyst-like cells, which are characterized by their resistance to osmotic stress and desiccation. (**E**) A model of the life history of *C. flexa* entrained by salinity fluctuations typical of splash pools undergoing natural evaporation-refilling cycles. During evaporation-induced high salinity, *C. flexa* sheets dissociate into single cells, and part of the population differentiates into solitary cyst-like cells capable of surviving complete desiccation (while the other part of the population experiences cell death). Upon rehydration (and subsequent decrease in salinity), cyst-like cells transition back into flagellated-swimming cells that can reform colonies. *C. flexa* colonies develop through clonal division, aggregation, or a combination of both. This mixed mode of multicellularity may confer selective advantages in transient habitats like splash pools. Colonies exhibit enhanced feeding capabilities compared to single cells, which may promote population growth before the onset of unfavorable environmental conditions. Schematics from panels D and E were adapted from Ros-Rocher and Reyes-Rivera et al. 2024.

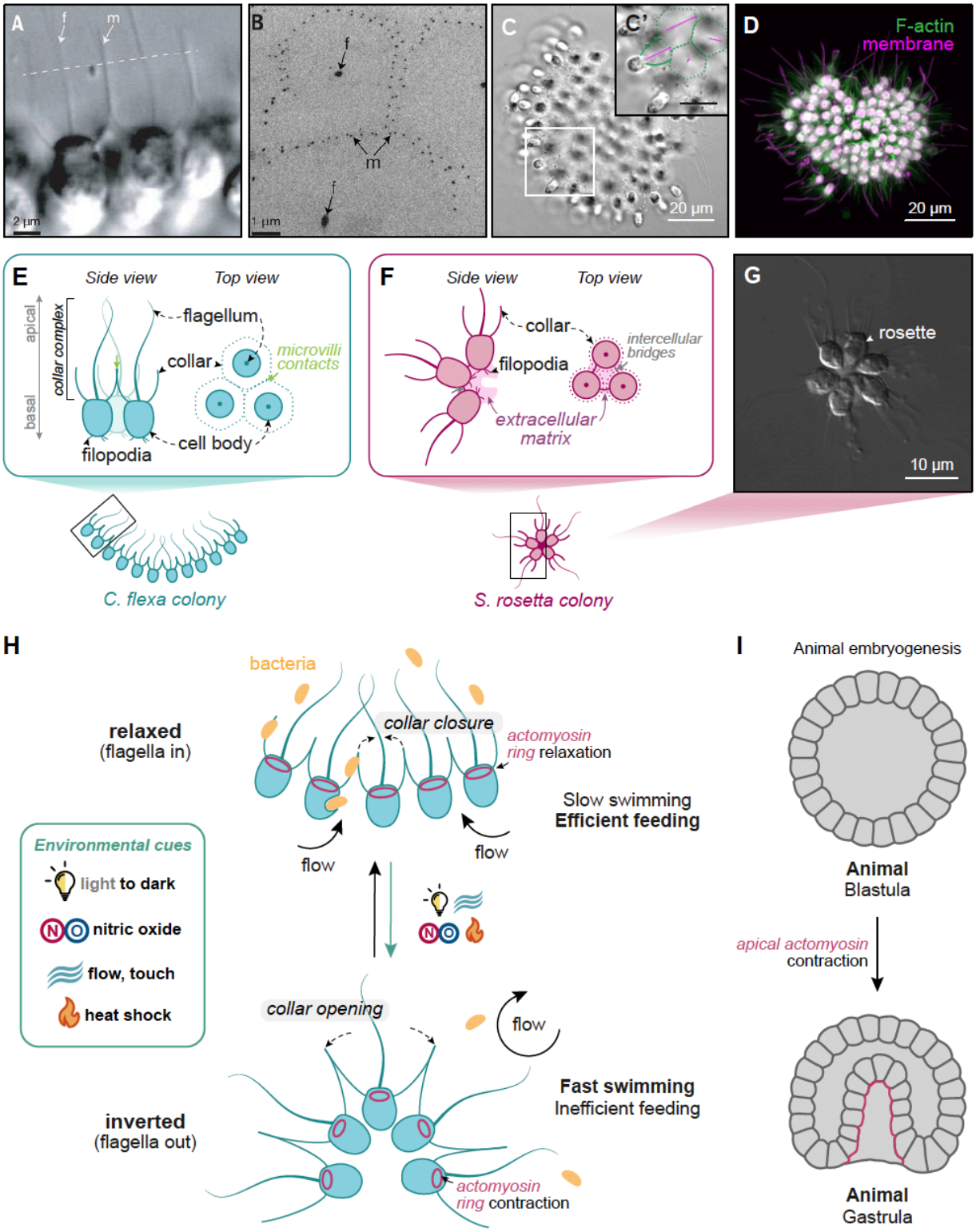

Figure 1.3. ***C. flexa*** **sheet architecture, inversion, and behaviors.**
(**A**-**E**) Architecture of *C. flexa* sheets. Cells in a sheet are attached to each other by their collars. (**A**) Brightfield image showing collar-collar interactions between neighboring cells (m =

microvilli, f = flagella). The dotted line indicates the micrograph's plane of section of panel **B**. (**B**) Transmission electron micrograph from a transverse section showing collar arrangement and interactions in a sheet (see dotted line in panel **A** for plane section reference) (**C**) Brightfield image of a relaxed sheet (flagella in). (**C'**) Inset: zoom in on the image in **C**. Pseudocolor is used to label microvillar collars (green) and flagella (magenta). (**D**) Airyscan 3D reconstruction of an inverted sheet (flagella out). The cell body and flagella are stained with a membrane dye (in magenta), and actin filaments of the collar are stained with phalloidin (in green). (**E**) Schematics of cell arrangement and microvillar contacts of *C. flexa* sheets. (**F**-**G**) Representative schematic (**F**) and micrograph (**G**) of rosette colonies of the model choanoflagellate *S. rosetta*. Unlike *C. flexa* sheets, rosettes are spherical and harbor an interior extracellular matrix to which cells anchor using their filopodia. Moreover, cells are interconnected by intercellular bridges that result from incomplete cytokinesis during clonal multicellular development (Dayel et al. 2011; Larson et al. 2019). (**H**-**I**) Colony inversion and behaviors of *C. flexa*. (**H**) Coordinated apical constriction of cells within colonies leads to the opening of their collars and consequent colony inversion. Colony inversion results in a trade-off between feeding and swimming behaviors: relaxed colonies are slow swimmers and efficient feeders, while inverted colonies swim rapidly and feed inefficiently. Multiple environmental cues regulate this behavioral switch, including light-to-dark transitions, nitric oxide, mechanical stimuli (flow and touch), and heat shocks. (**I**) The coordination of apical actomyosin constriction in *C. flexa* resembles tissue deformations observed during animal embryogenesis, such as gastrulation. The micrographs from panels A and B were published in Brunet, Larson, and Linden et al. 2019; micrographs from panels C and D were published in Ros-Rocher and Reyes-Rivera et al. 2024; and micrograph from panel G was published in Dayel et al. 2011.

Chapter 2

Mixed clonal-aggregative multicellularity entrained by extreme salinity fluctuations in a close relative of animals

The results presented here were published as part of the following paper:

Ros-Rocher, N and Reyes-Rivera, J. et al. Mixed clonal-aggregative multicellularity entrained by extreme salinity fluctuations in a close relative of animals. *bioRxiv* (2024) doi:10.1101/2024.03.25.586565

Supplementary Tables S1-S2, Files S1-S4, and Movies S1-S18 are available in the published online version.

Summary

Multicellularity evolved multiple times independently during eukaryotic diversification. Two distinct mechanisms underpin multicellularity: clonal development (serial cell division of a single precursor cell) and aggregation (in which independent cells assemble into a multicellular entity). Clonal and aggregative development are traditionally considered to be mutually exclusive and to result from independent acquisitions of multicellularity. Here, we show that the choanoflagellate *Choanoeca flexa*, a close relative of animals that forms contractile monolayers of cells (or "sheet colonies"), develops by an unconventional intermediate mechanism that we name "clonal-aggregative multicellularity". We find that *C. flexa* sheets can form through purely clonal processes, purely aggregative processes, or a combination of both, depending on experimental conditions. To assess the ecological relevance of these findings, we characterize the natural context of multicellular development in the native environment of *C. flexa* on the island of Curaçao. We show that the *C. flexa* life cycle is environmentally regulated by extreme salinity fluctuations in splash pools undergoing cycles of evaporation and refilling. Upon desiccation, *C. flexa* colonies dissociate into drought-resistant quiescent cells, which resume activity and reform multicellular sheets after rehydration. We hypothesize that clonal-aggregative development reflects selection for fast transitions into and out of multicellularity in the ephemeral context of coastal splash pools. Our findings underscore the potential of the exploration of biodiversity to reveal new fundamental biological phenomena and expand the known option space for both multicellular development and for the origin of animal multicellularity.

Introduction

The transition to multicellularity was a key event in animal evolution. Multicellularity has evolved independently over 45 times across eukaryotes (Lamża 2023) and can develop by two main mechanisms canonically depicted as mutually exclusive (Grosberg and Strathmann 2007; Brunet and King 2017; John Tyler Bonner 1998): clonal development or aggregative development (also referred to as “staying together” versus “coming together”, respectively (Staps, Van Gestel, and Tarnita 2019)). During clonal development, a single founder cell undergoes serial cell divisions without separation of sister cells, resulting in a genetically identical multicellular structure. In contrast, aggregative development refers to the formation of multicellular entities by grouping and coalescence of independent cells. Contrary to clonal development, aggregation allows genetically distinct cell populations to combine into chimeric multicellular structures (La Fortezza, Schaal, and Velicer 2022). The potentially low degree of genetic relatedness within aggregates can result in evolutionary conflict (*e.g.* vulnerability to "cheaters"; see glossary) and has been argued to limit the potential for aggregation to give rise to complex multicellularity, alongside the fact that aggregative multicellularity tends to be transient and facultative (Márquez-Zacarías et al. 2021; Knoll 2011; Fisher, Cornwallis, and West 2013; Pentz et al. 2020; Biernaskie and West 2015). Indeed, all five eukaryotic lineages with "complex multicellularity” (*i.e.* controlled three-dimensional morphogenesis and spatial cell differentiation), including animals, fungi, and land plants, develop clonally rather than by aggregation (Knoll 2011; Brunet and King 2017).

Despite the apparent evolutionary limitations of aggregative multicellularity, one remarkable feature of aggregation is the speed with which aggregative organisms can complete multicellular development from a unicellular state (often over a few hours (La Fortezza, Schaal, and Velicer 2022; Tarnita, Taubes, and Nowak 2013)). Aggregative multicellularity is often a stress response to environmental changes such as nutrient depletion (J T Bonner 1971; Keller and Segel 1970) or the presence of predators (Herron et al. 2019; Kessin et al. 1996; Trunk, Khalil, and Leo 2018). In such situations, aggregation allows for rapid establishment of a multicellular structure that confers some selective advantage (*e.g.* increased size, shielding of inner cells by a protective cell layer, or elevation from the substrate via formation of a stalk). This mechanism is faster than clonal division, and might be especially beneficial when cell proliferation (and therefore clonal development) is infeasible (J T Bonner 1971; La Fortezza, Schaal, and Velicer 2022; Trunk, Khalil, and Leo 2018). Thus, it has been argued that aggregation can be ecologically more advantageous than clonal development in fast-fluctuating environments, including conditions of acute stress (as an “emergency response”) (La Fortezza, Schaal, and Velicer 2022; Pentz et al. 2020; Stratford 1992).

Efforts to reconstruct the evolution of multicellularity in the stem lineage of animals have benefited from the study of their closest living relatives (the unicellular and facultatively multicellular holozoans (see glossary)) and notably of their sister group: the choanoflagellates (Figure 2.1A) (Ros-Rocher et al. 2021; Booth and King 2022; Ros-Rocher and Brunet 2023; Carr et al. 2008). Choanoflagellates are bacterivorous aquatic microeukaryotes bearing an apical flagellum surrounded by a collar of interconnected actin-filled microvilli (Figure 2.1B-C) (B. S. C.

Leadbeater 2015). Flagellar beating causes a water flow that carries bacterial prey toward the collar, where the bacteria are trapped and ultimately phagocytosed. Choanoflagellates can differentiate into diverse cell types, and can develop into facultative multicellular forms in many species (Brunet and King 2017; B. S. C. Leadbeater 2015; Fairclough, Dayel, and King 2010; Fairclough et al. 2013; Dayel et al. 2011). As in animals, multicellular development is clonal in all choanoflagellate species investigated so far, which contrasts with the occurrence of aggregative multicellularity in more distantly related lineages, such as filastereans (Hehenberger et al. 2017; Sebé-Pedrós et al. 2013; Mylnikov et al. 2019; Tikhonenkov et al. 2020) and dictyostelid amoebae (J T Bonner 1971; Du et al. 2015a). These observations have inspired the hypothesis that animals evolved from organisms with a simple form of clonal multicellularity, akin to that observed in certain modern choanoflagellates (Brunet and King 2017; Haeckel and Wright 1874; Nielsen 2008; Arendt et al. 2015).

Here, we describe an unusual type of multicellular development in the colonial choanoflagellate *Choanoeca flexa* (Brunet et al. 2019), which challenges previous generalities about choanoflagellates. We report that *C. flexa* colonies develop by a combination of clonal and aggregative development, which we refer to as 'clonal-aggregative multicellularity'. This mixed mode of development has never been formally described in choanoflagellates or other protists to our knowledge and nuances the textbook dichotomy between clonal and aggregative modes of multicellular development. We show that *C. flexa* clonal-aggregative development occurs in the context of a life cycle entrained by salinity fluctuations encountered in their natural habitat: splash pools that undergo cycles of evaporation and refilling on the timescale of a few days. We propose that this extreme, fast-fluctuating environment might have contributed to selecting for this unusual mode of multicellularity. Our observations establish *C. flexa* as a new model for the ecological context and developmental mechanisms of facultative multicellularity across close relatives of animals and expand the range of possible scenarios for the emergence of animal multicellularity.

Results

C. flexa was discovered in 2018 in splash pools (see glossary) on the rocky coast of the Caribbean island of Curaçao in the form of curved multicellular "sheet" colonies (Figure 2.1A-D) (Brunet et al. 2019). Cells within *C. flexa* colonies are held together through direct collar-collar interactions, forming a concave monolayer of cells with aligned apico-basal polarity (Figure 2.1B-D) (Brunet et al. 2019; Brunet and Booth 2023). *C. flexa* sheets display collective contractility under the control of environmental cues (including light-to-dark transitions), inverting their curvature and switching from a feeding state (relaxed form, flagella-in; Figure 2.1B) to a swimming state (contracted form, flagella-out; Figure 2.1D) (Brunet et al. 2019; Reyes-Rivera et al. 2022). In an earlier study, we established stable cultures of *C. flexa* sheets from a single isolated cell, indicating that sheets can arise from individual cells (Brunet et al. 2019). Nevertheless, the mechanisms of *C. flexa* multicellular development remained unexplored.

C. flexa sheets can develop clonally but are also able to expand by aggregation

To understand *C. flexa* colony development, we first isolated and monitored single cells from mechanically disassembled sheets by time-lapse microscopy. In this context, we observed clonal development of sheets by serial cell division (Figure 2.1E-F; movie 2.S1). After cell division, sister cells remained attached to each other by intermicrovillar contact. Cells continued to divide asynchronously (every ~8-10 hours), resulting in a monolayer of polarized cells with the signature curved morphology of *C. flexa* sheets (Figure 2.1E-F; movie 2S1). These observations show that small *C. flexa* sheets (up to 7 cells) can develop clonally from a single cell. To test whether clonal development can contribute to the further growth of *C. flexa* colonies, we monitored small- and medium-sized colonies (between 6 and 46 cells) by time-lapse microscopy and regularly observed clonal expansion by cell division both at the core and periphery of the sheets (Figures 2.1G and 2.S1; movies S2-S3). However, unexpectedly, we also captured instances of free-swimming single cells and doublets meeting colonies, attaching to their periphery, re-orienting their apico-basal polarity to align with neighboring cells, and seemingly integrating into the sheet (Figures 2.1G and 2.S1; movies S2-S3). Taken together, these results show that *C. flexa* colonies can form clonally but can also expand by aggregation. This motivated us to test whether *C. flexa* could also acquire multicellularity purely by aggregation (Figure 2.1H).

Aggregation is sufficient for multicellular development in *C. flexa*

To test whether *C. flexa* colonies can form by aggregation, we mechanically disassembled colonies into free-swimming single cells and performed live imaging of the dissociated cells (Figure 2.2A; movie S4). We found that *C. flexa* single cells aggregated within minutes into irregular masses of cells that continued incorporating additional cells and underwent repeated fusion into larger groups (a process known as agglomeration (Ros-Rocher et al. 2023); Figure 2.2A; movie S4). To determine the fate of these aggregates, we labeled two populations of

dissociated single cells with different fluorophores. Mixing both populations was followed by aggregation of cells of both colors within minutes (Figure 2.2B; movie S5). After 24 hours, we observed chimeric colonies displaying the polarized cup-shaped morphology typical of canonical *C. flexa* sheets and comprising cells of both colors (Figures 2.2C and 2.S2A; movies S6-S8), indicating that they had developed by aggregation. To better understand the dynamics of aggregative development, we fixed aggregates at different stages and imaged them by Airyscan confocal microscopy. We found that early aggregates (fixed up to 6 hours post-dissociation (6 hpd)) displayed a variable and irregular morphology with cells frequently showing unaligned apico-basal polarity, likely resulting from collision and attachment of cells in diverse random orientations (Figures 2.2D and 2.S2B; movies S9-S12). Colonies observed 24 hpd, on the other hand, consistently showed *bona fide C. flexa* sheet morphology with regularly aligned cells (Figures 2.2D and 2.S2B; movie S13), suggesting that early irregular aggregates had by then completed their maturation into canonical sheets. At that stage, colonies comprised about 50 cells on average and as many as 120 cells (Figure 2.2E). This size further supported the idea that these sheets could not have formed exclusively by clonal development within 24 hours, given the cell cycle duration in *C. flexa* (at least 8 hours, which could result in sheets comprising at most 16 cells assuming maximal and synchronized proliferation; see Figure 2.1F). Indeed, treatment with the cell cycle inhibitor aphidicolin abolished cell proliferation (Figure 2.S3) but did not prevent colony formation from dissociated cells (Figure 2.2F), confirming that aggregation was sufficient for *C. flexa* multicellular development.

Our observation of aggregative development in *C. flexa* contrasts with earlier observations in other species of multicellular choanoflagellates, which had so far been found to develop strictly clonally (Brunet and King 2017; B. S. C. Leadbeater 2015; Fairclough, Dayel, and King 2010). Given that other protists often deploy aggregative development as an “emergency response” to fluctuating environments (Keller and Segel 1970; John Tyler Bonner 1998), while clonal development is thought to more frequently result in stable structures capable of feeding and cell proliferation, we were curious about the natural conditions of *C. flexa* mixed clonal-aggregative development. Thus, we set out to investigate the natural ecological context of *C. flexa* multicellular development.

Multicellular *C. flexa* sheets occur in a restricted salinity range in their natural environment

C. flexa was originally discovered in its multicellular form on the Caribbean island of Curaçao (Brunet et al. 2019), a semi-arid tropical island that experiences dry and rainy seasons (Figure 2.3A) (Kjerfve 1998). Unlike other multicellular choanoflagellate species (Booth and King 2022; B. S. Leadbeater 1983), *C. flexa* has been repeatedly re-isolated in the wild since its discovery in 2018 and can thus be studied in its natural environment. *C. flexa* sheets are found in splash pools on the wind-exposed northern part of the island (Figures 2.3A-B and 2.S4A-B) that undergo natural cycles of desiccation and refilling (Little and Kitching 1996; Garbary 2007). Water-filled splash pools experience gradual evaporation, leading to increasing salinity and, occasionally, complete desiccation (Figure 2.3C). Splash pools refill from crashing waves, splash, or rain, restoring lower salinity levels (Figures 2.3C and 2.S4B; movie S14). Splash pools are, consequently, ephemeral habitats in which organisms often experience extreme and recurrent

hypersaline and hyperosmotic stress (Garbary 2007; Huggett and Griffiths 1986; Amsalem and Rilov 2021; Davison and Pearson 1996). Thus, we investigated how this highly fluctuating environment might influence the life history and multicellular development of *C. flexa*.
We focused our studies on Shete Boka (meaning "seven bays" in Papiamento) National Park, where *C. flexa* is reliably found (Figure 2.3A). We surveyed the distribution of *C. flexa* in 150 splash pools and measured splash pool salinity in two different field expeditions: Exped-A and Exped-B (Figure 2.3D). During Exped-A, we randomly sampled 79 splash pools (numbered Sp1 to Sp79) along about 2 kilometers of coastline in Shete Boka (Figure 2.3D; see methods). While seawater collected from the neighboring inlets or *bokas* had a stable salinity of 40 parts per thousand (ppt), splash pool salinity ranged from below average seawater salinity (25 ppt) to saturation (≥ 280 ppt) (Figures 2.3E and 2.S4C).

In 10 out of 79 splash pools, we found sheets that exhibited the stereotypical *C. flexa* cup-shaped morphology and inversion behavior in response to light-to-dark transitions (Brunet et al. 2019) (Figures 2.3F and 2.S5A-C; movie S15). 18S ribosomal DNA sequencing of manually isolated sheets confirmed their identification as *C. flexa* (Figure 2.S5D; supplementary files S1-S4). Interestingly, although the salinity of surveyed splash pools ranged from 0.6-fold to 7-fold of that measured in seawater from the neighboring *bokas*, *C. flexa* sheets were only found in splash pools with <2-fold seawater salinity (<73 ppt; Figures 2.3E and 2.S4C). To independently test whether the presence of multicellular *C. flexa* was constrained by an upper bound of salinity, we employed a different sampling strategy during a second expedition (Exped-B) in which we exhaustively sampled all splash pools within a 4-meter by 10-meter quadrant (n=71, numbered Sp1 to Sp71; Figure 2.3D; see methods). We found sheets in 14 out of 71 splash pools, with a 94 ppt salinity upper bound for sheet occurrence (Figures 2.3E and 2.S4C). Across both expeditions, *C. flexa* sheets were found in splash pools with an average salinity of 61.42 ± 17.54 ppt, 1.56-fold higher than natural seawater from the *bokas* (Figures 2.3E and 2.S4C) and significantly lower than the salinity of sampled splash pools that did not contain sheets (155.1 ± 107.2 ppt; p=3.1e-04 by the Mann-Whitney U test). We never observed sheets in splash pool water with a salinity above 94 ppt (2.35-fold seawater salinity; Figures 2.3E and 2.S4C).

Transitions into and out of multicellularity correlate with the natural evaporation-refilling cycle of splash pools

We then set out to study the natural evaporation-refilling cycle of splash pools and how it may impact the presence/absence of sheets. We monitored ten splash pools in which *C. flexa* sheets were found and five more randomly selected splash pools daily over eight days (Figures 2.3G-H and 2.S6). We screened samples for sheets once per day and measured the salinity and maximum depth of each splash pool (Figures 2.3G-H and 2.S6). We observed a gradual decrease in depth and concomitant increase in salinity in all 15 splash pools (presumably due to evaporation; Figure 2.S6A-B), six events of complete desiccation (Figure 2.S6C-D), and four events of refilling (Figure 2.S6E-F; see three examples in Figure 2.3H). In all cases, *C. flexa* sheets were no longer observed after salinity crossed a ~100 ppt threshold during gradual evaporation (Figures 2.3H and 2.S6), consistent with results from Exped-A and Exped-B (Figures 2.3E-H and 2.S6). Moreover, artificial evaporation of a natural splash pool sample containing sheets in the

laboratory led to sheet disappearance (Figure 2.S7). These observations further reinforced the idea that the multicellular form of *C. flexa* might not tolerate high salinity levels.

Interestingly, in two dry splash pools that underwent refilling during our study (restoring salinity down to ~50 ppt), sheets were re-observed 48 hours after refilling (Sp69 and Sp70; Figures 2.3H and 2.S6E-F). The new incoming sheets may have arrived from waves or splash, or may have been transferred from neighboring splash pools. Alternatively, *C. flexa* might have persisted in the soil of desiccated splash pools in a hitherto unrecognized resistant form, perhaps in the form of unicellular cysts (which have been morphologically reported in other choanoflagellates (Stein 1859; Saville-Kent 1880; Reess and Fisch 1887; B. S. C. Leadbeater and Karpov 2000; Stoupin et al. 2012; Jeuck, Arndt, and Nitsche 2014)). Under this hypothesis, colonies would disassemble and transition into resistant single cells under high salinity, and those cells would then develop back into sheets once salinity decreased. To explore this possibility *in situ*, we collected soil samples from six desiccated splash pools in which *C. flexa* had been previously observed, rehydrated them in the lab (down to ~65 ppt salinity) and monitored the rehydrated samples for several days (Figure 2.3I-J; movie S16). Surprisingly, sheets could be recovered in various soil samples collected from one splash pool after two to seven days of desiccation (Figure 2.3I-J). Sheets consistently appeared 48-72 hours post-rehydration, suggesting that a resistant form of *C. flexa* can survive complete desiccation in the wild for at least a week (Figure 2.3I-J). Interestingly, the presence of choanoflagellates in soil might be a more general phenomenon: metagenomic analyses of soil samples from diverse environments have revealed the presence of choanoflagellate species yet to be studied (Venter, Nitsche, and Arndt 2018; Elsas et al. 2019), which might represent a significant and poorly understood ecological niche for choanoflagellates (Brunet et al. 2021).

Given that salinity fluctuations in splash pools seemed to dramatically impact *C. flexa* multicellularity in nature, we next set out to investigate the phenotypic response of *C. flexa* to evaporation-refilling cycles in a laboratory context.

Experimental evaporation-refilling cycles cause reversible transitions into and out of multicellularity

To better understand the response of *C. flexa* to evaporation, desiccation, and refilling, we designed an experimental setup mimicking the natural evaporation-refilling cycles of Shete Boka splash pools (Figures 2.4A and 2.S8). As a first step, we calculated the empirical evaporation rate of 12 splash pools in our longitudinal field survey (see methods; Figure 2.S8A-B). We then subjected *C. flexa* cultures to evaporation in an incubator (Figure 2.S8C), matching both the temperature (30°C) and evaporation rate to that observed in natural splash pools (see methods; Figure S8D). This setup resulted in complete desiccation after four days of evaporation (starting from artificial seawater (ASW) with a salinity of 35 ppt, referred to as 1X salinity in the rest of the text). Under these conditions, *C. flexa* sheets gradually dissociated into non-motile single cells (Figures 2.4A-B and 2.S9; movie S17), with more than 50% of the cells being solitary when salinity crossed the limit of sheet occurrence observed in the field (94 ppt; Figures 2.3E and 4A). Almost all sheets had dissociated into single cells when salinity reached saturation (Figures

2.4A-B and 2.S9; movie S17). As a negative control, we monitored identically treated cultures that were not undergoing evaporation and observed that colonies remained multicellular throughout the experiment (Figure 2.S10). This suggested that sheet dissociation in the gradual evaporation setup was caused by the increasing salinity. To independently test this hypothesis, we raised the salinity of *C. flexa* cultures by directly adding seawater salt (without evaporation) and similarly observed dissociation of multicellular sheets into single cells (Figure 2.S11A-C).

To test whether single cells resulting from sheet dissociation in the lab were viable and could survive desiccation, we mimicked splash pool refilling by rehydrating gradually evaporated samples with artificial seawater three hours after full desiccation. This brought salinity back down to ~50 ppt and was followed by the reappearance of small sheets as soon as 24 hours post-rehydration. The fraction of cells in colonies increased gradually until ~50% of cells were colonial on day 7 and ~75% on day 9 (Figure 2.4A-B).

We assessed the mechanism of colony re-formation by time-lapse microscopy of desiccated cultures after rehydration and captured instances of unicellular flagellates engaging in both clonal and aggregative multicellular development (Figure 2.4C; movie S18). Taken together, our results show that *C. flexa* sheets dissociate into non-motile single cells during gradual evaporation, that these solitary cells can survive complete desiccation under laboratory conditions, and that sheets reform after rehydration through both clonal division and aggregation. These findings are consistent with our field observations, where we recovered sheets after rehydrating soil samples from a dry splash pool (Figure 2.3I-J), and further support the existence of a desiccation-resistant form of *C. flexa*.

C. flexa differentiates into solitary cyst-like cells at high salinity

We then set out to further investigate the phenotype of the desiccation-induced single cells. In diverse protists, resistance to desiccation is often achieved by differentiation into cysts (Y. Li et al. 2022; Schaap and Schilde 2018; Verni and Rosati 2011), which are dormant cells with reduced metabolic activity and minimal or arrested proliferation. This process, known as encystment, often entails significant morphological changes such as rounding of the cell body, changes in cell volume, flagellar loss, and formation of a protective cell wall (B. S. C. Leadbeater and Karpov 2000; Y. Li et al. 2022; Griffiths 1969; Gong et al. 2018; Bowers and Korn 1969; Corliss and Esser 1974; Chen et al. 2018; Grimes 1973; Atkins, Anderson, and Wirsen 1998). First, we determined whether *C. flexa* desiccation-resistant cells (hereafter ‘cyst-like cells’) actively proliferate by quantifying cell growth during gradual evaporation in the laboratory. We found that growth was arrested above 2X salinity, with net cell loss above 3X salinity (Figures 2.4D and 2.S12). These effects may be attributable to a halt in the cell cycle and cell death due to hypersaline stress, similar to processes observed during encystment in other protists (J T Bonner 1971; Y. Li et al. 2022; Griffiths 1969; Atkins, Anderson, and Wirsen 1998; Khan, Iqbal, and Siddiqui 2015).

We next monitored cellular morphology by DIC microscopy during gradual evaporation and observed structural changes that occurred asynchronously, resulting in a heterogeneous cell

population (Figure 2.4E). At 3X salinity, most cells had dissociated from their colonies and bore a round cell body lacking microvilli and, most often, lacking a flagellum (Figure 2.4Eii). Additionally, some cells exhibited multiple filopodia-like protrusions (Figure 2.4Eiii). Membrane and F-actin staining of cyst-like cells confirmed that they lacked a collar complex (Figures 2.4F and 2.S13) but also revealed that they transiently formed an F-actin cortex, detectable at 3X salinity but lost above 6X (close to saturation; Figures 2.4F-G and 2.S13). This transient actin cortex might contribute to protecting the plasma membrane against osmotic stress during the initial differentiation stages (Di Ciano et al. 2002; Komis, Apostolakos, and Galatis 2002; Rivero et al. 1996; Aizawa et al. 1999).

Finally, morphometric analysis of cell body and nucleus volume showed that cyst-like cells had a larger nucleus-to-cytoplasm ratio compared to flagellate cells cultured in 1X salinity ($p=3.4e-05$; Figures 2.4H and 2.S14). An increase in the nucleus-to-cytoplasm ratio frequently correlates with cell quiescence in other systems (Balachandra, Sarkar, and Amodeo 2022), consistent with the growth arrest in *C. flexa* cyst-like cells (Figures 2.4D and 2.S12). To confirm that these changes were induced by hypersaline stress, we directly increased the salinity of *C. flexa* cultures by addition of seawater salt, and observed similar morphological changes and arrest in cell growth (Figure 2.S11).

In sum, hypersalinity caused drastic and reversible changes in cell architecture and growth: loss of the collar and flagella (and thus of motility), formation of a transient actin cortex, increased nucleus-to-cytoplasm ratio, and arrest of cell growth (Figure 2.4I), resembling the changes that occur during encystment in diverse protists (Y. Li et al. 2022; Griffiths 1969). Thus, during the evaporation-refilling cycle of a splash pool, *C. flexa* likely alternates between a multicellular flagellated form (at low salinity) and a unicellular cyst-like form (at high salinity), suggesting these two phenotypes benefit from an adaptive advantage in their respective environment. We thus decided to directly test for these putative advantages in laboratory conditions.

Multicellular sheets are advantaged at low salinity and unicellular cyst-like cells are advantaged at high salinity

If *C. flexa* cyst-like cells represent a desiccation-resistant form, we could expect these cells to be more resistant to hypersaline stress and desiccation compared to sheets. To test this, we compared the survival of both sheets and cyst-like cells after desiccation. We subjected sheets to fast evaporation, which resulted in complete desiccation from 1X salinity over 20 hours (see methods). Under these conditions, cells did not acquire a cyst-like morphology but instead retained an observable flagellum, collar, and multicellular morphology even after complete desiccation (Figure 2.S15). This suggests that the formation of cyst-like cells requires gradual evaporation at a comparable rate to that of natural splash pools. In parallel, we induced the differentiation of *C. flexa* into cyst-like cells by slow evaporation following the protocol detailed in the previous section (from 1X salinity to desiccation in 72 hours). After desiccation, we rehydrated both types of cells by adding 1X ASW and monitored their recovery. We found that desiccated sheets having undergone rapid evaporation never developed into viable cells after rehydration (Figure 2.5A). By contrast, as in the experiments detailed earlier, rehydrated cyst-

like cells consistently gave rise to viable sheets, confirming that they had survived desiccation (Figure 2.5A). These observations show that cyst-like cells, unlike flagellates, are equipped to survive hypersalinity and desiccation, and suggest that differentiation into cyst-like cells confers a selective advantage during evaporation. The loss of multicellularity during differentiation into cyst-like cells is likely linked to the retraction of the microvillous collar that connects cells within sheet colonies.

Because unicellular cyst-like cells seemed to have a survival advantage over multicellular flagellates in the hypersaline phase of the evaporation-refilling cycle, we wondered whether multicellularity, by contrast, was advantageous in the other phase of the cycle, marked by low salinity. It has been speculated that multicellularity in choanoflagellates might enhance feeding via cooperative hydrodynamic interactions between flagella, increasing the flux of bacterial prey towards the collar (Fenchel 2019; Koehl 2021; Cavalier-Smith 2017); however, this concept remains uncertain in the model choanoflagellate *Salpingoeca rosetta*, with different studies having come to contrasting conclusions (Fenchel 2019; Kirkegaard and Goldstein 2016a; L'Etoile and King-Smith 2020). To test for a feeding advantage in multicellular sheets of *C. flexa*, we quantified the capture of fluorescent bacteria in sheets and dissociated single flagellates (Figure 2.5B-C). We found that sheets captured more than twice as many fluorescent bacteria per cell as single cells (Figure 2.5B-C). This suggests that multicellularity confers a prey capture advantage at the salinity levels that are compatible with cells maintaining a functional collar complex and, therefore, with feeding.

Taken together, our findings support a model of *C. flexa* life history that correlates with the evaporation-refilling cycle of splash pools characteristic of their natural habitat (Figure 2.5D). *C. flexa* sheets are found in water-filled splash pools with salinities below ~2.3-fold that of natural seawater. As gradual evaporation proceeds, salinity increases, and sheets dissociate and differentiate into solitary, non-motile, and non-proliferative cyst-like cells (some of which undergo cell death). These cyst-like cells can survive complete desiccation and persist in the soil of the splash pools. After splash pool refilling, cyst-like cells regrow a collar complex and transition back into free-swimming flagellates that develop into multicellular sheets by aggregation and/or clonal division, a phenotype that more efficiently captures bacteria and presumably supports faster cell proliferation.

Discussion

The ecological context of *C. flexa* clonal-aggregative multicellularity

Our results show that *C. flexa* can form multicellular sheets through a combination of clonal division and aggregation following the rehydration of desiccated cyst-like cells. This mixed developmental strategy might represent an adaptation to the ephemeral nature of water-filled splash pools, allowing faster multicellular development by simultaneous action of both mechanisms. It might also serve as a versatile strategy for robust re-establishment of multicellularity across a broad range of environmental conditions: indeed, aggregative and clonal multicellularity are subjected to different constraints, as they respectively depend on cell density and on the possibility of cell division (which is in turn constrained by salinity and availability of bacterial prey). In our laboratory experiments, *C. flexa* appeared capable of both purely clonal development (at low cell density and under permissive conditions for proliferation) and purely aggregative development (at sufficient cell density, even if proliferation is compromised), as well as intermediate modes.

The selective advantage of multicellularity has been the subject of intense debates (Koehl 2021; Stanley 1973; Tong, Bozdag, and Ratcliff 2022; Richter and King 2013) and multiple studies in choanoflagellates (Fenchel 2019; Koehl 2021; Kirkegaard and Goldstein 2016b; Boraas, Seale, and Boxhorn 1998; Chin et al. 2023; Kumler et al. 2020; Roper et al. 2013). In the case of *C. flexa*, the prey capture efficiency of cells within sheets surpasses that of solitary flagellated cells, suggesting a feeding (and likely reproductive) benefit of multicellularity. Cooperative feeding—a trait observed among various protists—has been postulated as a selective factor for the evolution of multicellularity (Short et al. 2006). However, other advantages of multicellularity might exist in *C. flexa*. Prominently, *C. flexa* colonies exhibit collective behavior through coordinated contractility that implements whole-colony inversion. Inversion allows reversible transitions between feeding and swimming states and is modulated by several signals, including mechanical stimuli, heat shocks, and nitric oxide (Reyes-Rivera et al. 2022). This switch is also regulated by light-to-dark transitions, thus enabling photokinesis (preferential accumulation of sheets under light) (Brunet et al. 2019). Our previous research indicates that individual cells from dissociated sheets are no longer capable of photokinesis, suggesting this behavior requires multicellularity (Brunet et al. 2019). Moreover, multicellular groups show decreased vulnerability to size-selective predators in different protists and predator avoidance has been proposed as a potential selective force for evolving multicellularity (Herron et al. 2019; Koehl 2021; La Fortezza, Schaal, and Velicer 2022; Tong, Bozdag, and Ratcliff 2022) (but see (Kumler et al. 2020)).

More generally, the environmentally entrained life history transitions of *C. flexa* are in line with other recently described examples. Unicellular-to-multicellular switches are controlled by fluctuating environmental parameters in other species, such as salinity for cyanobacteria in brackish environments (Tang, Pichugin, and Hammerschmidt 2023) and periodic flooding for cave bacteria attached to surfaces (Mizuno et al. 2022). A selective advantage for regulated life cycles in fluctuating environments has also been supported by laboratory experiments in yeast

(Barrere, Nanda, and Murray 2023) and by theoretical models (Pichugin, Park, and Traulsen 2019; Staps, Van Gestel, and Tarnita 2019; 2022). The phenotypic plasticity of *C. flexa* might thus enable it to reap both the benefits of multicellularity (for feeding and collective behavior) under permissive conditions, and of differentiation into solitary cyst-like cells for individual survival under harsh conditions.

Evolutionary implications of mixed clonal-aggregative multicellularity

The clonal-aggregative multicellularity of *C. flexa* contrasts with that of previously characterized multicellular choanoflagellates, which appear to develop solely clonally (Brunet and King 2017; B. S. C. Leadbeater 2015; Fairclough, Dayel, and King 2010; Dayel et al. 2011; H. James-Clark A. B. 1867; S.a and S.j 1998; B. S. C. Leadbeater 1983; Hibberd 1975; Pettitt et al. 2002). Indeed, the best-characterized example is the formation of rosette colonies in *S. rosetta*, which occurs by serial cell division without separation of sister cells and thus requires cell proliferation (Fairclough, Dayel, and King 2010). *S. rosetta* can also develop into chain colonies, which are similarly thought to form clonally (Fairclough et al. 2013; Dayel et al. 2011).

Beyond choanoflagellates, both clonal and aggregative multicellularity are widely present, with a discontinuous occurrence, across unicellular holozoans (Marshall and Berbee 2011; Suga and Ruiz-Trillo 2013; de Mendoza et al. 2015; Dudin et al. 2019; Kożyczkowska et al. 2021; Shah et al. 2023; Sebé-Pedrós et al. 2013; Ros-Rocher et al. 2023; Hehenberger et al. 2017; Mylnikov et al. 2019; Tikhonenkov et al. 2020) and eukaryotes as a whole (Brunet and King 2017; Nagy et al. 2020; Brown, Spiegel, and Silberman 2009; Toret et al. 2022). The scattered distribution of clonal and aggregative multicellularity is currently interpreted as reflecting independent evolutionary origins of both types of development (John Tyler Bonner 1998). However, the discovery of clonal-aggregative multicellularity in a eukaryote raises the intriguing alternative possibility of evolutionary interconversions between aggregative and clonal multicellular development (via a mixed intermediate). Future studies of clades that contain both clonal and aggregative forms (such as Holozoa and Holomycota) might help test this possibility. Although mixed clonal-aggregative multicellularity has not been formally reported before in other protists to our knowledge, some parallels can be drawn with processes described in other taxa or contexts: for example, clonality and aggregation might cooperate in the formation of bacterial boofilms (Sauer et al. 2022) and in the development of (unicellular but multinucleated) syncytia in reticulopodial amobae (Lamża 2023). This raises the possibility that mixed clonal-aggregative development might be more widespread than currently appreciated.

Interestingly, the phenotype of *C. flexa* colonies differs in some important respects from that of most previously described aggregative structures. The paradigmatic model of aggregative multicellularity is fruiting body formation (see glossary), which has been well-characterized in dictyostelid amoebae (Keller and Segel 1970; Du et al. 2015b; John Tyler Bonner 1998) and evolved convergently multiple times across eukaryotes (Brown and Silberman 2013; Brown et al. 2012) (and even at least once in bacteria (Curtis et al. 2007)). Fruiting bodies are masses of dormant cells (sometimes together with cells having undergone cell death) that disperse into single cells before resuming metabolic activity and proliferation upon the restoration of

favorable environmental conditions. By contrast, *C. flexa* sheets are proliferatively and behaviorally active, and appear to survive and reproduce in a multicellular form as long as permissive conditions persist. Thus, the ecological niche accessible to mixed clonal-aggregative multicellularity might differ from that typical of purely aggregative forms.

Aggregative multicellularity comes with a well-known evolutionary challenge: one aggregate can combine cells of different ancestries and potentially different genotypes, thus raising the possibility of conflict (Pentz et al. 2023; Hammerschmidt et al. 2014; Michod 2007). Aggregates are notably vulnerable to cheater genotypes, which reap the benefits of multicellularity without contributing their fair share of the cost of multicellular development. Such cheaters have, for example, been described in *Dictyostelium* (Strassmann, Zhu, and Queller 2000), in the fruiting body-forming bacterium *Myxococcus* (Velicer, Kroos, and Lenski 2000), and in flocculating yeast (Pentz et al. 2020). The evolutionary challenge posed by cheater mutants can be addressed by strategies that limit aggregation to fellow co-operators, either directly by co-operator recognition (so-called "green beard" mechanisms (Queller et al. 2003; Gruenheit et al. 2017)) or indirectly by preferential aggregation with close relatives. Restriction of aggregation to relatives can either be enforced actively by kin recognition (mediated by polymorphic loci (Benabentos et al. 2009; S. I. Li and Purugganan 2011; Espinosa and Paz-y-Miño-C 2014)) or be facilitated passively by spatial structuration of the environment that can limit dispersal (Smith, Strassmann, and Queller 2016; West, Griffin, and Gardner 2007). The latter might be relevant to *C. flexa*, as splash pools are collections of disconnected environments that might lead to geographic divergence of genotypes (as shown for other organisms in similar environments, such as *Daphnia* metapopulations in tide pools (Haag et al. 2006)). Splash pools might thus favor the evolution of aggregative multicellularity by mitigating the need for strong kin recognition mechanisms. This is in line with recent models supporting an “ecological scaffolding” function for patchy environments in the emergence of multicellularity (Black, Bourrat, and Rainey 2020). In the future, studies of potential kin recognition mechanisms, natural genetic diversity and dispersal in *C. flexa* might shed further light on these questions.

Conclusion

Our study documents an unusual mode of multicellular development that combines features of clonal and aggregative multicellularity in a choanoflagellate, belonging to the sister-lineage of animals. This complex life cycle further underscores the emerging concept of considerable phenotypic and developmental plasticity among close unicellular relatives of animals, supporting the existence of a complex life cycle in unicellular ancestors of animals (Ros-Rocher et al. 2021; Brunet and King 2022).

Beyond this, our study establishes *C. flexa* as a model to study the facultative multicellular development of a close relative of animals in its natural context. This contrasts with other well-characterized facultatively multicellular holozoans, such as *S. rosetta* (Booth and King 2022) and *C. owczarzaki* (Ferrer-Bonet and Ruiz-Trillo 2017), which could both be isolated only once from their natural environment and in which studies of unicellular-to-multicellular transitions are thus inevitably restricted to laboratory setups. In the future, we expect the dialogue between field and lab studies of *C. flexa* to continue, clarifying questions such as the selective advantage(s) and ecological implications of multicellularity and unicellularity, as well as the existence of possible natural kin recognition mechanisms and cheater mutants.

Acknowledgments

We thank the personnel of the Shete Boka National Park in Curaçao for access to the field site. We thank Tess Linden for help during preliminary field work experiments and feedback on the manuscript. We thank Marvin Albert, Stéphane Rigaud and Jean-Yves Tinevez at the Image Analysis Hub at the Institut Pasteur for feedback on image analyses. We acknowledge Pierre-Henri Commere and Sebastien Megharba from the Flow Cytometry platform at Institut Pasteur for support with single-cell isolation of new *C. flexa* isolates by flow cytometry. Special thanks to Geneviève Milon and Noah Whiteman for feedback and useful discussions on laboratory and fieldwork experimental design, respectively. We also thank members of Brunet and King laboratories for feedback and useful discussions and Jaime Ramirez and Kayla Dinshaw for technical support during preliminary experiments. NRR is supported by the European Union's Horizon Europe research and innovation funding program under a Marie Skłodowska-Curie Actions grant (Grant Agreement ID: 101106415). JRR is supported by a National Science Foundation Graduate Research Fellowship Program (grant no. 1752814). NK and work in the King lab is supported by the Howard Hughes Medical Institute. TB and work in the Brunet lab is supported by the Institut Pasteur (G5 package), the CNRS (UMR 3691), and by the ERC Starting Grant EvoMorphoCell (Grant agreement ID: 101040745). Funded by the European Union. Views and opinions expressed are however those of the author(s) only and do not necessarily reflect those of the European Union or the European Research Council. Neither the European Union nor the granting authority can be held responsible for them.

Glossary

Cheaters: in social evolution theory, organisms that receive a benefit at the cost of other organisms of the same species within the context of a collective behavior. In the case of aggregative multicellularity, cheaters are cells within a chimeric multicellular aggregate that impair collective outcomes to their own benefit. For example, in sorocarp-forming eukaryotes, cheaters differentiate disproportionately into spores (reproductive cells) rather than other cell types (such as stalk cells), giving them a higher likelihood of reproducing than non-cheaters. Cheaters can exploit shared resources in a way that enhances their own fitness at the expense of the collective. The existence of cheaters may impede group-level selection of traits and result in evolutionary conflict (Strassmann, Zhu, and Queller 2000; Velicer, Kroos, and Lenski 2000).

Fruiting body: a spherical mass of stress-resistant cells (spores or cysts), often in a quiescent state, that eventually undergoes disassembly and dispersal (Broersma and Ostrowski 2022). Fruiting bodies often result from aggregative development and are sometimes equipped with a stalk providing elevation from the substrate, and facilitating dispersal by the wind after dissociation.

Holozoa: eukaryotic clade encompassing all species more closely related to animals than to fungi. Holozoa comprises various clades, including Metazoa (animals), Choanoflagellata, Filasterea, Corallochytrea/Pluriformea, and Ichthyosporea. Unicellular eukaryotes (*a.k.a.* protists) within the Holozoa clade are pivotal for elucidating the evolutionary transitions that facilitated the emergence of multicellularity in animals from unicellular ancestors (Hehenberger et al. 2017; Adl et al. 2019; Ocaña-Pallarès et al. 2022).

Splash pools: shallow seawater pools in rocky shores inhabited by prokaryotic and eukaryotic organisms that are occasionally filled with seawater by oceanic waves and splash (and sometimes with rainwater). In Curaçao, the substrate of splash pools is composed mainly of limestone. Their sizes range from a few centimeters to a few meters. In splash pools, environmental conditions such as seawater volume, temperature, salinity, and oxygen fluctuate as they undergo natural evaporation-refilling cycles over a few days or weeks. Thus, splash pools are considered extreme environments.

Materials and Methods

Cell strain and growth conditions

Choanoeca flexa monoaxenic cultures (*ChoPs7* strain, established as in (Brunet et al. 2019)) were grown in 25 cm^2 tissue-culture treated flasks (#130189, ThermoFisher Scientific), either in 1% (v/v) Seawater Complete (SWC) or 5% (v/v) Cereal Grass Medium 3 (CGM3) medium, following the protocols below:

Culture in 1% (v/v) SWC: cells were cultured 10 mL filter-sterilized 1X Artificial Seawater (see recipe below) and 1% (v/v) SWC (see recipe below), hereafter referred to as SWC medium, unless otherwise specified. Cultures were supplemented with 1% (v/v) *Halopseudomonas oceani* (formerly *Pseudomonas oceani*) resuspended food pellet (see below) and kept in a 25°C incubator (Memmert IPP410ecoplus) under a 12-hour light-dark cycle. Incubator humidity was maintained by placing an open box of distilled water in the bottom shelf of the incubator. For live imaging experiments, ChoPs7 cultures were scaled-up in 75 cm^2 tissue-culture treated flasks (#130190, ThermoFisher Scientific) with 20 mL filter-sterilized 1X Artificial Seawater, 1% (v/v) Seawater Complete and 1% (v/v) *H. oceani* resuspended food pellet.

Culture in 5% (v/v) CGM3: ChoPs cultures were grown in 25 cm^2 tissue-culture treated flasks with 10 mL filter-sterilized 1X Artificial Seawater and 5% (v/v) CGM3 (see below), hereafter referred to as CGM3 medium, unless otherwise specified. Cultures were supplemented with 1% (v/v) *H. oceani* resuspended food pellet (see below) and kept in a 25°C Caron low temperature incubator equipped with a lamp (Venoya Full Spectrum 150W Plant Growth LED) controlled by a programmable timer (Leviton VPT24-1PZ Vizia) with 60% humidity under a 12-hour light-dark cycle.

C. flexa growth medium preparation

1X Artificial Seawater (hereafter ASW) was prepared by diluting 32.9 g of Instant Ocean (#218035, Aquarium Systems) in 1 L of ultrapure milliQ water and adjusting pH to 8.0 ± 0.1. The 1X ASW solution was filter-sterilized using a 0.22 µm pore-size filter (#SEGPU1145, Millipore). The resulting salinity of the pH-adjusted and sterile-filtered 1X ASW stock solution corresponds to 35 ppt. Sterility was tested by incubating a sealed 5 mL aliquot at 37ºC for 24 hours and visually assessing transparency.

100% stock of SWC growth medium was prepared by diluting 12 g of Instant Ocean, 1.5 mL Glycerol (#15523, Sigma-Aldrich), 2.5 g Bacto peptone (#211677, BD Difco) and 1.5 g Yeast extract (#212750, BD Difco) in 1 L ultrapure milliQ water. The 100% SWC solution was filter-sterilized using a 0.22 µm pore-size filter. A 5 mL aliquot was incubated at 37ºC during 24 hours to confirm sterility.

100% CGM3 was prepared by diluting 5 g of Cereal Grass (#IS5020, Basic Science SupplieS) into 1 L of 1X ASW directly from the autoclave. Media was filtered using a 150 mm filter paper (#1001-150, Whatman) placed in Buchner funnel (#60246, Coorstek) and vacuum filtered to remove large particles. This step was repeated a second time. Aliquots were made and filtered sterilized with 0.22 µm filter and vacuum line, and stored at room temperature.

H. oceani food pellet preparation

H. oceani food pellets were prepared by inoculating either 5 mL of an overnight pre-grown culture in 100% SWC (from a glycerol stock) or a single bacterial colony (from a pre-grown culture in an SWC-agar plate) into 500 mL of 100% SWC. The bacteria culture was then incubated at room temperature for ~2-3 days in a rocking shaker until OD reached ~0.6. Next, the 500 mL bacteria culture was distributed into 50 mL falcon tubes and harvested at 4000-5000xg for 30 minutes at 4ºC in a tabletop centrifuge. After centrifugation, the supernatant was removed by pouring the tubes and by additionally using a serological pipette to remove all excess liquid. Next, the bacterial mass of each tube was determined to calculate the resuspension volume of 1X ASW to reach a final bacteria concentration of 20 mg/mL and resuspended in 1X ASW by pipetting up and down. After resuspension, bacteria were distributed into 500 µL aliquots into 1.5 mL Eppendorf tubes. Finally, tubes were centrifuged at 16,000xg for 10 minutes at 4ºC and the supernatant was removed with a fine transfer pipette. Food pellets were flash frozen in liquid nitrogen and stored at -80ºC. Ready-to-use food pellets were prepared by resuspending a 10 mg/mL food pellet tube in 1 mL of 1X ASW.

Imaging *C. flexa* flagella-in and flagella-out sheets (related to Fig. 2.1B-D)

To image flagella-in sheets (Fig. 1B), about 1mL of ChoPs7 dense cultures grown in CGM3 medium were transferred into a FluoroDish (#FD35-100, World Precision Instruments) and incubated for 30 minutes to allow them to settle to the bottom of the plate. Colonies were imaged by differential interference contrast (DIC) microscopy using a C-Apochromat 63X/1.4 1.6X optovar Zeiss objective mounted on a Zeiss Observer Z.1 with Hamamatsu Orca Flash 4.0 V2 CMOS camera (C1140-22CU). Flagella-out sheets (Fig. 1D) were imaged as in (Brunet et al. 2019).

Tracking cell division of single cells (related to Fig. 2.1E-F and Movie S1)

The cell concentration of an exponentially growing ChoPs7 culture grown in SWC medium was estimated using the LUNA-II™ automated cell counter (LogosBiosystems). The culture was then diluted down to 1 cell/µL in 5% (v/v) SWC + 1% (v/v) *H. oceani* resuspended food pellet. 1 µL of the resulting diluted culture was pipetted onto the center of a well in a black 96-well ibiTreat µ-plate (#89626, Ibidi) and covered with 400 µL of Ibidi anti-evaporation oil (#50051, Ibidi). The sample was imaged with a Plan-Apochromat 20X/0.8 M27 Zeiss objective in a Zeiss Axio

Observer Z.1 Inverted Microscope, using the tile scan option to cover the whole surface of the droplet, Definite Focus, and a ColorBand filter (#FGL610, Thorlabs).

Mixed clonal/aggregative multicellularity timelapse (related to Fig. 2.1G, Fig. 2.S1 and Movies S2-S3)

Colonies grown in CGM3 medium were transferred into a FluoroDish (#FD35-100, World Precision Instruments) and incubated for 30 minutes to allow them to settle to the bottom of the plate. Colonies were imaged every 5 minutes by differential interference contrast (DIC) microscopy using a Plan-Apochromat 63X/1.4 Oil Zeiss objective mounted on a Zeiss Observer Z.1 with Hamamatsu Orca Flash 4.0 V2 CMOS camera (C1140-22CU) and "Time-lapse" option.

Aggregation dynamics over time (related to Fig. 2.2A and Movie S4)

Chops7 cultures were grown to maximal density in CGM3 medium. Colonies were transferred into 50 mL Falcon tubes and vortexed in "fast" setting on a Vortex Genie 2 for one minute to dissociate colonies into single cells. Single cells were concentrated by centrifugation to $3*10^5$ cells/mL, and 2 mL were transferred into a FluoroDish (#FD35-100, World Precision Instruments). Cells were imaged every 60 seconds for 1 hour 45 minutes using a C-Apochromat 10X/0.45 optovar 1.6X Zeiss objective mounted on a Zeiss Observer Z.1 with Hamamatsu Orca Flash 4.0 V2 CMOS camera (C1140-22CU).

Live imaging of dual labeling of aggregates (related to Fig. 2.2B and Movie 2.S5)

Around 40 mL of ChoPs7 cells from an exponentially growing culture grown in SWC medium were harvested at 3,300xg during 15 minutes at room temperature and washed twice with 40 mL of 1X ASW. Cells were then resuspended in ~1 mL of 1X ASW by pipetting up and down, dissociated by vortexing for 20 seconds and divided into two 1.5 mL Eppendorf tubes. Cells in each tube were stained with 1:1000 of either CellTrace™ CFSE (green) (#C34570, ThermoFisher Scientific) or CellTrace™ Far Red (magenta) (#C34572, ThermoFisher Scientific) (both from 5 mM stock solutions in DMSO) for 20 minutes at room temperature on a rocking shaker. After incubation, cells were quenched by adding 1% (v/v) Bovine Serum Albumin (BSA) (#BP9705-100, Fisher Scientific; from a 50 mg/mL stock solution in distilled water) for 1 minute at room temperature by gently inverting each tube. Next, cells were harvested at 3,300xg for 15 minutes at room temperature and washed once with 1 mL of 1% (v/v) BSA in 1X ASW and next with 1 mL of 1X ASW. Cells were finally resuspended in 500 µL of 1X ASW and counted using a LUNA-II™ automated cell counter (LogosBiosystems) (adjusting particle detection range to 1-15 µm using the "histogram" option) to estimate cell concentration. Before seeding, samples were vortexed again for 30 seconds to ensure dissociation into single cells. Green and magenta single cell populations were mixed in a 1:1 ratio and a final number of $2*10^5$ cells were seeded in 300 µL of 1X ASW in a black 96-well ibiTreat µ-plate (#89626, Ibidi). Cells were imaged every 3 minutes in

5 different positions by DIC and 4% intensity LEDs 488 nm and 650 nm with a Plan-Apochromat 20X/0.8 M27 Zeiss objective in a Zeiss Axio Observer Z.1 Inverted Microscope, using Definite Focus and a ColorBand filter (#FGL610, Thorlabs).

Airyscan imaging of dual labeling of aggregates (related to Fig. 2.2C, Fig. 2.S2A and Movies S6-S8)

Green and magenta single cell populations were stained as above, mixed in a 1:1 ratio, seeded in 1 mL of SWC medium in a 24-well plate (#3526, Corning) and incubated overnight in a 25ºC incubator (protected from light by a layer of aluminum foil). Non-mixed single-labeled populations of $2*10^5$ single cells were also seeded as controls. After incubation, 100 µL of colonies pipetted from the center of the well were pipetted with a truncated P200 filter tip and transferred to a black 96-well ibiTreat µ-plate (#89626, Ibidi) coated with 200 µL of 100 µg/mL Poly-D-Lysine hydrobromide (#P6407, Sigma-Aldrich; stock solution in distilled water; each well was washed twice with 200 µL distilled water prior to cell seeding). Cells were then incubated for 15 minutes at room temperature, fixed with 16% (v/v) ice-cold paraformaldehyde (PFA; #15710, Electron Microscopy Sciences) to a final concentration of 4% (v/v) PFA, and further incubated for 5 minutes at room temperature. Next, cells were permeabilized for 5 minutes at room temperature with 0.1% (v/v) Triton X-100 (#A16046, Thermo Fisher Scientific; from a 10% (v/v) stock solution in distilled water). Finally, cells were stained with 1:1000 Alexa Fluor™ Plus 405 Phalloidin at 2 units/µL pre-diluted in DMSO (#A30104, Invitrogen). Cells were then imaged with a Plan-Apochromat 40X/1.3 Oil DIC (UV) VIS-IR M27 Zeiss objective using Airyscan MPLX SR-4Y and 2X line averaging modes in an inverted Zeiss Axio Observer Z1/7 confocal microscope equipped with LSM900 Airyscan 2. All experiments were performed in two biological replicates.

Images were then processed using the “Airyscan process” option in the “Image Processing” menu of the Zen Blue software and analyzed with Imaris Imaging software version 9.9.1 (build 61122 for x64). The “Volume” tool was used to create a 3D rendering image, which was captured by the “Snapshot” option and movie recorder.

Fluorescence staining of aggregation dynamics over time (related to Fig. 2.2D-E, Fig. 2.S2B and Movies S9-S13)

Around 10-20 mL of ChoPs7 cells from an exponentially growing culture grown in SWC medium were harvested at 3,300xg during 15 minutes at room temperature and washed twice with 20 mL 1X ASW. Cells were then resuspended in ~1 mL 1X ASW by pipetting up and down, dissociated by vortexing for 20 seconds and counted to estimate cell concentration using a LUNA-II™ automated cell counter (LogosBiosystems) (adjusting particle detection range to 1-15 µm as before). Next, $2.2*10^5$ cells were seeded in 1 mL of 1X ASW in a 24-well plate and incubated for 10 minutes, 30 minutes, 2 hours, 6 hours and 24 hours in a 25ºC incubator. After incubation, 45 µL of cells were pipetted using a truncated P200 tip in a black 96-well ibiTreat µ-plate (#89626, Ibidi) pre-treated with 200 µL of 100 µg/mL Poly-D-Lysine hydrobromide

(#P6407, Sigma-Aldrich) (each well was washed twice with 200 µL of milliQ water prior to cell seeding), letting cells settle for 5-10 minutes at room temperature. Then, cells were fixed by addition of 16% (v/v) ice-cold PFA (#15710, Electron Microscopy Sciences) to a final concentration of 4% (v/v) PFA, and incubated for 5 minutes at room temperature. Next, cells were permeabilized for 5 minutes at room temperature using a 0.1% Triton X-100 solution (#A16046, ThermoFisher Scientific) added from a 10% (v/v) stock solution in distilled water, reaching a final concentration of 0.1% (v/v). Finally, cells were stained with a 10X dye mix solution diluted in 1X ASW containing 1:100 FM™ 4-64X at 5 mg/mL pre-diluted in milliQ water (#F34653, Invitrogen) and 1:100 Alexa Fluor™ 488 Phalloidin at 2 units/µL pre-diluted in DMSO (#A12379, Invitrogen), reaching a final concentration of 1:1000 each. Cells were then imaged with a Plan-Apochromat 40X/1.3 Oil DIC (UV) VIS-IR M27 and a Plan-Apochromat 63X/1.4 Oil M27 Zeiss objectives using Airyscan MPLX SR-4Y and 2X line averaging modes in a Zeiss Axio Observer Z1/7 equipped with LSM900 Airyscan 2 inverted microscope. All experiments were performed in two biological replicates.

Images were then processed using the "Airyscan process" option in the "Image Processing" menu of the Zen Blue software and later analyzed with Imaris Imaging software version 9.9.1 (build 61122 for x64). The "Volume" tool was used to create a 3D rendering image, which was captured by the "Snapshot" option and movie recorder. The "Surfaces" tool was used for image segmentation and individual cell counting.

Growth curve of Aphidicolin-treated single cells and colonies (related to Fig. 2.2F and Fig. 2.S3B)

Chops7 cultures grown in CGM3 medium were treated overnight with the cell proliferation inhibitor Aphidicolin (#38966-21-1, Santa Cruz Biotechnology) at 17 µg/mL or DMSO (drug vehicle), following a previous protocol used for the choanoflagellate *S. rosetta* (Fairclough, Dayel, and King 2010). To confirm that the drug worked as intended with *C. flexa*, we performed growth curves using different concentrations of the inhibitor (Aphidicolin 8 µg/mL, 10 µg/mL, and 17 µg/mL). Cells used for the growth curve were treated with Aphidicolin or DMSO and incubated overnight. The following morning, treated cells were seeded in 24-well plates at a concentration of $1*10^3$ cells/mL in 2.5% (v/v) CGM3 supplemented with 0.5% (v/v) *H. oceani* resuspended food pellet, in triplicates. Cells were fixed with 16% (v/v) ice-cold paraformaldehyde (#15710, Electron Microscopy Sciences) to a final concentration of 4% (v/v) and counted every 24 hours using the LUNA-II™ automated cell counter (LogosBiosystems) (adjusting particle detection range to 3-10 µm as before) for a total of 96 hours.

Quantification of aggregation in aphidicolin-treated cells (related to Fig. 2.2F and Fig. 2.S3A)

Chops7 cultures grown in CGM3 medium were treated with aphidicolin or DMSO (control) as detailed above and incubated overnight. The following morning, colonies were transferred into 50 mL Falcon tubes and vortexed in "fast" setting on a Vortex Genie 2 for one minute to dissociate colonies into single cells. Single cells were concentrated to $3*10^5$ cells/mL, and 200 µL

were transferred into an µ-slide 8-well chamber (#80826, Ibidi). Cells were imaged at 6 to 9 different locations per replicate every 30 minutes for 2 hours using a C-Apochromat 10X/0.45 optovar 1.6X Zeiss objective mounted on a Zeiss Observer Z.1 with Hamamatsu Orca Flash 4.0 V2 CMOS camera (C1140-22CU) using the "Tile positions" option. Cell aggregates area was quantified using ImageJ Imaging Software version 2.14 (Schindelin et al. 2012a). Tiled images were processed using the following commands with default settings in the following order: "*Smooth"* and *"Find Edges"* (from the *"Process"* menu)*; "Despeckle"* (in the *"Process"* menu)*, "Make Binary", "Dilate", "Erode", and "Fill Holes"* (from the "*Binary*" tool in the "*Process*" menu); and "*Analyze Particles"* (in the *"Analyze"* menu) to quantify areas.

Curaçao study area and sampling procedures (related to Fig. 2.3, Fig. 2.S4-S6, Table S1 and Movies S14-S16)

Fieldwork data was collected in the Shete Boka National Park, a protected area situated in Willemstad at the NW coast of Curaçao (12°22'5.718"N, 69°06'56.916"W) (Fig. 2.3A-B and Fig. 2.S4A-B) in July and August 2023 (*Exped-A* and *Exped-B*). The park covers almost 10 km of the rocky wave-exposed northern coast of the island, and contains approximately 10 pocket bays, or "*bokas*".

For *Exped-A,* at least 10 mL of seawater were collected from 79 different splash pools in 25 cm^2 tissue culture flasks along ~2 km in the coast of the park, ranging from Boka Wandomi to Boka Pistol (Fig. 3D). 15 of these splash pools were randomly selected to monitor splash pool evaporation and refilling cycles every day over an 8-day timecourse (Fig. 2.3D and Fig. 2.S6). We identified each splash pool using a physical tagging system and its geographic position, recorded using the GPS of an iPhone 12 Mini (Apple). An image of each splash pool and its surrounding environment was also taken using the camera of an iPhone 12 Mini (Apple). The following parameters were measured onsite: seawater salinity using a refractometer (#B07FQPFJGX (ASIN), Gain Express) (Fig. 2.3E,H, and Fig. 2.S4,S6), splash pool seawater or soil (when dry) (Fig. 2.3I-J and Movie S16) temperature using a thermometer (#B07CB8JG21 (ASIN), ThermoPro), and seawater depth using measuring tape. Presence of sheets was later visually assessed using a Leica inverted microscope (Leica DMIL LED) equipped with a Nikon camera (Nikon Z 50) at the CARMABI biological station in Curaçao (Fig. 2.3F, Fig. 2.3I-J, Fig. 2.S5A-C, Fig. 2.S7 and Movie S15). Seawater salinity and temperature from the open sea were measured in the bokas of *Boka Wandomi* and *Boka Kalki* as controls.

For *Exped-B,* a random number generator was used to select a randomized sampling location between 150 and 250 m upstream *Boka Wandomi*, avoiding previous sampling sites analyzed in *Exped-A* (Fig. 2.3D). The sampling location selected was 204 m upstream *Boka Wandomi*, where an area of 10 by 4 meters was defined. All splash pools containing at least 5 mL of seawater within that area were collected and analyzed as above.

Soil rehydration of splash pools (related to Fig. 2.3I-J, Table S1 and Movie S16)

Soil samples of six splash pools that underwent complete desiccation surveyed in *Exped-A* (Sp6, Sp12, Sp15, Sp43, Sp69 and Sp70) were scraped and collected in a 25 cm^2 tissue-culture treated flasks daily during 8-days using a spatula, making sure to obtain soil from various areas to maximize sample representativity (Movie S16). Soil samples were then rehydrated in the laboratory with 50-100 mL of sterile-filtered seawater collected from Boka Wandomi (using a 0.22 µm pore-size filter (#SLGP033RS, Millex®-GP)), adjusting the rehydration volume to reach a salinity of ~40 ppt. Presence of sheets was monitored daily during the next five days using a Leica inverted microscope (Leica DMIL LED) equipped with a Nikon camera (Nikon Z 50) at the CARMABI biology station in Curaçao.

Manual isolation of field sheets (related to Fig. 2.S5A-C)

To start cultures of newly collected *Choanoeca flexa* from individual sheet colonies (single-sheet-bottlenecked, or SSB), we manually isolated single sheets from Sp44, Sp60, and Sp61 (Exped-B) splash pool samples as follows: for each sample, a first round of sheet isolation was performed by distributing 2 mL of each splash pool sample in various wells in a 6-well plate. Individual sheets were manually pipetted in a 0.2 µL volume and transferred into a new 6-well plate containing 2 mL of 1X ASW per well. Individual sheets were then transferred at least twice more into a new well of a 6-well plate (same volume and medium) to dilute away potential contaminants. Multiple sheets from the same splash pool were then manually pipetted again (in a 0.2 µL volume) and transferred into clean 25 cm^2 tissue-culture treated flasks containing 20 mL of filtered seawater from Boka Wandomi and supplemented with 0.5% (v/v) *H. oceani* resuspended food pellet. Cultures were then seeded from individual sheets via a second round sheet isolation performed as before: pipetting of one individual sheet, at least two washes in a 6-well plate, and finally transfer into a new 25 cm^2 tissue-culture treated flask (containing 10 mL of SWC medium supplemented with 1% (v/v) *H. oceani* resuspended food pellet). Flasks were then maintained in SWC medium in a 25ºC incubator under a 12-hour light-dark cycle.

To start single-cell-bottlenecked (or clonal) cultures of newly collected *Choanoeca flexa,* we performed Fluorescence Activated Cell Sorting (FACS) of previously established single-sheet-bottlenecked (SSB) cultures from Sp44 and Sp60 (Exped-B) as follows. For each SSB culture, around 40 mL of exponentially-growing cells in SWC medium were harvested at 3300xg during 15 minutes at room temperature and resuspended in ~3 mL of 1X ASW by pipetting up and down. Sheets were then dissociated by vortexing the culture for 20 seconds and by adding 2.5 mM EGTA (#11453097, ThermoFisher Scientific, pre-diluted in milliQ water) to the cell suspension. Single cells were sorted into individual wells using a MoFlo Astrios Cell Sorter (Beckman Coulter) in three different 96-well tissue-culture treated plates (#229195, Cell Treat) containing 200 µL of 1X ASW (with 0.1% (v/v) SWC and 0.5% (v/v) *H. oceani*) per well. We performed an additional washing step with 1X ASW between samples during sorting to avoid cross-contamination. Single-cell-bottlenecked clonal cultures were grown in the 96-well plates

for 6 days and expanded into a 75 cm^2 tissue-culture treated flask containing SWC medium supplemented with 1% (v/v) *H. oceani.*

18S rDNA sequencing (related to Fig. 2.S5D and Supplementary Files S1-S4)

gDNA was extracted from previously established single-sheet-bottlenecked and clonal cultures as follows. Around 40 mL of each exponentially-growing culture in SWC medium were harvested at 3300xg during 15 minutes at room temperature and directly resuspended in 30-120 µL of DNAzol®Direct (#DN131, Molecular Research Center). Cell lysis was promoted by pipetting up and down and incubating the lysates at room temperature for at least 30 minutes.

The 18S ribosomal DNA (18S rDNA) locus was amplified by PCR with Q5® High-Fidelity DNA Polymerase (#M0491L, New Englands Biolab) and degenerate primers (sequences in Table S2). We followed the same nested PCR program used in (Brunet et al. 2019). For the first round of PCR, we used 2.5 µL of gDNA (directly from the DNAzol-containing tubes) as template. For the nested PCR, we used 0.5 µL of the first PCR as template. Both forward and reverse primers from the nested PCR, and an additional forward primer (named "Sequencing", see Table S2), were used for Sanger sequencing.

18S rDNA sequences from newly isolated single-sheet-bottlenecked and clonal sheet cultures as well as other opisthokonts (including the previously published *C. flexa* 18SrDNA sequence (see File S1) (Brunet et al. 2019)) were analyzed following a custom phylogenetic workflow using NGPhylogeny.fr (Lemoine et al. 2019; Dereeper et al. 2008). First, sequences were aligned with MAFFT v.7467 L-INS-i under default parameters (File S2), and trimmed with gBlocks v.091b (Castresana 2000) under minimally stringent default parameters (File S3). Then, a Maximum Likelihood phylogenetic tree was produced using PhyML v3.3.20190909 (Guindon and Gascuel 2003; Guindon et al. 2010) with the GTR model, empirical nucleotide equilibrium frequencies, estimated transition/transversion ratio, optimized proportion of invariable sites, estimated gamma model (4 categories), optimized parameter for tree topology, branch length and model parameter, and a mix of NNI & SPR tree search method (File S4). The resulting 18S rDNA tree was visualized and edited with FigTree v.1.4.4 (http:// tree.bio.ed.ac.uk) and further edited with Adobe Illustrator CC 2017 to generate the tree figure.

Artificial gradual evaporation of splash pool samples (related to Fig. 2.S7)

3 mL of splash pool sample collected from Sp64 (Exped-A) were seeded in a 6-well plate (#130184, ThermoFisher Scientific) and left over the bench at room temperature (between 25-28ºC), without the lid of the plate to promote gradual evaporation. Presence of sheets was monitored daily during the next six days using a Leica inverted microscope (Leica DMIL LED) equipped with a Nikon camera (nikon Z 50) at the CARMABI biology station in Curaçao.

Artificial gradual evaporation experiment (related to Fig. 2.4A-B, Fig. 2.S8-S10 and 2.S12, and Movie S17)

3 mL of dense ChoPs7 cells grown in SWC medium were seeded in four separate 6-well plates (#130184, ThermoFisher Scientific) and transferred over a grid in a 30ºC incubator. One 6-well plate was kept with its lid on (low-evaporation control) and the rest of plates were kept without lid (gradual evaporation condition) over a 9-day time course. A plastic box (dimensions: 35.7 cm x 23.5 cm x 13.5 cm) was installed over the plates to allow air-exchange while reducing contamination from potentially falling microscopic particles in ambient air (Fig. 2.S8B). At every timepoint, a 50 µL sample was used to measure salinity increase using a refractometer (#B07FQPFJGX (ASIN), Gain Express). An additional 100 µL sample was transferred to a black 96-well ibiTreat µ-plate (#89626, Ibidi) coated with poly-D-lysine (as above). The number of single cells and sheets was quantified from at least 16 images per timepoint, captured with a Plan-Apochromat 20X/0.8 M27 Zeiss objective in a Zeiss Axio Observer Z.1 Inverted Microscope, using a ColorBand filter (#FGL610, Thorlabs).

The number of cells per sheet was estimated based on sheet area, using the following method: first, cells were manually counted and area was measured in 27 sheets ranging from 2 to 96 cells. Then, the estimated average area of a cell was calculated from that sample. Linear regression of sheet area over cell number yielded a regression coefficient r^2=0.98, indicating that sheet area is as a good approximation a linear function of cell number. In the rest of the analysis, the number of cells per sheet was estimated from the sheet area. Doublets of cells were excluded from the final analysis, because their frequency was highly variable, and because they could result from either aggregation or clonal cell division, which might not necessarily reflect multicellular development. Once complete desiccation was achieved (at ~4 days of incubation) all dry samples in the "gradual evaporation condition" were rehydrated with 3 mL 1X ASW, transferred to a 25ºC incubator with the plate lid on together with the low-evaporation control samples, and monitored daily as before. A negative control flask filled with 3 mL 1X ASW and 3 mL of 5% (v/v) SWC (without cells) was prepared and visually inspected under a Leica DM IL LED microscope to confirm that the 1X ASW stock used for rehydration was not contaminated with ChoPs7 cells (or other cells). All experiments were performed in two biological replicates.

Live imaging of sheet dissociation during gradual evaporation (related to Fig. 2.S10 and Movie S17)

3 mL of dense ChoPs7 cells grown in SWC medium were seeded in three separate 6-well plates (#130184, ThermoFisher Scientific) and placed over a grid in a 30ºC incubator. The plates were kept without lid (gradual evaporation condition) to let samples evaporate gradually (see *"Gradual evaporation experiment"* section). Evaporation was monitored until the samples reached 82 ppt salinity (about 48 hours after the beginning of the experiment). At that point, 600 µL of culture were pipetted from the bottom of a well and transferred onto a black 96-well ibiTreat µ-plate (#89626, Ibidi). The samples were imaged every minute for 24 hours with a

Plan-Apochromat 20X/0.8 M27 Zeiss objective in a Zeiss Axio Observer Z.1 Inverted Microscope, using the tile scan option, definite focus mode and a ColorBand filter (#FGL610, Thorlabs).

The lid of the plate was kept on throughout the experiment, except for 2 intervals of 1 hour each (after 3-4 hours and 5-6 hours since the start of the timelapse, to maintain some degree of evaporation). At the end of the experiment, salinity had reached 105 ppt. The timelapse was binarized and analyzed with Fiji version 2.14.0/1.54g (Schindelin et al. 2012a). First, the timelapse (composed of 2 different stacks) was converted to 8 bits using the "Type" option and duplicated using the "Duplicate" option in the "Image" menu. Next, the image brightness was homogenized by first applying a Gaussian blur filter, setting the radius value at 100, in the duplicated stacks using the "Filter" option in the "Process" menu. Next, the "Calculator Plus" option in the "Process" menu was used to finalize homogenizing image brightness, using the original stacks and the duplicated Gaussian-filtered stacks in the operation setting the following parameters: i1=original stacks, i2=blurred stacks, Operation=Divide, k1=150 (average intensity of image). Intensity boundaries were later adjusted to remove shadows of bacterial biofilm and only leave choanoflagellate cells visible. Finally, the timelapse was binarized, closed and dilated using the "Make Binary", "Close", and "Dilate" options in the "Binary" tool from the "Process" menu.

Live imaging of cell rehydration after gradual evaporation (related to Fig. 2.4C and Movie S18)

3 mL of dense ChoPs7 cells grown in SWC medium were seeded in three separate 6-well plates (#130184, ThermoFisher Scientific) and transferred over a grid in a 30ºC incubator. The plates were kept without lid (gradual evaporation condition) to let samples evaporate gradually (see *"Gradual evaporation experiment"* section). Samples were monitored until complete desiccation (reached about 72 hours after the beginning of the experiment). The samples were then rehydrated with 3 mL of 1X ASW per well. Cyst-like cells were collected from the bottom of the wells using a cell scraper (#08-100-241, Fisher Scientific) and 600 µL of culture containing cysts were transferred onto a black 96-well ibiTreat µ-plate (#89626, Ibidi). The samples were imaged every minute over night with the plate lid on with a Plan-Apochromat 20X/0.8 M27 Zeiss objective mounted on a Zeiss Axio Observer Z.1 Inverted Microscope, using the definite focus mode and a ColorBand filter (#FGL610, Thorlabs).

Loss of multicellularity micrographs after salinity increase by direct addition of salt (related to Fig. 2.S11A-C)

Around 40 mL of ChoPs7 cells from an exponentially growing culture grown in SWC medium were harvested at 3,300xg for 15 minutes at room temperature, washed twice with 20 mL of 1X ASW, vortexed for 30 seconds, and counted to estimate cell concentration using the LUNA-II™ automated cell counter (LogosBiosystems) (adjusting particle detection range to 1-15 µm as before). Next, $1*10^4$ cells were seeded in 1.2 mL of SWC medium (at 1X salinity) in a 12-well plate (#130185, ThermoFisher Scientific) and grown in a 25ºC incubator for 6 days. After 3 days

of growth in 1X salinity, we gradually increased salinity by 1X every day by addition of a 10X ASW stock solution until reaching either 3X or 4X salinity. A 1X salinity condition (without salt addition) was also used as a control. Samples were imaged on the 6th day after having spent a total of 6 days at 1X salinity, 2 days at 3X salinity or 1 day at 4X salinity after gradual increase of salinity by addition of salt. 100 µL of sample in each condition were transferred to poly-D-lysine-coated 96-well plate (see above) and imaged by DIC microscopy with a C-Apochromat 40X/1.2 W Corr M27 Zeiss objective in a Zeiss Axio Observer Z.1 Inverted Microscope, using a ColorBand filter (#FGL610, Thorlabs).

Growth rate during gradual evaporation (related to Fig. 2.4D and Fig. 2.S12)

Around 40 mL of ChoPs7 cells from an exponentially growing culture grown in SWC medium were counted to estimate cell concentration using a LUNA-II™ automated cell counter (LogosBiosystems) (adjusting particle detection range to 1-15 µm as before). Next, 2.5*10^5 cells were seeded in 3 mL of SWC medium in four separate 6-well plates (#130184, ThermoFisher Scientific) without lid and incubated at 30ºC during a 5-day time course to let samples evaporate gradually (see *"Gradual evaporation experiment"* section). Two additional 6-well plates were kept with their lid on as low-evaporation controls. Sample volume, salinity and cell number were quantified daily as before. Lids of plates in "gradual evaporation" condition were closed to stop evaporation once samples reached either 2X or >3X salinity compared to 1X control samples. All experiments were performed in three biological replicates, including at least two technical replicates per condition. The growth rate in each condition was calculated over the 5-day time interval as follows:

$$growth\ rate\ = \frac{log_2(\frac{N_t}{N_0})}{T}$$

where N_t corresponds to the number of cells at the final timepoint (t); N_0 corresponds to the initial number of cells at time 0; and T corresponds to the time interval between the final timepoint (t) and time 0.

Cyst-like cell development micrographs (related to Fig. 2.4E)

Cyst-like cell development was monitored by capturing images every day during a four-day period. Images were acquired in the morning of each day by differential interference contrast (DIC) microscopy using C-Apochromat 40X/1.1 Water, C-Apochromat 63X/1.4 Oil, or C-Apochromat 100X/1.4 Oil Zeiss objectives mounted on a Zeiss Observer Z.1 with Hamamatsu Orca Flash 4.0 V2 CMOS camera (C1140-22CU). Around 200 mL of Chops7 cultures grown to high density in 1X ASW (33-35 ppt salinity) and CGM3 medium were transferred into a Bio-Assay Dish (#240845, Thermo Scientific). On the first day, the culture was placed in a 28°C incubator with the lid partially open to allow gradual evaporation. Around 4-6 hours later, when salinity had reached 60 ppt, the lid was closed overnight to allow cells to adapt to the new salinity, and the temperature was then set to 29ºC. On the morning of the 2nd day, the lid was partially

opened, and gradual evaporation resumed during the day until salinity reached 80 ppt. The lid was closed overnight, and the temperature was set to 30ºC. On the 3rd day, the lid was opened until salinity reached 100-110 ppt (equivalent to that of 3X ASW). The culture was incubated in 3X ASW for 24 hours to allow more cells to transition into cyst-like cells. On the 4th day, cells were imaged in the morning. For imaging purposes, on each day, 2 mL of the culture was transferred into a FluoroDish (#FD35-100, World Precision Instruments) pre-treated with poly-D-lysine. The sheets/single cells were incubated for 30 minutes to allow them to settle to the bottom of the plate before imaging.

F-actin staining in cyst-like cells (related to Fig. 2.4F-G and Fig. 2.S13)

About 40 mL of ChoPs7 cells from an exponentially growing culture grown in SWC medium were counted to estimate cell concentration using a LUNA-II™ automated cell counter (LogosBiosystems) (adjusting particle detection range to 1-15 µm as before). Next, $7*10^5$ ChoPs7 cells were seeded in 3 mL of SWC medium in four separate 6-well plates (#130184, ThermoFisher Scientific) without lid and incubated at 30ºC to let samples evaporate gradually (see *"Gradual evaporation experiment"* section). Two additional 6-well plates were kept with the plate's lid on as low-evaporation controls. Samples were monitored daily and salinity was measured after 4 days of incubation. Next, samples were scraped, homogenized and collected in a 1.5 mL Eppendorf tube. 1 mL of the low-evaporation control sample (flagellates) was directly transferred to an Eppendorf tube. All tubes were centrifuged at 3,300xg for 15 minutes at room temperature. Supernatant was carefully removed and samples were resuspended with 375 µL 1X ASW. The low-evaporation control sample was additionally vortexed for 30 seconds to dissociate sheets into single cells. Then, all samples were fixed with 16% (v/v) ice-cold paraformaldehyde (#15710, Electron Microscopy Sciences), reaching a final concentration of 4% (v/v), and incubated for 5 minutes at room temperature. Next, 100 µL sample were seeded in a black 96-well coated with poly-D-lysine and permeabilized with 0.1% Triton X-100 (as above). Finally, cells were stained with a 10X dye mix solution diluted in milliQ water containing 1:100 FM™ 4-64X (from a 5 mg/mL stock solution in distilled water; #F34653, Invitrogen), 1:100 Alexa Fluor™ 488 Phalloidin (from a 2 units/µL stock solution in DMSO; #A12379, Invitrogen), and 1:100 Hoechst (from 1 µg/mL stock solution; #H21486, Invitrogen) as before, reaching a final concentration of 1:1000 (compared to the stock solution) for each dye. Samples were imaged with a Plan-Apochromat 40X/1.3 Oil DIC (UV) VIS-IR M27 Zeiss objective using Airyscan MPLX SR-4Y and 2X line averaging modes on a Zeiss Axio Observer Z1/7 equipped with LSM900 Airyscan 2 inverted microscope. All experiments were performed in two biological replicates.

Images were processed using the "Airyscan process" option in the "Image Processing" menu of the Zen Blue software and later analyzed with Fiji Imaging Software version 2.9.0/1.53t (Schindelin et al. 2012b). A line was drawn transversally at the equatorial plane of each cell and in the F-actin channel using the "Straight line" tool in the Fiji toolbar. Then, the linescan profile of F-actin fluorescence intensity across the cell was displayed using the "Plot Profile" tool in the "Analyze" menu.

Nucleus-to-cytoplasm ratio calculation (related to Fig. 2.4H and Fig. 2.S14)

About 20 mL of ChoPs7 cells from an exponentially growing culture grown in SWC medium were harvested at 3300xg during 15 minutes at room temperature and counted to estimate cell concentration using the LUNA-II™ automated cell counter (LogosBiosystems) (adjusting particle detection range to 1-15 µm as before). Next, $6*10^5$ ChoPs7 cells were seeded in 3 mL of SWC medium in two separate 6-well plates (#130184, ThermoFisher Scientific) without lid and incubated at 30ºC to let samples evaporate gradually until complete desiccation (see *"Gradual evaporation experiment"* section). An additional 6-well plate was kept with its lid on as a low-evaporation control. Samples were monitored daily until complete desiccation was achieved after ~48 hours incubation. All 6-well plates were incubated an extra 24 hours at 30ºC with their lid on. Next, desiccated plates were rehydrated with 1 mL 1X ASW, and samples were scraped, homogenized and collected in an Eppendorf tube. 1 mL of the low-evaporation control sample (flagellates) was directly transferred to an Eppendorf tube. All tubes were centrifuged at 3,300xg for 15 minutes at room temperature. Supernatant was carefully removed and samples were resuspended with 500 µL 1X ASW. The low-evaporation control sample was additionally vortexed for 30 seconds to dissociate sheets into single cells. Then, all samples were fixed by addition of 16% (v/v) ice-cold PFA (#15710, Electron Microscopy Sciences) to a final concentration of 4% (v/v), and incubated for 5 minutes at room temperature. Next, 100 µL of each sample were mounted in a poly-D-lysine-coated 96-well plate, permeabilized and stained with FM 4-64FX, Alexa 488-phalloidin and Hoechst as above. At least 10 cells in each condition were imaged with a Plan-Apochromat 40X/1.3 Oil DIC (UV) VIS-IR M27 Zeiss objective using Airyscan MPLX SR-4Y and 2X line averaging modes in a Zeiss Axio Observer Z1/7 equipped with LSM900 Airyscan 2 inverted microscope. All experiments were performed in three biological replicates.

Images were processed using the "Airyscan process" option in the "Image Processing" menu of the Zen Blue software and later analyzed with Imaris Imaging software version 9.9.1 (build 61122 for x64). The "Volume" tool was used to create a 3D rendering image. The "Surfaces" tool was used for image segmentation and quantification of the volumes and sphericity values of the cell body (excluding collar and flagella) and nucleus of each individual cell. The nucleus-to-cytoplasmic ratio (N:C) was calculated as follows:

$$N{:}C\ ratio\ = \frac{Nucleus\ Volume}{Cell\ Volume\ -\ Nucleus\ Volume}$$

Growth rate during gradual salinity increase by the addition of salts (related to Fig. 2.S11D-E)

Around 40 mL of ChoPs7 cells from an exponentially growing culture grown in SWC medium were harvested at 3,300 xg for 15 minutes at room temperature, washed twice with 20 mL of 1X ASW, vortexed for 30 seconds, and imaged using a LUNA-II™ automated cell counter (LogosBiosystems). In this experiment, we did not adjust particle detection range with the histogram option (as stated above). Instead, images generated by the cell counter were

exported and cells were counted with a batch processing quantification using a macro script in the Fiji Imaging Software version 2.14.0/1.54g (Schindelin et al., 2012). In brief, the "Smooth" tool and the "Substract Background" tool (setting a rolling ball radius to 50) from the "Process" menu were first applied; images were then converted to binary with the "Convert to Mask" command from the "Binary" tool in the "Process" menu using the default parameters. Images were then analyzed using the "Analyze Particles" command to calculate the area of each particle, setting the analysis parameters to a particle size range of 20-100 µm2 and a circularity of 0.01-1, excluding particles on the edges of the images. Next, $1*10^4$-$1.2*10^4$ cells were seeded in 1.2 mL of SWC medium (at 1X salinity) in a 12-well plate (#130185, ThermoFisher Scientific) and grown in a 25ºC incubator for 6 days. Salinity was increased to 3X or 4X salinity by addition of salt as above. A 1X salinity condition (no salinity increase by the addition of salts) was used as a control. Presence of sheets and single cells (flagellates or cyst-like cells) was monitored daily. Sample volume, salinity and cell number were quantified daily as before. The growth rate in each condition was calculated considering the 3-day time interval during which salinity was gradually increased (from day 3 until day 6) as before. All experiments were done in two biological replicates, including two technical replicates per condition.

Survival of cyst-like cells and flagellates during desiccation (related to Fig. 2.5A and Fig. 2.S15)

Survival of cyst-like cells from desiccation was scored in the following way: first, cyst-like cells were produced by seeding 4 mL of dense ChoPs7 culture grown in SWC medium in each well of a 6-well plate (#130184, ThermoFisher Scientific) that was placed without lid in a 30ºC incubator (see *"Gradual evaporation experiment"* section). Cells were visually inspected and were found to have switched to a cyst-like morphology after 48 hours, and samples to have fully evaporated after 72 hours. Then, cyst-like cells were rehydrated with 4 mL 1X ASW and transferred to a 25ºC incubator with 60% humidity. At 8 days post-rehydration, all wells contained abundant and actively swimming sheet colonies, and cells were counted using the usual protocol using a LUNA-II™ automated cell counter (LogosBiosystems).

Survival of flagellate cells from desiccation was scored in the following way: 0.5 mL of dense ChoPs7 culture grown in SWC medium were seeded in each well of a 6-well plate (same reference as above) and placed in a 30°C incubator with the lid off. Evaporation was complete after 21 hours. Desiccated cells were visually inspected and were observed to not have switched to a cyst-like morphology but instead to have retained a visible flagellum and collar and to remain connected to each other by their microvilli. Desiccated flagellates were rehydrated with 0.5 mL 1X ASW and transferred to a 25ºC incubator with 60% humidity. At 8 days post-rehydration, no living cell was observed in any of the wells, and the LUNA-II™ automated cell counter (LogosBiosystems) did not detect any cell either.

To image desiccated sheets, 1 mL of dense Chops7 culture was seeded onto a FluoroDish (#15159112, Fisher Scientific) transferred to a 30ºC incubator without its lid and incubated overnight for rapid evaporation. After 24 hours the sample was completely desiccated. For imaging, the sample was rehydrated with 1 mL 1X ASW and immediately imaged by DIC with a

C-Apochromat 63X/1.20 W corr UV-VIS-IR (#421787-9970-000, Zeiss) in a Zeiss Axio Observer Z.1 Inverted Microscope.

Quantification of prey capture (related to Fig. 2.5B-C)

Bacterial staining: A *H. oceani* food pellet (20 mg) was resuspended in 1 mL of 1X ASW. Bacteria were stained using the fluorescent dye BactoView-Live Green [FITC] (#40102, Biotium) at a concentration of 2X (4 µL per mL) and incubated at room temperature for 30 minutes in the dark. To wash the unincorporated dye away, the stained bacteria were centrifuged at 2,750xg for 5 minutes, and the supernatant was carefully removed with a transfer pipette. The stained bacterial pellet was resuspended in 1mL of 1X ASW. Capture prey assay: *C. flexa* cultures were grown to high density in CGM3 medium. To assess colony capture efficiency, 200 µL of colonies were transferred into µ-slide 8-well chambers (#80826, Ibidi), and incubated for 30 minutes. In parallel, to obtain single cells, we transferred part of the culture into a 15 mL falcon tube and vortexed with the "fast" setting on a Vortex Genie 2 for 1 minute to dissociate colonies into single cells. Cells were allowed to recover from mechanical stimulation for 5 minutes before transferring them into µ-slide 8-well chambers (#80826, Ibidi). Bacteria were diluted 1:20 in 1X ASW, and 100 µL were added to each of the wells containing colonies or single cells. *C. flexa* was incubated in the presence of bacteria for 1 minute before fixing the samples with 16% (v/v) ice-cold paraformaldehyde (#15710, Electron Microscopy Sciences) to a final concentration of 4% (v/v). After fixation, we waited 30 minutes for the colonies and 2 hours for the single cells to settle to the bottom of the plate before imaging. Imaging and quantification: Colonies and single cells were imaged by differential interference contrast (DIC) microscopy and green fluorescence to visualize stained bacteria using a C-Apochromat 40X/1.1 optovar 1.6X Water Zeiss objective in a Zeiss Observer Z.1 with Hamamatsu Orca Flash 4.0 V2 CMOS camera (C1140-22CU). To quantify capture efficiency, we calculated the ratio between the number of bacteria attached to the collar of choanoflagellate cells over the total number of choanoflagellate cells in each picture. We quantified at least ~100 choanoflagellate cells per technical replicate in each condition. All experiments were performed in technical and biological triplicates.

Statistical analyses (related to Fig. 2.3E, Fig. 2.4D and 2.4H, Fig. 2.5A-B, Fig. 2.S11E and Fig. 2.S14C-D)

The significance of differences in one-to-one comparisons were tested using the non-parametric Mann-Whitney U test. Shapiro-Wilk normality test and F-test were examined to assess the distribution of the data and the differences in variances between conditions, respectively. All statistical analyses were performed using the R Stats Package version 3.6.3 (R Core Team, n.d.).

Figures

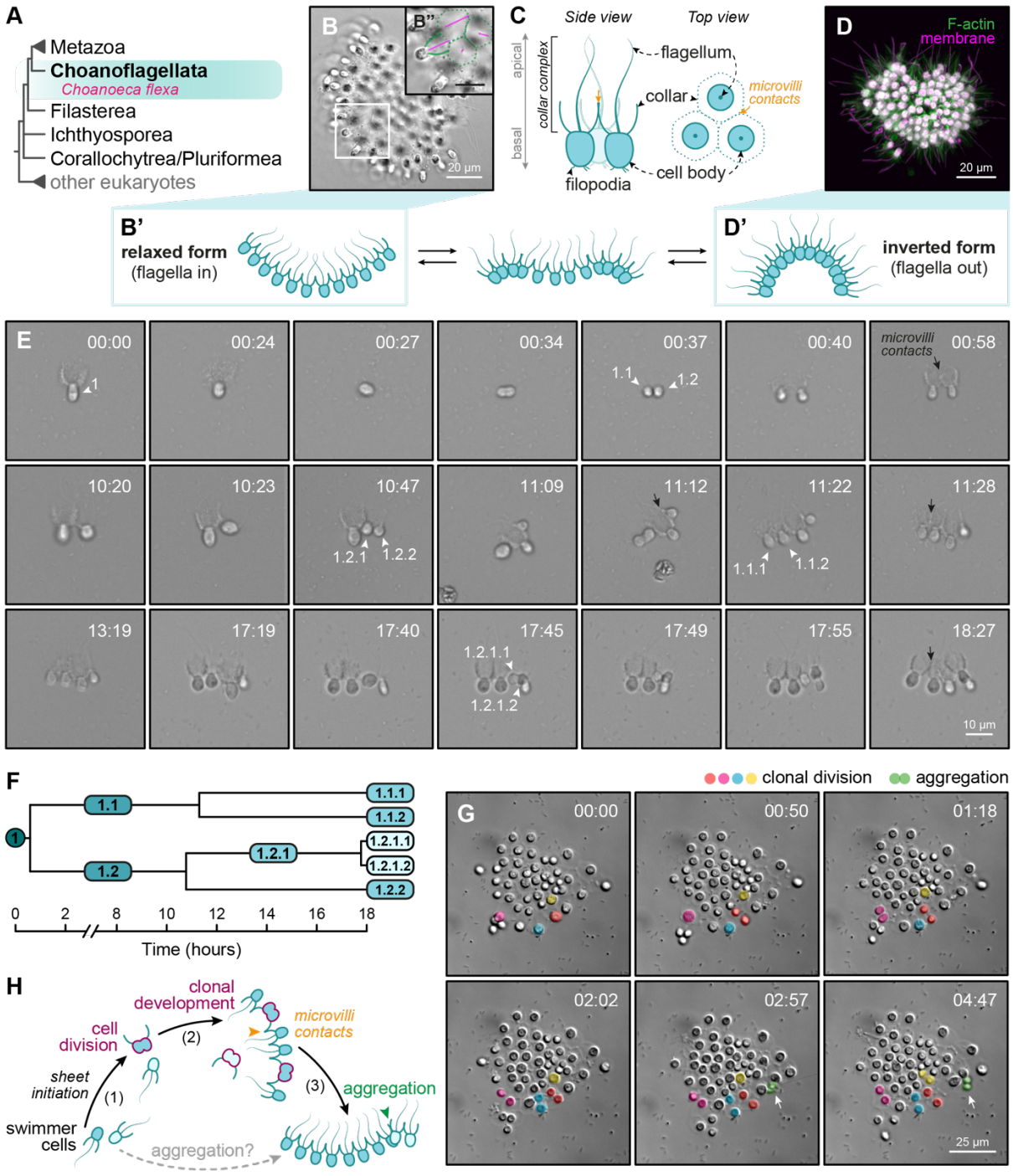

Figure 2.1. *Choanoeca flexa* can develop clonally but also displays aggregative features. (**A**) Choanoflagellates (turquoise) are the sister group to animals (Metazoa). The phylogenetic relationships depicted are based on several recent phylogenomic studies (Hehenberger et al. 2017; Ocaña-Pallarès et al. 2022; Brunet and King 2017; Fairclough et al. 2013; Brunet et al.

2019; Grau-Bové et al. 2017; King et al. 2008; Torruella et al. 2015). Uncertain positions are represented with polytomies. (**B**) Brightfield image of a *C. flexa* multicellular colony ("sheet") in its relaxed conformation (**B'**). **B"**, white square: zoom-in showing flagella (magenta pseudocolor) and direct cell-cell contacts between collars (green pseudocolor). Scale bar in B'': 10 µm. (**C**) Diagnostic morphological features of a choanoflagellate cell. *C. flexa* cells within a sheet are linked by their collars (orange arrow). (**D**) 3D reconstruction of an Airyscan Z-stack of a fixed sheet exhibiting an inverted conformation (**D**'), with cell bodies stained with a membrane/cytoplasmic dye (FM^{TM} 1-43FX, magenta, which distributes to the membrane and cytoplasm of cells following fixation), and microvilli stained with a filamentous actin (F-actin) dye (phalloidin Alexa 488, green). (**E**) Stills from a brightfield timelapse movie of clonal *C. flexa* sheet development by serial cell division from a single *C. flexa* swimmer cell (white arrowhead). After each division, the sister cells remain adhered to each other by direct cell-cell contacts between collars (black arrow). Note that cells retract their flagellum during division. Time scale hh:mm. (**F**) Cell lineage tracing as a function of time in E shows that cells divide asynchronously during colony formation, taking ~8-10 hours between each round of division. (**G**) Stills from a brightfield timelapse movie depicting a medium-sized *C. flexa* sheet (flagella-in conformation) that expands in cell number both by cell division (pseudocoloring in orange, pink, blue and yellow) and by cellular aggregation (white arrow, pseudocoloring in green). Time scale hh:mm. (**H**) Schematics of *C. flexa* mixed clonal-aggregative multicellularity development observed under laboratory culture conditions: (1) unicellular flagellate (swimmer) cells can divide clonally to initiate a colony; in turn, colonies can increase in cell number by (2) clonal division and (3) cellular aggregation (green arrowhead). In all cases, sister cells resulting from cell division or independent cells attaching to colonies by cellular aggregation adhere to each other through direct cell-cell contacts in their collar (orange arrowhead). The hypothesis that *C. flexa* sheets might be able to develop purely by aggregation is tested in Figure 2.2. Figure related to Figure 2.S1 and movies S1-S3.

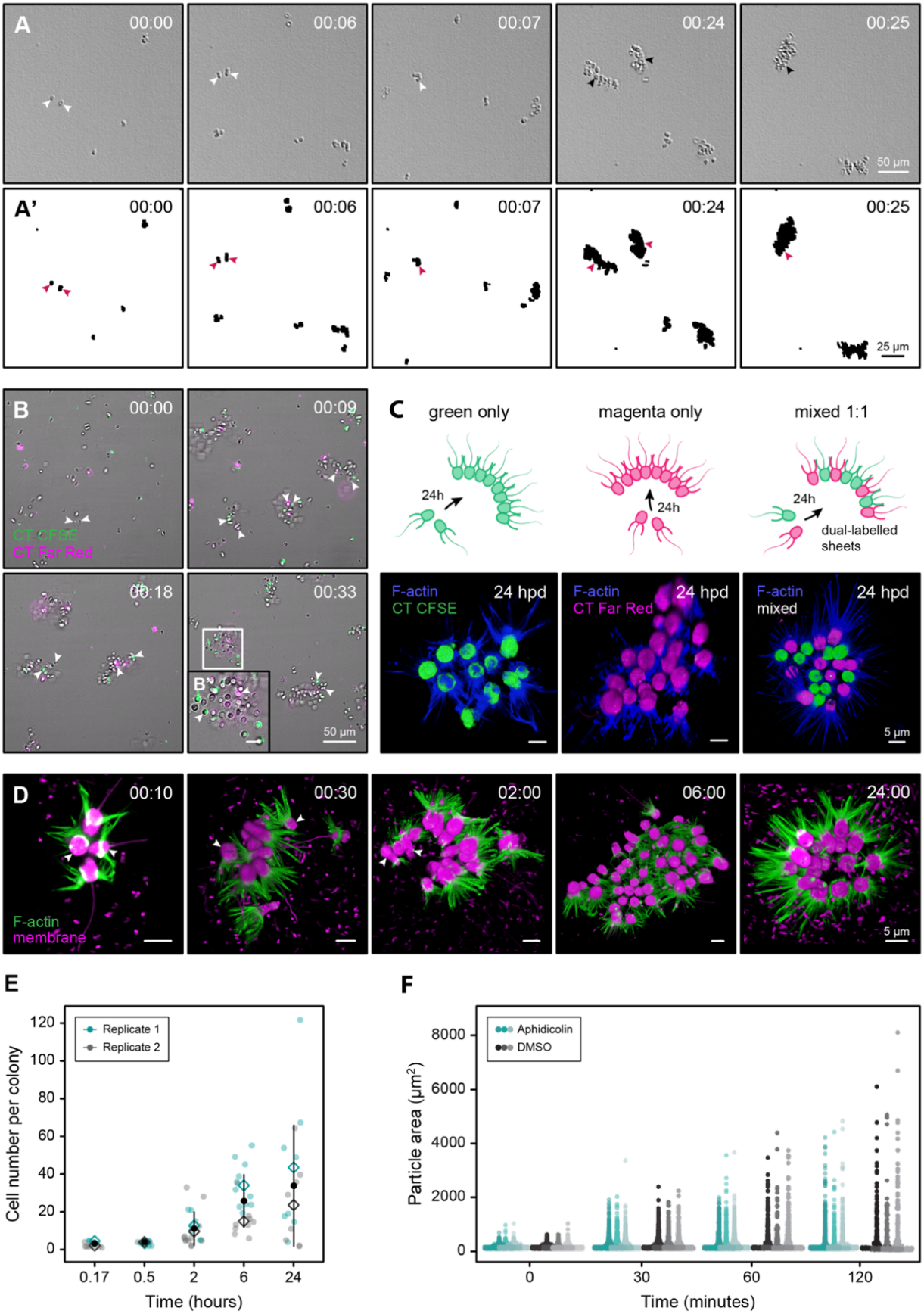
A
00:00
00:06
00:07
00:24
00:25
50 µm
A'
00:00
00:06
00:07
00:24
00:25
25 µm
B
00:00
00:09
CT CFSE
CT Far Red
00:18
00:33
B'
50 µm
C
green only
magenta only
mixed 1:1
24h
24h
24h
dual-labelled sheets
F-actin
CT CFSE
24 hpd
F-actin
CT Far Red
24 hpd
F-actin
mixed
24 hpd
5 µm
D
00:10
00:30
02:00
06:00
24:00
F-actin
membrane
5 µm
E
Replicate 1
Replicate 2
Cell number per colony
120
100
80
60
40
20
0
0.17
0.5
2
6
24
Time (hours)
F
Aphidicolin
DMSO
Particle area (µm²)
8000
6000
4000
2000
0
0
30
60
120
Time (minutes)

Figure 2.2. Multicellularity in *C. flexa* can be established purely by aggregation.
(**A**) Stills from a brightfield timelapse movie showing that dissociated single cells (white arrowheads) quickly re-formed colonies by cellular aggregation. Note that two colonies can fuse together by agglomeration (black arrowheads). (**A'**) Binary image mask of stills in A. Time scale hh:mm. (**B**) Stills from a timelapse movie showing that two dissociated single cell populations labelled with either Cell Trace CFSE (green) or Cell Trace Far Red (magenta) aggregated into dual-labelled chimeric groups of cells (white arrowheads). Time scale hh:mm. B', white square: zoom-in showing a dual-labelled colony. Scale bar: 10 µm. (**C**) (Upper panels) Dissociated single flagellate cells labelled with Cell Trace CFSE (left, green) or Cell Trace Far Red (middle, magenta) form single-labelled colonies 24 hours post-dissociation (hpd). When both single celled populations are mixed in a 1:1 ratio, they form dual-labelled colonies (right). (Lower panels) 3D reconstructions of Airyscan Z-stacks of sheets formed by aggregation from dissociated single cells labelled as depicted above and fixed 24 hpd, with additional filamentous actin (F-actin) staining (phalloidin Alexa 405, blue). (**D**) 3D reconstructions of Airyscan microscopy images of single cells fixed after 10 minutes (n=12), 30 minutes (n=12), 2 hours (n=19), 6 hours (n=20) and 24 hours (n=16) post-dissociation stained for membrane/cytoplasm (FM^{TM} 4-64FX, magenta) and F-actin (phalloidin Alexa 488, green). Note that cells frequently show unaligned apico-basal polarity and diverse cell orientations at early timepoints (white arrowheads). Time scale hh:mm. (**E**) Quantification of cell number per colony during aggregation (from the experiment in D) in two independent biological replicates. Black circles: mean. Error bars: standard deviation. Diamonds: mean values of independent biological replicates. (**F**) Quantification of particle area during an aggregation time course of dissociated single cells pre-treated with 17 µg/mL aphidicolin overnight in three independent biological replicates. DMSO: negative control. Figure related to Figures 2.S2-S3 and movies S4-S13.

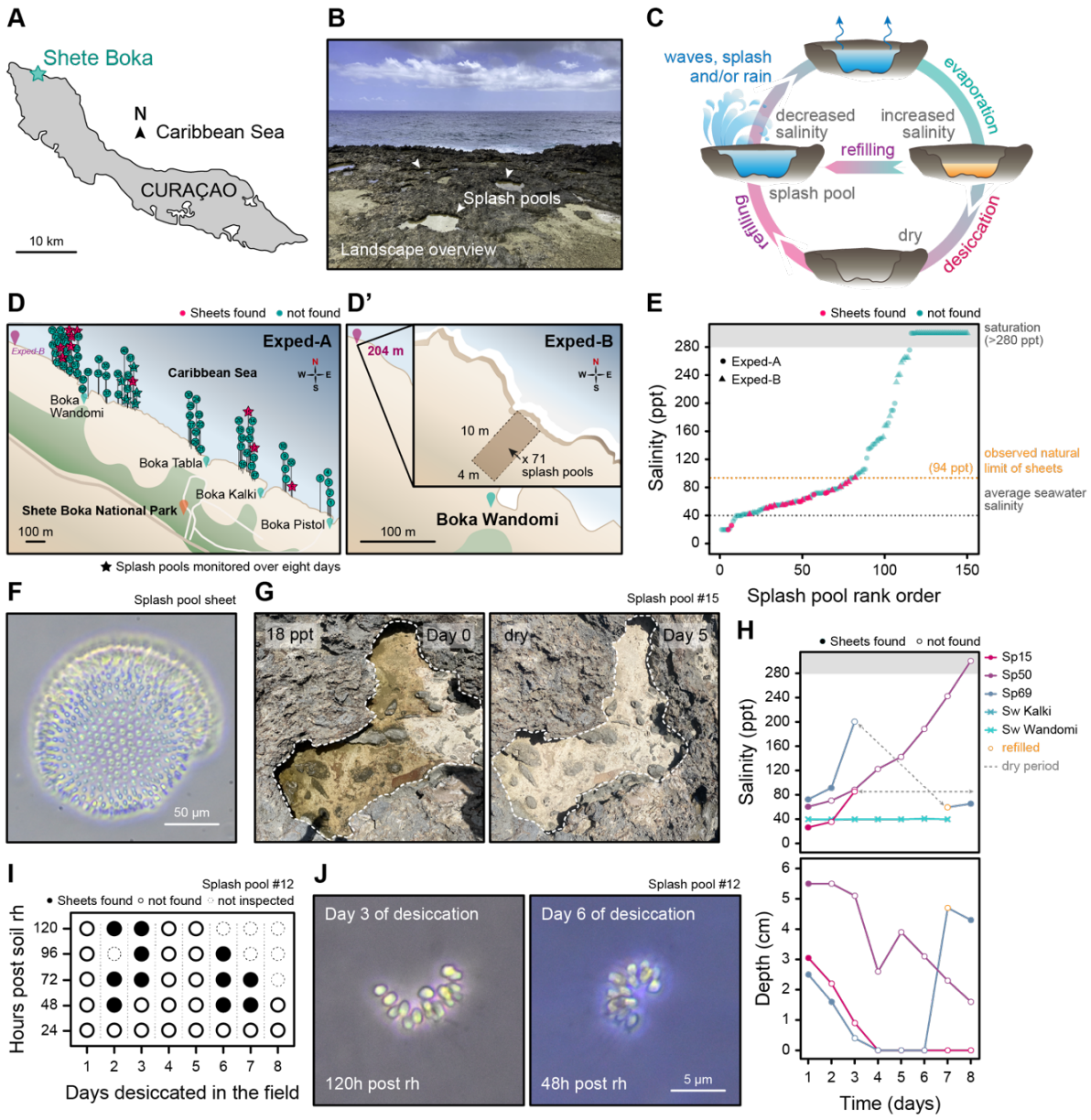

Figure 2.3. Cyclical salinity fluctuations constrain the occurrence of multicellular *C. flexa* sheets in their natural environment.

(**A**) Map of Curaçao and location of Shete Boka National Park (turquoise star) where fieldwork data was collected in Exped-A and Exped-B expeditions (12° 22' 5.718" N, 69° 06' 56.916" W). (**B**) Representative photograph of the landscape in Shete Boka, including splash pools where *C. flexa* sheets can be found (white arrowheads). (**C**) Schematics of a splash pool natural cycle of seawater evaporation, desiccation, and refilling. (**D**) Maps showing the locations of sampled splash pools in Exped-A and in Exped-B expeditions. In Exped-A (**D**), samples were collected from splash pools along ~2 km of Shete Boka coastline (n=79). 15 of these splash pools were randomly selected for daily monitoring during eight days (stars) (shown are results from the first day of monitoring). Colors indicate whether sheets were found (magenta) or not found (turquoise) upon microscopic inspection. In Exped-B (**D'**), a random number generator was used

to select the randomized sampling location (purple pin, 204 m upstream of Boka Wandomi). Samples were collected from splash pools within an area of 10 m by 4 m (n=71). (**E**) Distribution of salinity of splash pools surveyed in Exped-A (circles) and Exped-B (triangles). For daily monitored splash pools, measurements from the first day of monitoring are shown. Magenta and turquoise colors indicate that sheets were respectively found and not found in splash pool samples. The observed natural limit of salinity where sheets were found (94 ppt) is indicated by an orange dotted line, and the average seawater salinity measured in the *bokas* with a gray dotted line. Gray area: salinity saturation (>280 ppt). (**F**) Brightfield image of a sheet observed in a splash pool sample. (**G**) Representative images of a splash pool near Boka Kalki (Sp15) followed for eight days, showing recorded salinity in the upper left. This splash pool was completely desiccated at day 5 (right). Dashed line: splash pool outline. (**H**) Salinity (upper panel) and depth (lower panel) measurements in three representative splash pools followed over eigth days. Shown are one splash pool that experienced evaporation but not complete desiccation (Sp50), one splash pool that experienced complete desiccation (Sp15), and one splash pool that experienced both desiccation and refilling (Sp69). Filled and empty circles indicate that sheets were respectively found and not found in splash pool samples. Gray area: salinity saturation. Dashed lines: dry periods. Orange circles: refilling events. (**I**) Recovery of sheets from soil samples collected from a splash pool (Sp12) during its dry period. Soil samples were collected every day for eight days and were independently rehydrated in the laboratory with filtered seawater from the *bokas,* reconstituting salinity back to 42 ppt. Each rehydrated soil sample was monitored over five days for sheet re-appearance. Filled circle: sheets observed. Empty circle: sheets not observed. Dashed empty circle: sample not inspected. rh: rehydration. (**J**) Brightfield images of soil-recovered sheets (same experiment as in I) collected after 3 (left) and 6 (right) days of desiccation and rehydrated in the laboratory (lower left: time post-rehydration). Figure related to Figures 2.S4-S7, movies S14-S16, Tables S1-S2 and Supplementary Files S1-S4.

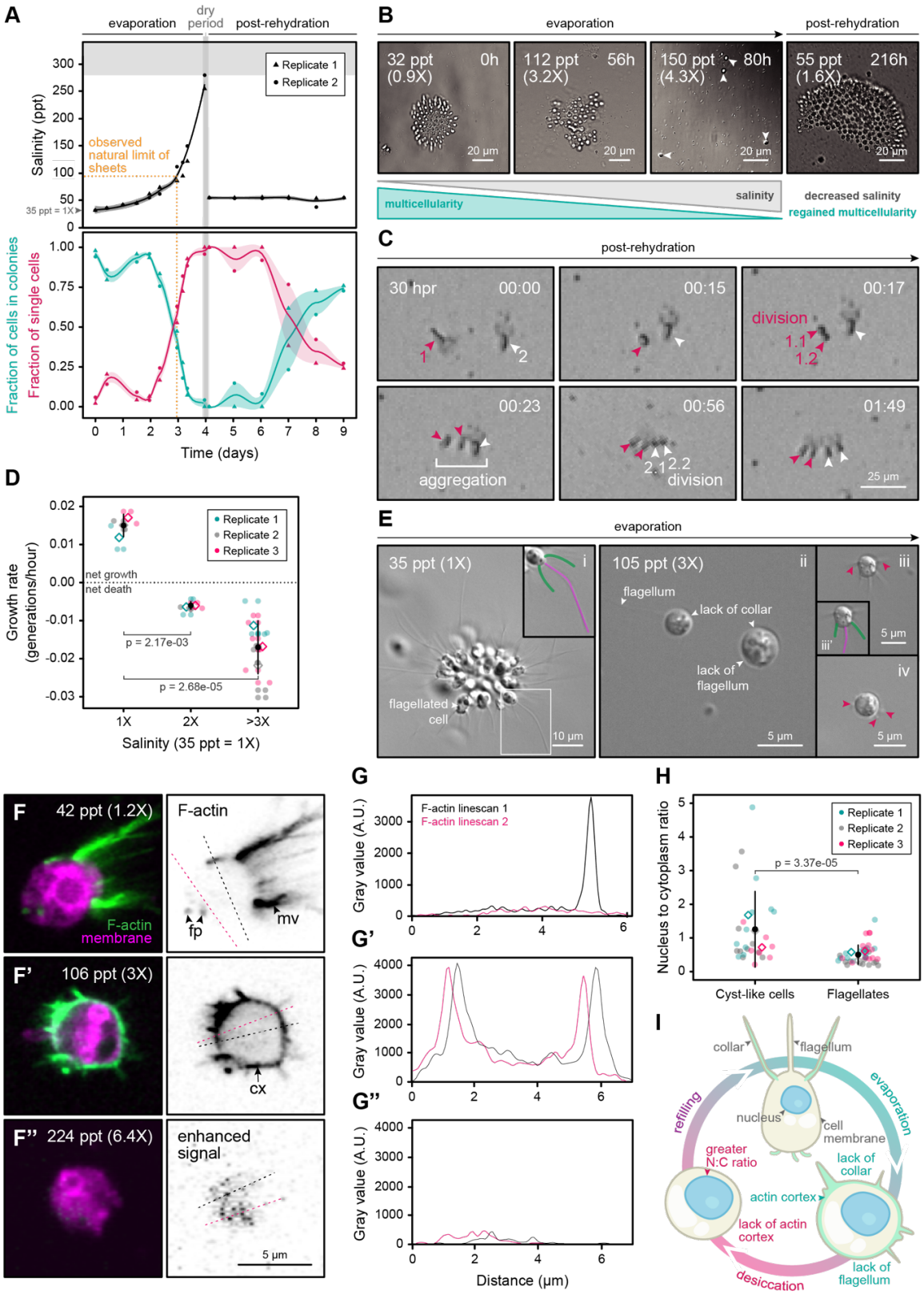
A
evaporation
dry period
post-rehydration
Replicate 1
Replicate 2
Salinity (ppt)
observed natural limit of sheets
35 ppt = 1X
Fraction of cells in colonies
Fraction of single cells
Time (days)
B
evaporation
post-rehydration
32 ppt (0.9X)
0h
112 ppt (3.2X)
56h
150 ppt (4.3X)
80h
55 ppt (1.6X)
216h
20 µm
multicellularity
salinity
decreased salinity
regained multicellularity
C
post-rehydration
30 hpr
00:00
00:15
00:17
division
1.1
1.2
1
2
00:23
00:56
01:49
aggregation
2.1 2.2
division
25 µm
D
Replicate 1
Replicate 2
Replicate 3
Growth rate (generations/hour)
net growth
net death
p = 2.17e-03
p = 2.68e-05
1X
2X
>3X
Salinity (35 ppt = 1X)
E
evaporation
35 ppt (1X)
i
flagellated cell
10 µm
105 ppt (3X)
ii
flagellum
lack of collar
lack of flagellum
5 µm
iii
iii'
iv
5 µm
5 µm
F
42 ppt (1.2X)
F-actin
membrane
F-actin
fp
mv
F'
106 ppt (3X)
cx
F''
224 ppt (6.4X)
enhanced signal
5 µm
G
F-actin linescan 1
F-actin linescan 2
Gray value (A.U.)
G'
G''
Distance (µm)
H
Replicate 1
Replicate 2
Replicate 3
Nucleus to cytoplasm ratio
p = 3.37e-05
Cyst-like cells
Flagellates
I
collar
flagellum
nucleus
cell membrane
evaporation
refilling
greater N:C ratio
lack of collar
actin cortex
lack of actin cortex
lack of flagellum
desiccation

Figure 2.4. Experimental evaporation-refilling cycles causes reversible transitions between multicellular sheets and unicellular cyst-like cells.
(**A**) Quantification of salinity (upper panel) and fraction of cells in colonies (magenta) or in single cells (turquoise) (lower panel) during a 9-day gradual evaporation time course. Dark gray rectangle: complete desiccation (dry period). Orange dotted line: observed natural salinity limit of sheet occurrence. Gray area: salinity saturation. Lines correspond to mean values and shadowed area to standard deviation. Experiment performed in two independent biological replicates. (**B**) Stills of *C. flexa* sheets during the same 9-day gradual evaporation timecourse in A, showing salinity (in ppt and fold-change compared to that of 1X ASW in parenthesis, upper left) and time (upper right). Sheets had completely dissociated into single cells (white arrowheads) after 80 hours of gradual evaporation. Multicellular sheets were observed again after complete desiccation and rehydration with 1X ASW. (**C**) Stills from a brightfield timelapse movie of cells rehydrated after complete desiccation. Recovered flagellate cells re-form colonies both by clonal division and aggregation 30 hours after rehydration. (**D**) Growth rate of cells at different salinities during gradual evaporation in three independent biological replicates. Black circles: mean. Error bars: standard deviation. n=28, *p* by the Mann-Whitney U test. Diamonds: mean values of independent biological replicates. (**E**) Brightfield images of *C. flexa* showing morphological changes during gradual evaporation. At ~1X seawater salinity (left), *C. flexa* occurs in the form of multicellular sheets of flagellated cells (**i**). Green pseudocolor: collar. Magenta pseudocolor: flagellum. During gradual evaporation (**ii-iv**, right panel), sheets dissociate into unicellular cyst-like cells. Cyst-like cells lack a collar, often lack a flagellum, and can exhibit filopodia-like protrusions (magenta arrowheads in iii-iv). (**F**) AiryScan micrographs of *C. flexa* cells fixed during gradual evaporation and stained with a membrane (FM^{TM} 4-64FX, magenta) and F-actin (phalloidin Alexa 488, green) dyes, showing lack of collar and flagellum in cyst-like cells. A flagellate cell (**F**, low-evaporation control) exhibits distribution of F-actin distribution in the collar of microvilli (mv, black arrowhead) and filopodia (fp, black arrowhead). Gradual evaporation triggers a morphological change from a flagellate to a cyst-like cell, showing a transient actin cortex (cx) at early stages of evaporation (**F'**, black arrow) which disappears as salinity approaches saturation (**F''**). (**G**) (resp. **G'**, **G"**) Line scan of F-actin fluorescence intensity along the dashed lines of interest in **F** (resp **F'**, **F"**), showing cortical actin as two peaks where the lines intersect the cell cortex. (**H**) Quantification of the nucleus-to-cytoplasm ratio in cyst-like cells (n=27) and flagellate cells (n=38) in three independent biological replicates. Black circles: means. Error bars: standard deviations. Diamonds: mean values of independent biological replicates. *p* by the Mann-Whitney U test. (**I**) Schematic summarizing phenotypic changes experienced by *C. flexa* cells during gradual evaporation. At early stages of evaporation (turquoise), flagellate cells differentiate into cyst-like cells by losing their collar and flagellum, and show a temporal actin cortex. At later stages of evaporation (desiccation, magenta), cyst-like cells lack an actin cortex and show a higher nucleus-to-cytoplasm ratio. Rehydration (refilling, purple) induces a cyst-like cell-to-flagellate cell transition, where cells regenerate their collar and flagellum and re-form multicellular sheets. Figure related to Figures 2.S8-S14 and movies S17-S18.

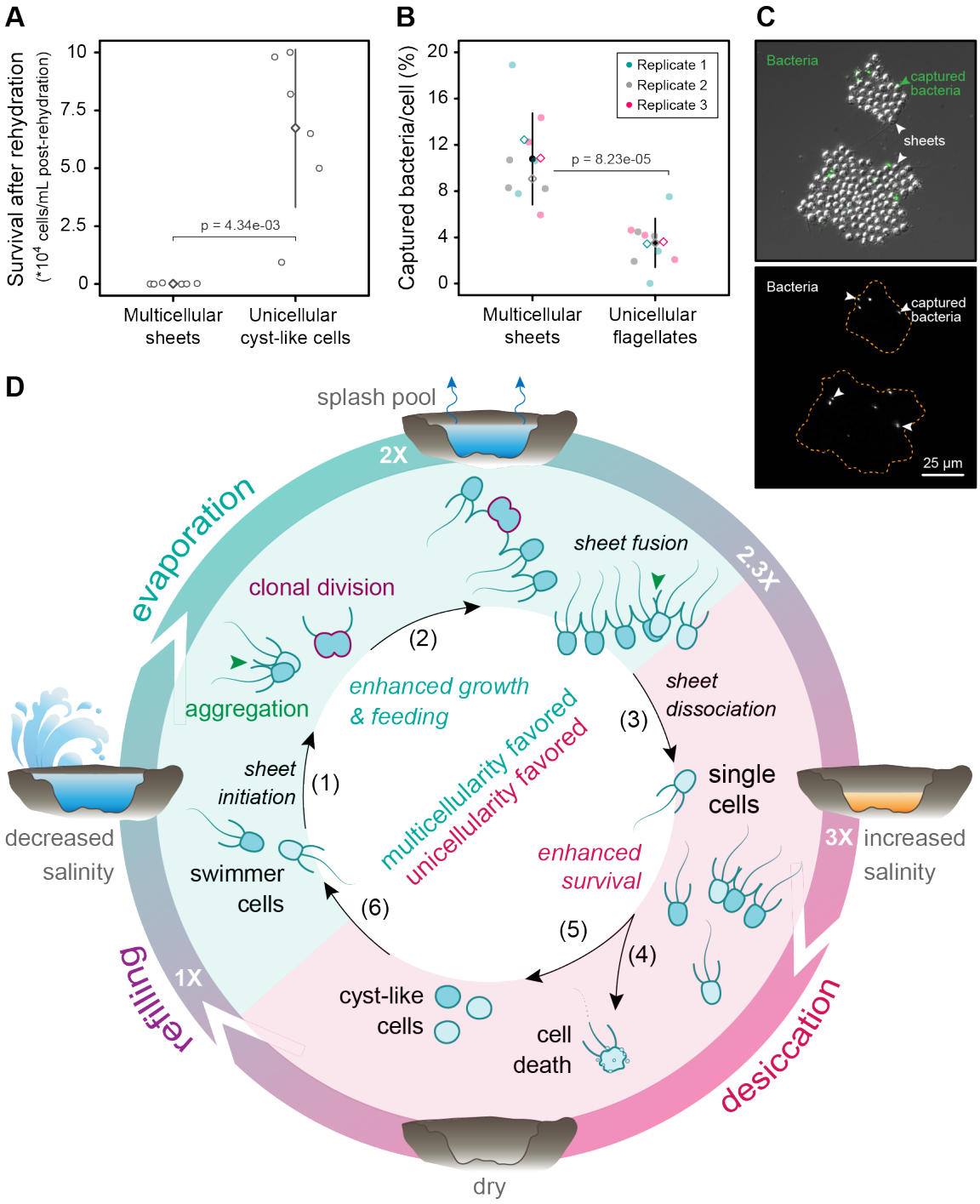

Figure 2.5. Unicellular cyst-like cells are advantaged at high salinity while multicellular sheets are advantaged at low salinity.

(**A**) Quantification of cell survival after 12 hours of desiccation in multicellular sheets (n=6 technical replicates) to unicellular cyst-like cells (n=6 technical replicates). Diamonds: means. Error bars: standard deviations. *p* by the Mann-Whitney U test. (**B**) *C. flexa* multicellular sheets are more efficient at capturing bacteria than unicellular flagellates. Number of labelled bacteria

captured per flagellate cells in multicellular colonies (n=9) or in cultures of unicellular flagellates (n=9) in three independent biological replicates. Black circles: means. Error bars: standard deviations. Diamonds: means of independent biological replicates. *p* by the Mann-Whitney U test. (**C**) DIC images of multicellular sheets (upper panel, white arrowheads) capturing fluorescently-labelled bacteria using Bactoview dye (upper panel: green; lower panel: white). (**D**) Summary schematic of *C. flexa* mixed clonal-aggregative development entrained by natural splash pool evaporation-refilling cycles. Multicellularity is favored in low salinity, where sheets exhibit enhanced growth and prey capture (turquoise): (1) unicellular flagellate cells can aggregate and/or divide clonally to initiate multicellular sheet development; (2) sheets expand by clonal cell division, by aggregation of individual cells, and by sheet fusion. Gradual evaporation leads to increase in salinity and favors unicellularity (magenta): (3) *C. flexa* remains multicellular in up to 2.3-fold salinity, but hypersaline conditions (>3-fold salinity) trigger sheet dissociation into single cells that are incapable of proliferation and occasionally to cell death (4). Gradual evaporation, instead, results in the differentiation of flagellates into cyst-like cells (5) capable of surviving desiccation. (6) Rehydration restores permissive salinity and induces differentiation of cyst-like cells into flagellates, which undergo clonal-aggregative multicellular development. Figure related to Figure 2.S15.

Supplementary Material

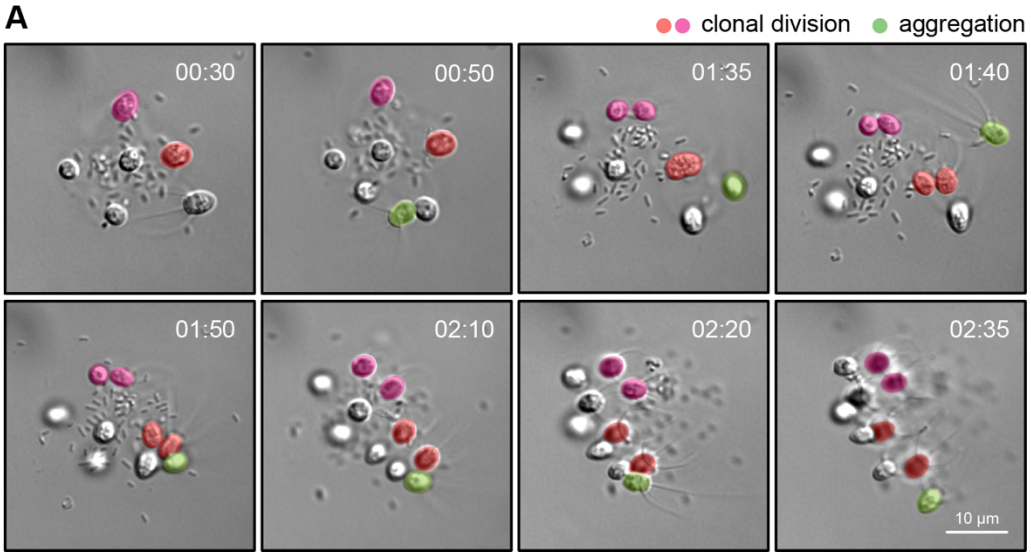

Figure 2.S1. *C. flexa* sheets exhibit mixed clonal-aggregative multicellularity.
(**A**) Snapshots of a brightfield timelapse movie of a small-sized *C. flexa* colony expanding in cell number. Two cells within the sheet divide clonally (orange and pink pseudocolor), and a swimmer flagellate cell joins the colony by cellular aggregation (green pseudocolor). Figure related to Figure 2.1G and Movie S3.

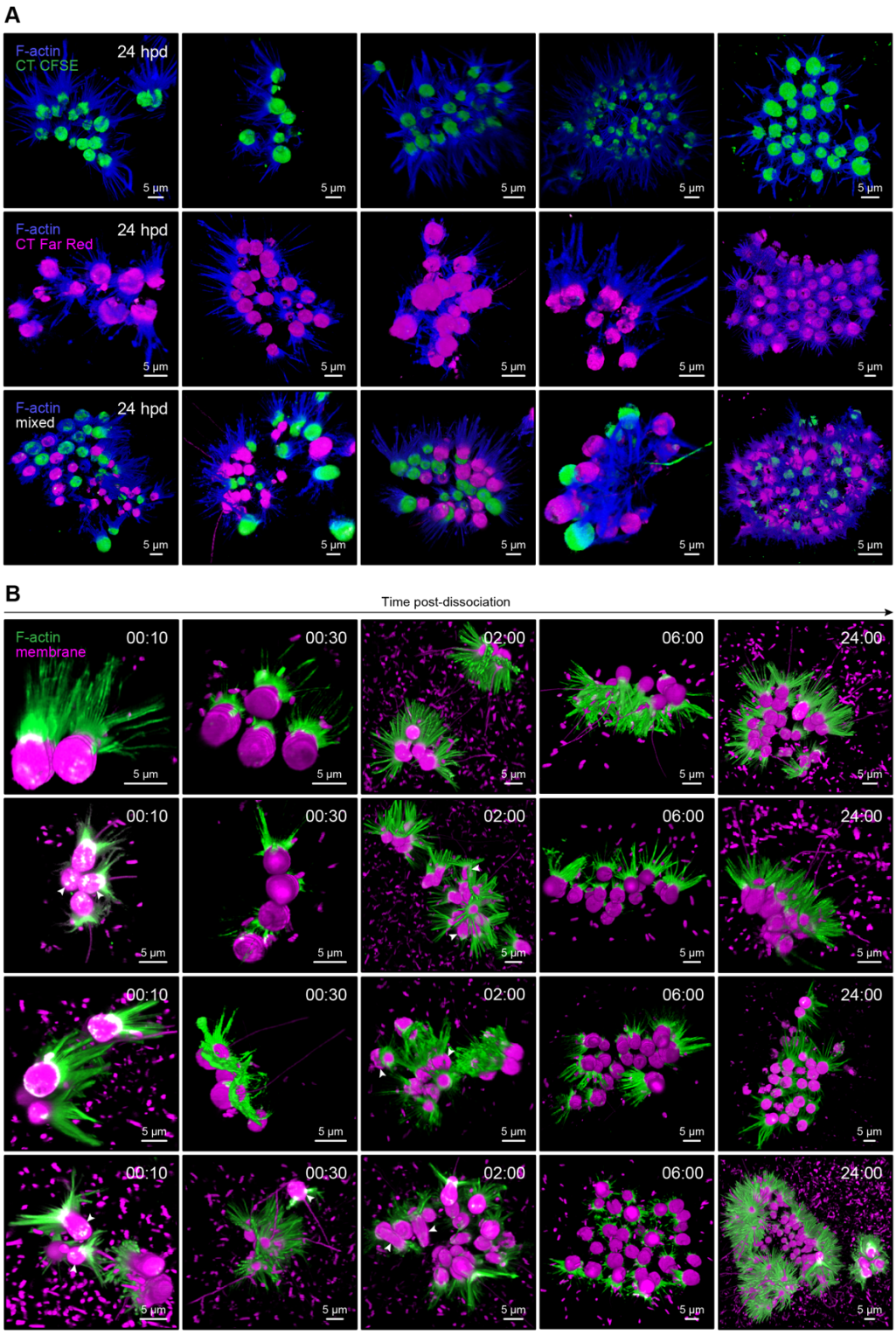

Figure 2.S2. *C. flexa* sheets can be formed purely by cellular aggregation.
(**A**) 3D reconstructions of Airyscan microscopy images of sheets formed from dissociated single cell populations labelled with Cell Trace CFSE (green) or Cell Trace Far Red (magenta) and fixed

24 hours post-dissociation, with additional filamentous actin (F-actin) staining labelling the microvilli (phalloidin 405, blue). When both single cell populations are mixed in a 1:1 ratio they form dual-labelled chimeric colonies. Shown are 5 different representative colonies for each condition. (**B**) 3D reconstructions of Airyscan microscopy images of dissociated cells fixed 10 minutes, 30 minutes, 2 hours, 6 hours, and 24 hours post-dissociation (hpd), with a membrane staining labelling the cell body and flagella (FM^{TM} 4-64FX, magenta) and F-actin staining labelling the collar (phalloidin 488, green). Shown are 4 different representative colonies for each timepoint. Note that cells frequently show unaligned apico-basal polarity and diverse cell orientations in early aggregation timepoints (white arrowheads). Time scale hh:mm. Figure related to Figure 2.2B-D and movies 2.S6-S8.

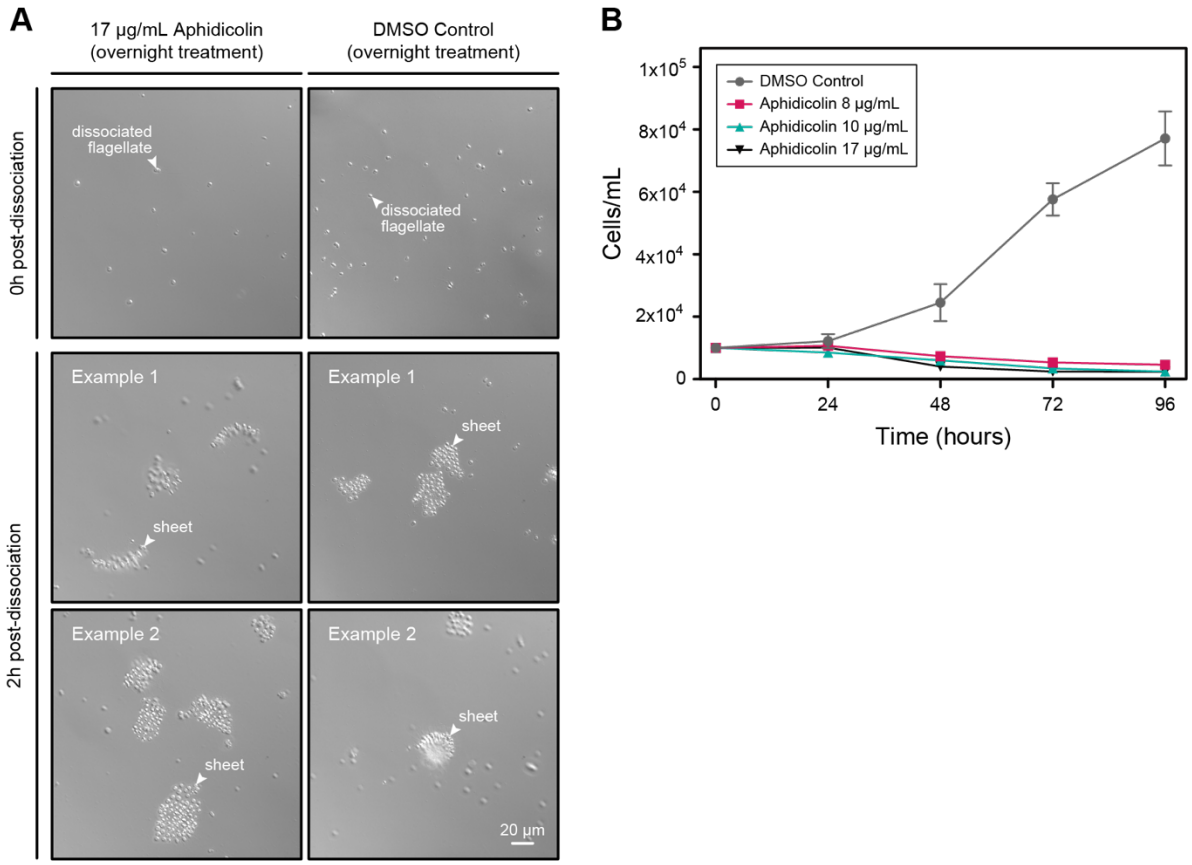

Figure 2.S3. Colony formation is independent of cell division.
(**A**) Snapshots of cells after 0 hours (flagellate cells, white arrowheads) and 2 hours post-dissociation (sheets, white arrowheads). Cells were initially treated overnight with 17 µg/mL Aphidicolin cell cycle inhibitor prior dissociation. (**B**) Dose-response growth curve of dissociated single cells treated with distinct concentrations of Aphidicolin shows that it effectively blocks cell division at concentrations equal or greater than 8 µg/mL. DMSO was used as a negative control. Figure related to Figure 2.2F.

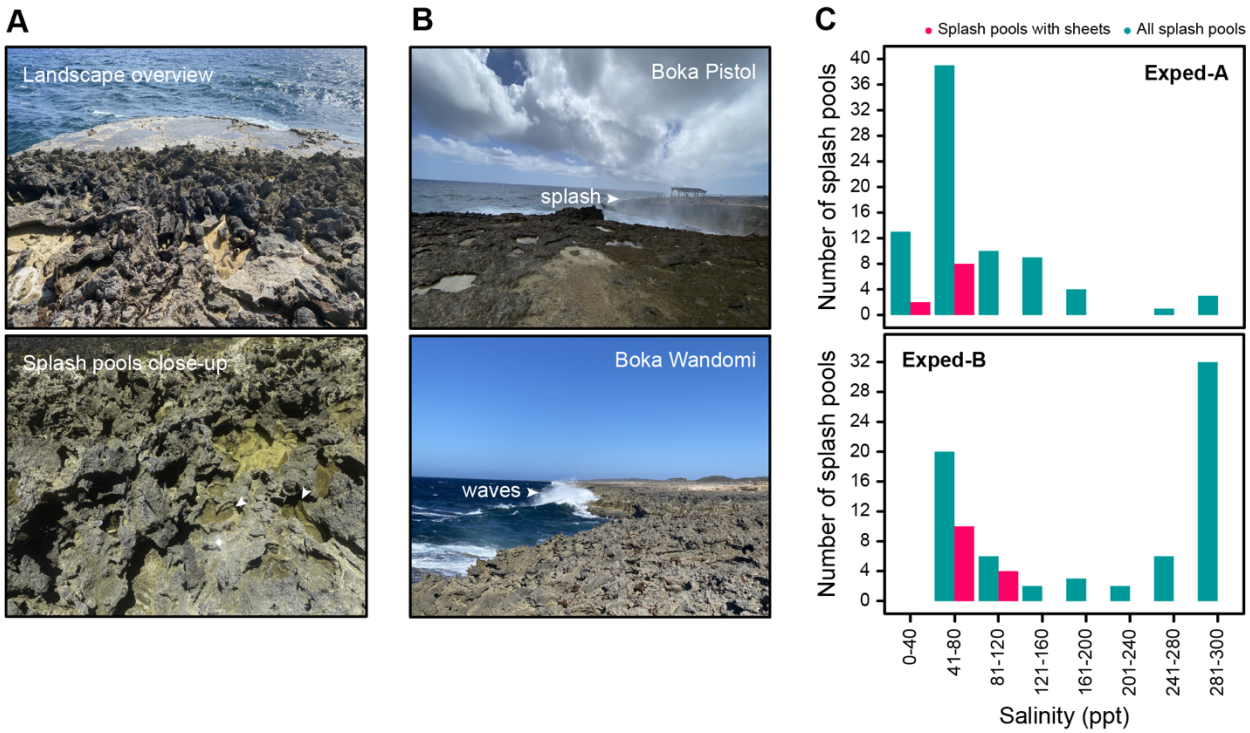

Figure 2.S4. Salinity distribution and presence of sheets comparing Exped-A and Exped-B Curaçao expeditions.

(**A**) Representative images of the landscape in Shete Boka National Park, with a close-up image of splash pools (white arrowheads). (**B**) Representative images of splash pools near Boka Pistol and Boka Wandomi, including two possible sources of splash pool refilling by splash or waves from the sea (white arrowheads). (**C**) Distribution of seawater salinity of sampled splash pools on Exped-A and Exped-B Curaçao expeditions. Magenta and turquoise colors indicate that sheets were respectively found and not found in splash pool samples. Figure related to Figure 2.3 and Table S1.

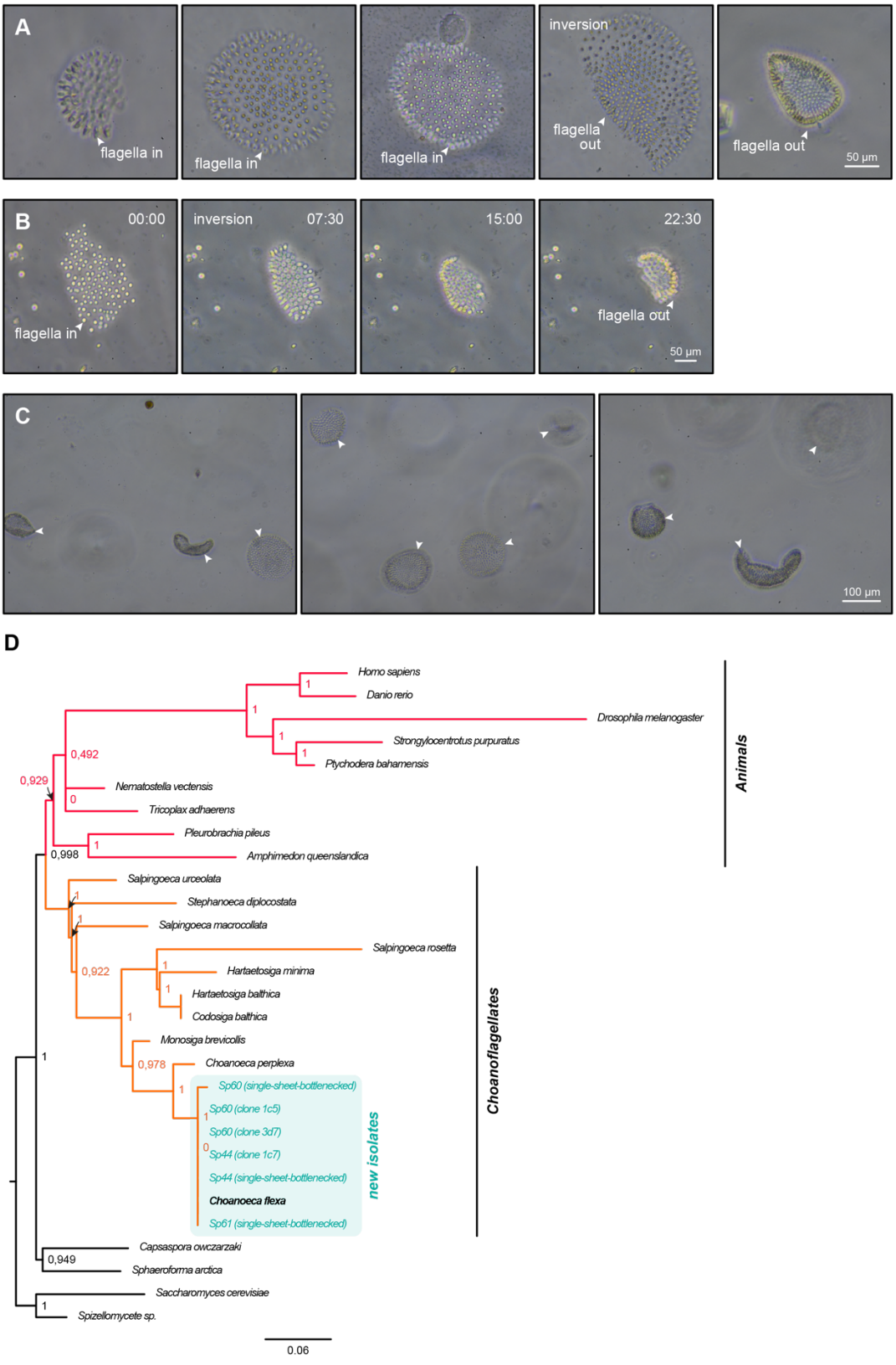
A
flagella in
flagella in
flagella in
inversion
flagella out
flagella out
50 µm
B
00:00
flagella in
inversion
07:30
15:00
22:30
flagella out
50 µm
C
100 µm
D
Homo sapiens
Danio rerio
Drosophila melanogaster
Strongylocentrotus purpuratus
Ptychodera bahamensis
Animals
0,492
0,929
Nematostella vectensis
Tricoplax adhaerens
Pleurobrachia pileus
Amphimedon queenslandica
0,998
Salpingoeca urceolata
Stephanoeca diplocostata
Salpingoeca macrocollata
Salpingoeca rosetta
0,922
Hartaetosiga minima
Hartaetosiga balthica
Codosiga balthica
Monosiga brevicollis
0,978
Choanoeca perplexa
Sp60 (single-sheet-bottlenecked)
Sp60 (clone 1c5)
Sp60 (clone 3d7)
Sp44 (clone 1c7)
Sp44 (single-sheet-bottlenecked)
Choanoeca flexa
Sp61 (single-sheet-bottlenecked)
new isolates
Choanoflagellates
Capsaspora owczarzaki
0,949
Sphaeroforma arctica
Saccharomyces cerevisiae
Spizellomycete sp.
0.06

Figure 2.S5. Sheets identified in natural splash pool samples correspond to *C. flexa* species, and exhibit the stereotypical cup-shaped morphology and light-induced inversion behavior. (**A**) Representative brightfield images of sheets observed in natural splash pool samples. Note the different "flagella in" and "flagella out" sheet conformations. (**B**) Snapshots of a brightfield timelapse movie of a medium-sized sheet inverting its curvature from a "flagella in" to a "flagella out" conformation in response to light-to-dark transitions. (**C**) Representative brightfield images of multiple sheets in the same field of view identified in natural splash pool samples. (**D**) 18S rDNA phylogenetic tree of newly isolated *C. flexa* single-sheet-bottlenecked and clonal cultures (turquoise), several other choanoflagellates (orange), and other opisthokonts, including animals (red), other holozoans and fungal species. Shown is a Maximum Likelihood phylogenetic tree of 18S rDNA sequences of three single-sheet-bottlenecked cultures isolated from Sp44, Sp60 and Sp61 (Exped-B) and three clonal cultures isolated from Sp44 and Sp60 (Exped-B). Support values on nodes: approximate likelihood ratio test (aLRT).

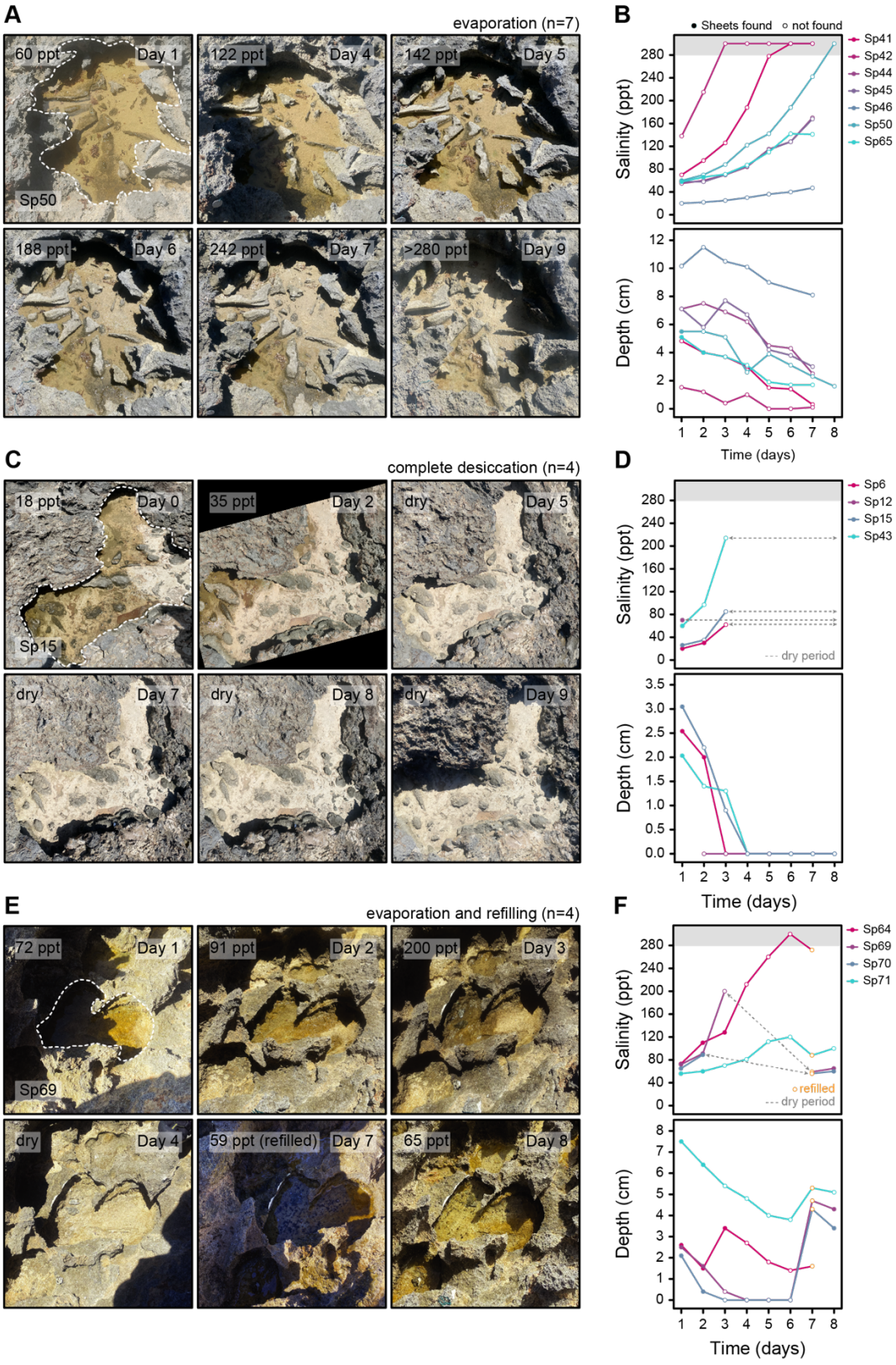
A
evaporation (n=7)
60 ppt
Day 1
Sp50
122 ppt
Day 4
142 ppt
Day 5
188 ppt
Day 6
242 ppt
Day 7
>280 ppt
Day 9
B
Sheets found
not found
Sp41
Sp42
Sp44
Sp45
Sp46
Sp50
Sp65
Salinity (ppt)
Depth (cm)
Time (days)
C
complete desiccation (n=4)
18 ppt
Day 0
Sp15
35 ppt
Day 2
dry
Day 5
dry
Day 7
dry
Day 8
dry
Day 9
D
Sp6
Sp12
Sp15
Sp43
dry period
Salinity (ppt)
Depth (cm)
Time (days)
E
evaporation and refilling (n=4)
72 ppt
Day 1
Sp69
91 ppt
Day 2
200 ppt
Day 3
dry
Day 4
59 ppt (refilled)
Day 7
65 ppt
Day 8
F
Sp64
Sp69
Sp70
Sp71
refilled
dry period
Salinity (ppt)
Depth (cm)
Time (days)

Figure 2.S6. Splash pools undergo natural cycles of evaporation and refilling.
(**A**, **C**, **E**) Representative images of followed-up splash pools near Boka Kalki (Sp15) and Boka Wandomi (Sp50 and Sp69) during a 9-day timecourse from Exped-A Curaçao expedition. Some splash pools experienced evaporation (**A**), complete desiccation (**C**), and evaporation and refilling (**E**). Dashed lines indicate area of each splash pool. Salinity (in ppt) measurements are depicted in the upper left, and time (in days) of each timepoint in the upper right. Total number of splash pools analyzed in each condition are indicated outside the image panels in the upper right. (**B**, **D**, **F**) Salinity (upper panels) and depth (lower panels) measurements over time. Presence or absence of sheets is indicated by filled or empty circles, respectively. Gray area depicts salinity saturation outside the refractometer measuring range. Dry periods of splash pools that were completely evaporated are indicated with dashed lines in D and F. Refilling events are depicted with an orange circle in F. Figure related to Figure 2.3, Figures 2.S4-S5 and Table S1.

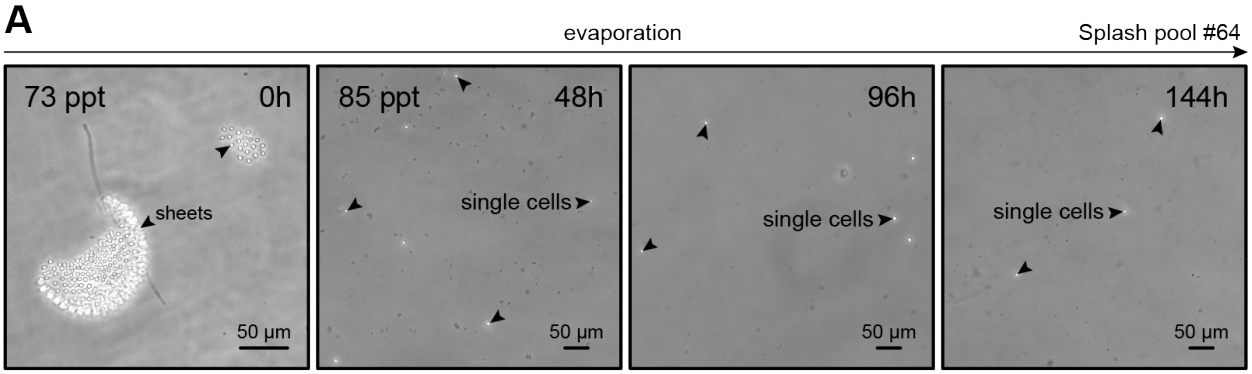

Figure 2.S7. Gradual evaporation triggers loss of multicellularity of sheets in natural splash pool samples.

(**A**) Representative brightfield images of sheets identified in natural samples from Sp64 (Exped-A) over a 6-day gradual evaporation time course in the laboratory. After 48 hours, sheets dissociated and single cells (black arrowheads) appeared. Time under gradual evaporation is depicted in the upper right. Salinity was not measure at 96 and 144 hours. Figure related to Figure 2.3 and Figure 2.4.

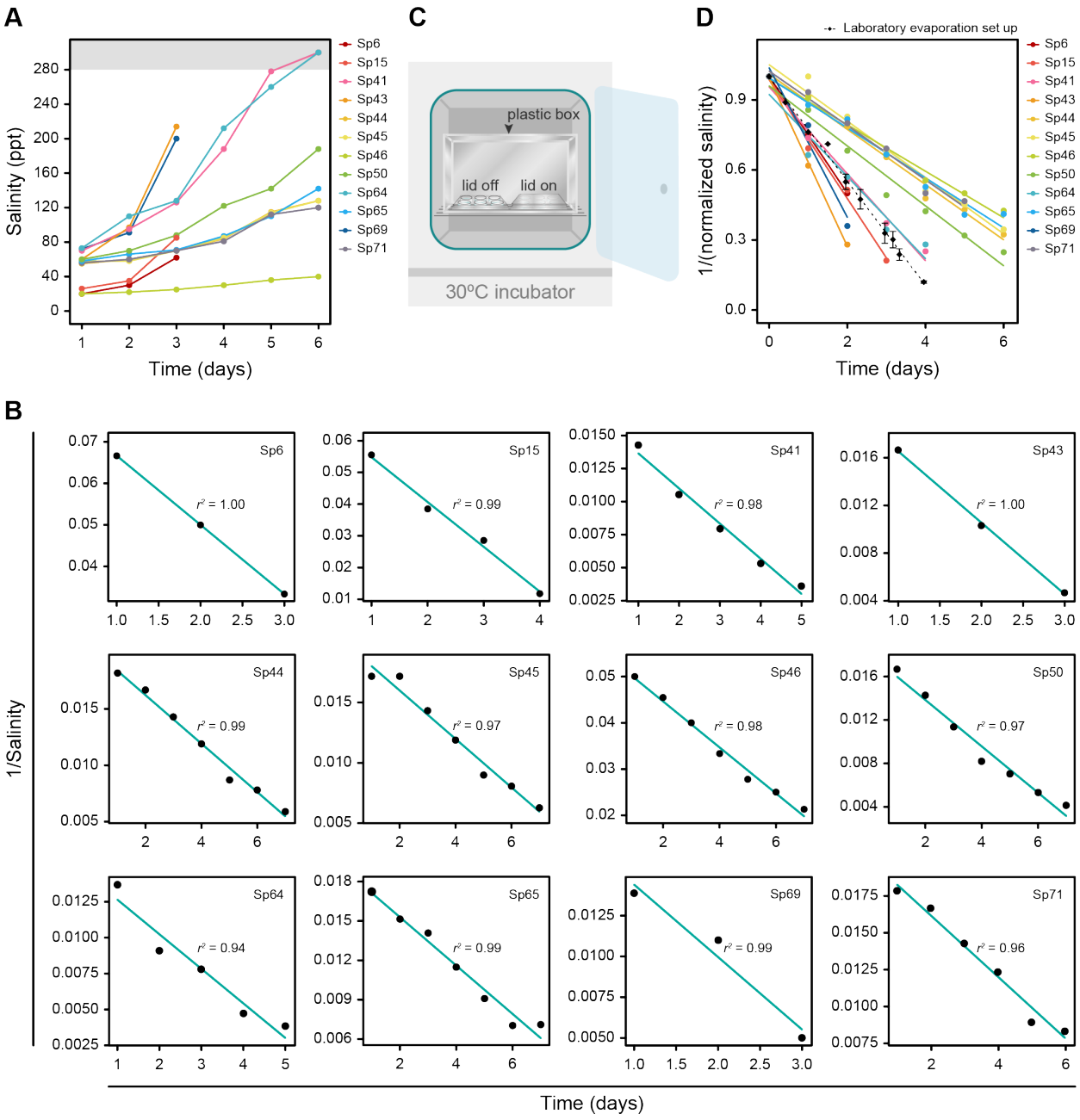

Figure 2.S8. Modelling splash pool gradual evaporation enables design of a laboratory experimental setup with similar evaporation dynamics.

(**A**) Salinity monitoring of followed-up splash pools during a 8-day time course from Exped-A Curaçao expedition. Splash pools during the first 6 days of the time course gradually evaporated, and hence they were used to model splash pool evaporation dynamics. Splash pools with less than 3 points outside saturation range (gray area) were not included in the modelling (*i.e.* Sp12, Sp42, and Sp70; see Figure 2.S6). (**B**) Inverse of salinity over time of splash pools in A. (**C**) Laboratory experimental evaporation setup in a 30ºC incubator. Note that plates were kept with the plate's lid off (gradual evaporation condition) or the plate lid's on (low-

evaporation control) over a grid and were covered with a plastic box to avoid contamination and favor air exchange. (**D**) Normalized inverse of salinity over time during gradual evaporation comparing empirical data from splash pools in B versus the laboratory experimental setup (black) in C. Figure related to Figure 2.3 and Table S1.

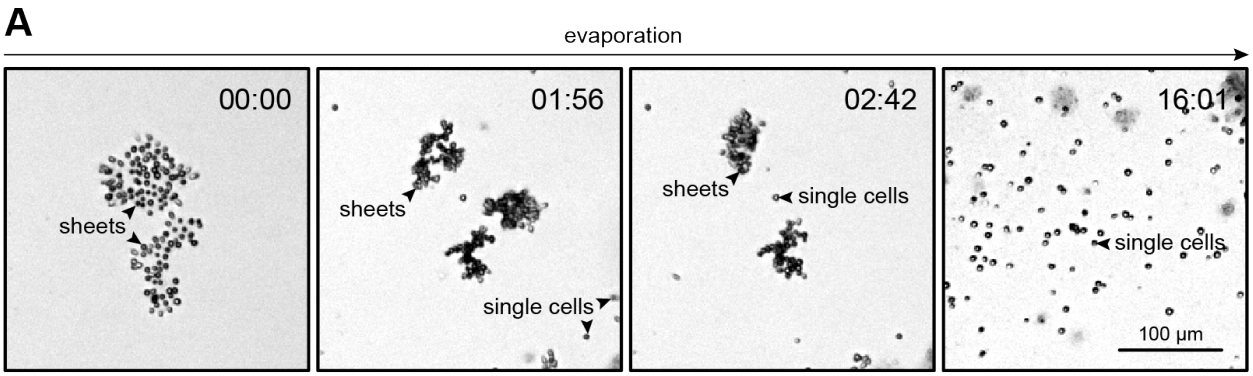

Figure 2.S9. Gradual evaporation triggers *C. flexa* sheet dissociation into single cells.
(**A**) Snapshots of a brightfield timelapse movie of *C. flexa* colonies in 1X ASW salinity experiencing gradual evaporation shows sheet dissociation into single cells (black arrowheads). Figure related to Figure 2.4 and Movie S17.

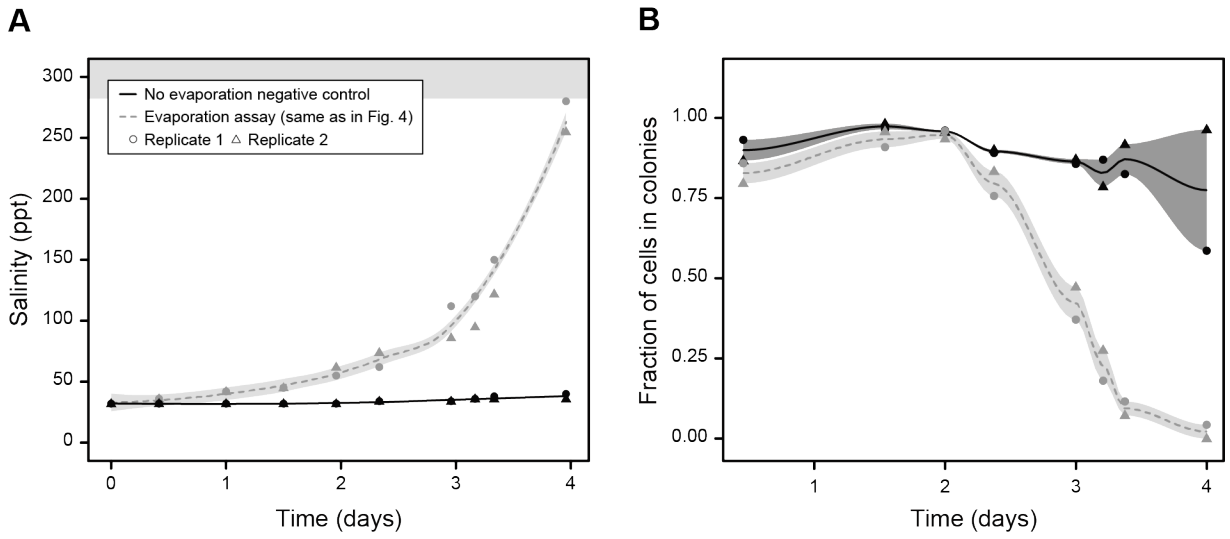

Figure 2.S10. Gradual evaporation causes loss of multicellularity in laboratory conditions. (**A**) Quantification of salinity during a 4-day timecourse comparing the gradual evaporation laboratory experimental set up and a no evaporation negative control laboratory set up. Values are represented as mean (lines) ± s.d (shadowed area). Gray area depicts salinity saturation outside the refractometer measuring range. All experiments were performed in two independent biological replicates. (**B**) Quantification of fraction of cells in colonies in A. Figure related to Figure 2.4.

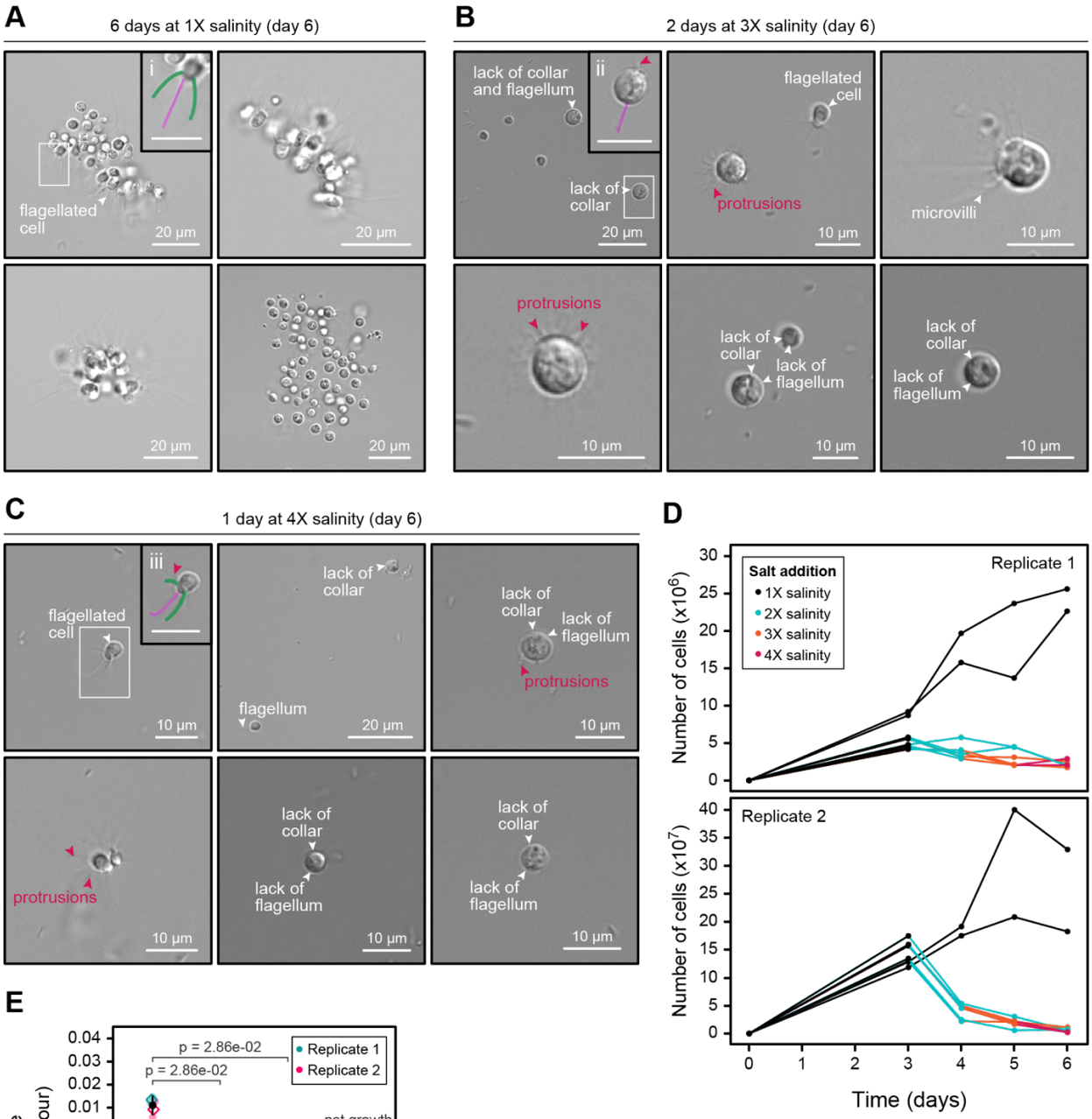
A
6 days at 1X salinity (day 6)
i
flagellated cell
20 µm
B
2 days at 3X salinity (day 6)
ii
lack of collar and flagellum
lack of collar
flagellated cell
protrusions
microvilli
10 µm
20 µm
C
1 day at 4X salinity (day 6)
iii
flagellated cell
lack of collar
flagellum
lack of flagellum
protrusions
D
Salt addition
1X salinity
2X salinity
3X salinity
4X salinity
Replicate 1
Replicate 2
Number of cells (x10^6)
Number of cells (x10^7)
Time (days)
E
p = 2.86e-02
Replicate 1
Replicate 2
net growth
net death
Growth rate (generations/hour)
Salinity (35 ppt = 1X)
1X
2X
3X
4X

Figure 2.S11. Salinity increase by the addition of salts (without evaporation) induces loss of multicellularity, phenotypic changes of single cells and cell growth arrest as in gradual evaporation conditions.

(**A-C**) DIC images of *C. flexa* cells over a 6-day timecourse experiment where salinity was progressively increased 1-fold daily by the addition of salts after 3 days of growth show that cells undergo morphological changes in hypersaline media. At the end of the 6-day timecourse, cells grown for 6 days at 1X salinity (**A**, no salinity increase) remain as multicellular sheets composed of flagellate cells (**i**) that showcase a collar (green pseudocolor) and a flagellum (magenta pseudocolor). Upon progressive salinity increase by the addition of salts, sheets dissociate into unicellular cyst-like cells (**B-C**). Many cyst-like cells lack a collar and a flagellum, and exhibit filopodia-like protrusions (magenta arrowheads) after 2 days at 3X salinity (**B**) and after 1 day at 4X salinity (**C**). Scale bars in (**i-iii**) correspond to 10 µm. (**D**) Quantification of cell number over a 6-day timecourse where salinity was progressively increased 1-fold daily by the addition of salts after 3 days of growth. 1X salinity corresponds to 35 ppt. (**E**) Growth rate of cells over a 6-day timecourse experiment in D. Error bars are represented as mean (black circles) ± s.d. (n=16, *p* by the Mann-Whitney U test). Mean values of each biological replicate are represented as diamonds. Experiments in D-E were performed in two independent biological replicates, including two technical replicates per condition. Figure related to Figure 2.4D-E.

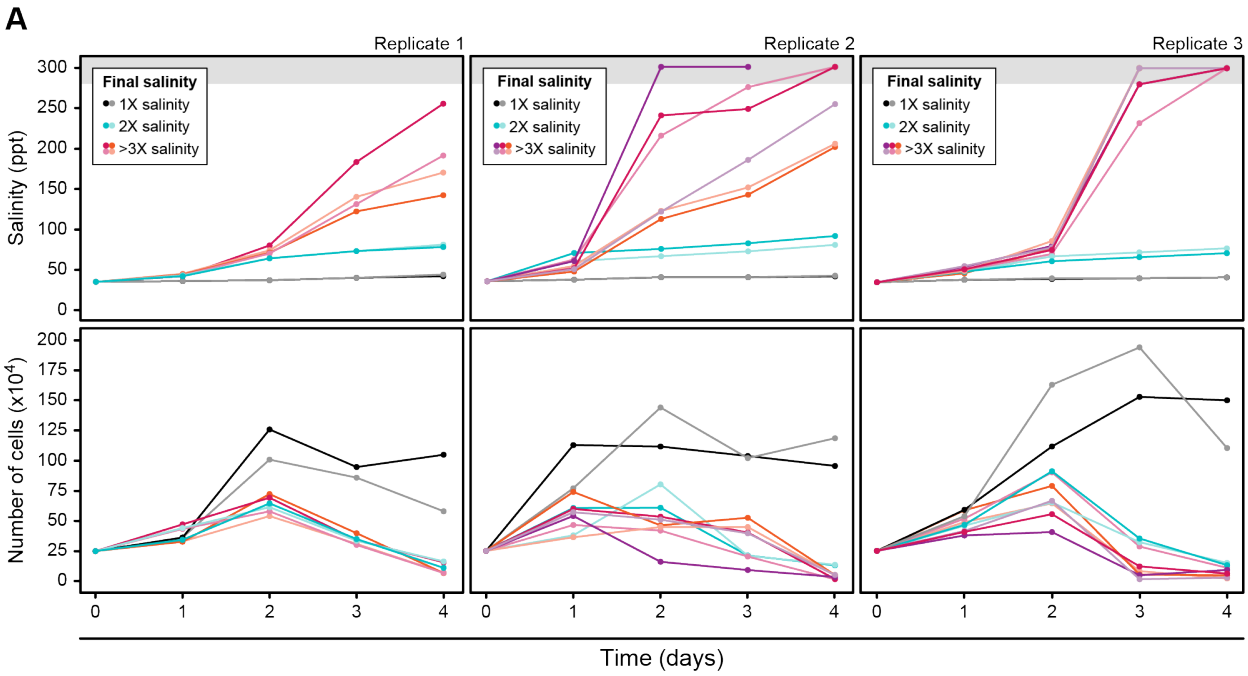

Figure 2.S12. Salinity increase during gradual evaporation arrests cell growth.
(**A**) Quantification of salinity (upper panels) and cell number (lower panels) over a 5-day timecourse experiment in the gradual evaporation experimental set up. Gray area depicts salinity saturation outside the refractometer measuring range. 1X salinity corresponds to 35 ppt. All experiments were performed in three independent biological replicates. Figure related to Figure 2.4D.

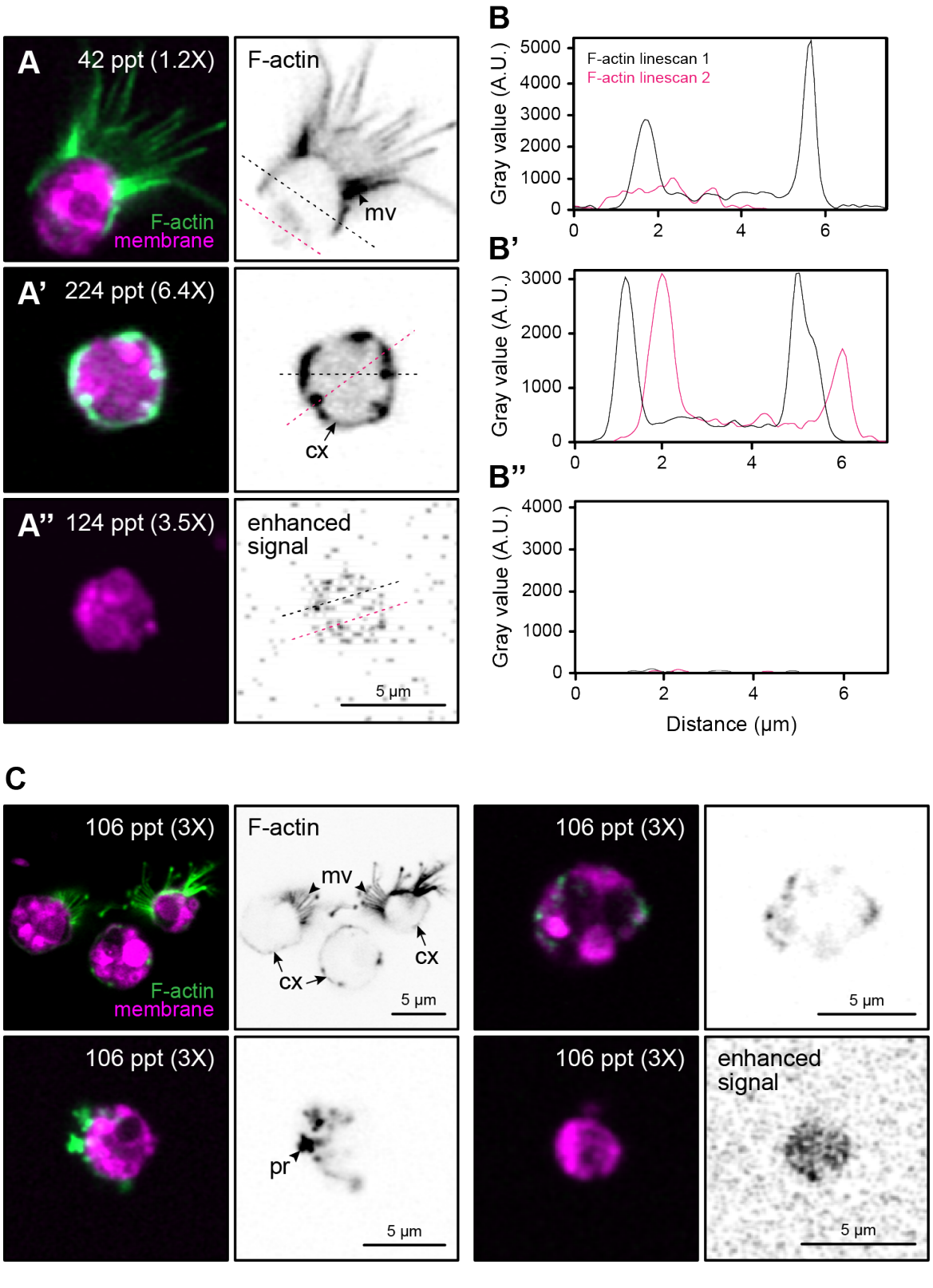
A
42 ppt (1.2X)
F-actin
membrane
F-actin
mv
A'
224 ppt (6.4X)
cx
A''
124 ppt (3.5X)
enhanced
signal
5 µm
B
F-actin linescan 1
F-actin linescan 2
Gray value (A.U.)
5000
4000
3000
2000
1000
0
0
2
4
6
B'
3000
2000
1000
B''
Distance (µm)
C
106 ppt (3X)
F-actin
membrane
mv
cx
pr

Figure 2.S13. Flagellate cells transition to cyst-like cells during gradual evaporation, showing a temporal actin cortex formation that disappears at later stages close to desiccation.
(**A**) Mid z-sections of Airyscan microscopy images of *C. flexa* cells during gradual evaporation fixed and stained with a membrane (FM^{TM} 4-64FX, magenta) and F-actin (phalloidin 488, green) dyes confirmed that cyst-like cells lack a collar and a flagellum at later stages of evaporation. A flagellate cell (**i**, low-evaporation control) exhibits the stereotypical filamentous actin distribution in the collar microvilli (mv, black arrowhead). Gradual evaporation triggers a morphological change from a flagellate to a cyst-like cell, showing a temporal actin cortex (cx, black arrow) formation at early stages of evaporation (**ii**, black arrowheads) and a later actin-free signal in salinity close to saturation (**iii**). (**B**) Linescan of F-actin fluorescence intensity along the dashed lines of interest in A, showing cortical actin as two peaks where the lines intersect the cell cortex. (**C**) Mid z-sections of Airyscan microscopy images of *C. flexa* during gradual evaporation fixed at 106 ppt salinity and stained as in A shows heterogeneity of F-actin signal either distributed in the microvilli (mv, black arrowheads), actin cortex (cx, black arrow) and filopodia-like protrusions (pr, black arrowheads) or absent in cyst-like cells. Figure related to Figure 2.4F-G.

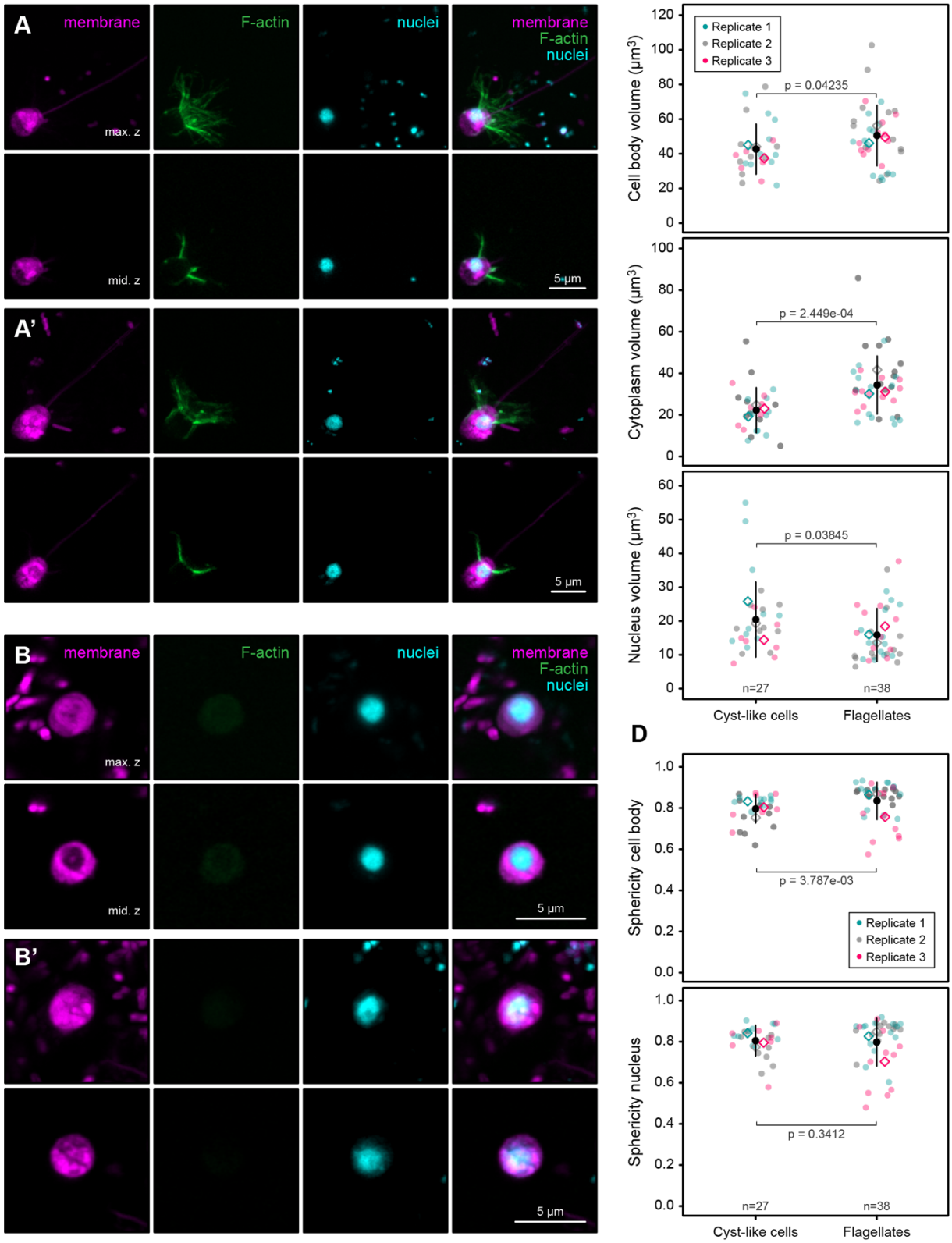
A
membrane
F-actin
nuclei
membrane
F-actin
nuclei
max. z
mid. z
5 µm
A'
5 µm
B
membrane
F-actin
nuclei
membrane
F-actin
nuclei
max. z
mid. z
5 µm
B'
5 µm
C
Replicate 1
Replicate 2
Replicate 3
Cell body volume (µm3)
p = 0.04235
Cytoplasm volume (µm3)
p = 2.449e-04
Nucleus volume (µm3)
p = 0.03845
n=27
n=38
Cyst-like cells
Flagellates
D
Sphericity cell body
p = 3.787e-03
Replicate 1
Replicate 2
Replicate 3
Sphericity nucleus
p = 0.3412
n=27
n=38
Cyst-like cells
Flagellates

Figure 2.S14. Cyst-like cells have greater nucleus-to-cytoplasm ratio than flagellate cells. (**A**) Maximum z-projections (upper panels) and mid z-sections (lower panels) of Airyscan microscopy images showing two representative flagellate cells (**A-A'**) (low-evaporation control) and two representative cyst-like cells (**B-B'**) stained with membrane (FM^{TM} 4-64FX, magenta), F-actin (phalloidin 488, green) and nucleus (Hoechst, cyan) dyes. (**C**) Quantification of cell body, cytoplasm and nucleus volume of individual cyst-like cells (n=27) and flagellate cells (n=38) in A-B in three independent biological replicates. (**D**) Quantification of sphericity (values fange from 0 (nonspherical) and 1 (perfect sphere)) of individual cyst-like cells (n=27) and flagellate cells (n=38) in A-B in three independent biological replicates. Error bars in C-D are represented as mean (black circles) ± s.d. (*p* by the Mann-Whitney U test). Mean values of each independent replicate are represented as diamonds. Figure related to Figure 2.4H.

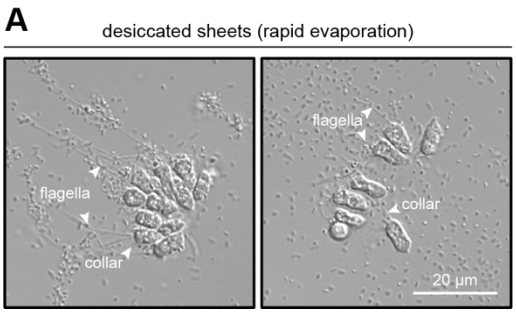

Figure 2.S15. Multicellular sheets do not survive after rapid evaporation.
(**A**) DIC images of desiccated sheets after rapid evaporation show that they still preserve the signature features of choanoflagellate cells: a flagellum and a collar (white arrowheads). Figure related to Figure 2.5A.

Supplementary Tables S1-S2, Files S1-S4 and Movies S1-S18 can be found online at https://www.biorxiv.org/content/10.1101/2024.03.25.586565v1

Table S1. Fieldwork data collection.

Table S2. Primers used for 18S rDNA amplification and sequencing.

Supplementary Files S1-S4. 18S rDNA sequencing data, multiple sequences alignment and phylogenetic tree comparing newly isolated single-sheet-bottlenecked and clonal (single-cell-bottlenecked) cultures isolated from the field.

Movie S1. *C. flexa* multicellular colonies can develop clonally from a single cell. Brightfield timelapse movie of a single *C. flexa* flagellate (swimmer) cell dividing asynchronously every ~8-10 hours. After each division, the sister cells remain adhered to each other by direct cell-cell contacts in the collar, giving rise to a monolayered colony with the signature curved morphology of *C. flexa* sheets. Movie related to Figure 2.1D-E.

Movie S2. *C. flexa* multicellular colonies can expand in cell number both by clonal cell division and cellular aggregation. Brightfield timelapse movie of a medium-sized *C. flexa* colony. Note that four cells within the colony divide clonally, and a duplet of cells joins the colony by cellular aggregation. Sister cells resulting from cell division and the duplet of cells that aggregates to the colony adhere to each other by direct cell-cell contacts. Time represents hh:mm. Movie related to Figure 2.1F.

Movie S3. *C. flexa* multicellular colonies can expand in cell number both by clonal cell division and cellular aggregation. Brightfield timelapse movie of a small-sized *C. flexa* colony, showing a mixed mode of clonal and aggregative multicellularity. Time represents hh:mm. Movie related to Figure 2.1F and Figure 2.S1.

Movie S4. Dissociated single cells reform sheets by cellular aggregation. Brightfield timelapse movie of mechanically dissociated single cells that actively aggregate within minutes into irregular masses of cells, that can eventually fuse by agglomeration. Time represents hh:mm. Movie related to Figure 2.2A.

Movie S5. Mixing two populations of single cells stained with two different fluorophores results in the formation of chimeric, dual-labelled sheets. Timelapse movie mixing two dissociated single cell populations labelled with either Cell Trace CFSE (green) or Cell Trace Far Red (magenta) form dual-labelled chimeric colonies by cellular aggregation. Time scale hh:mm. Movie related to Figure 2.2B-C.

Movies S6-S8. Two different labelled populations produce chimeric colonies by aggregation. 3D reconstruction movies from Airyscan microscopy images of fixed colonies 24 hours post-dissociation. Two single cell populations were stained with either Cell Trace CFSE (green) or Cell Trace Far Red (magenta) and later fixed and additionally stained with a filamentous actin marker

(phalloidin 405, blue). Each labelled single-celled population form green (Movie S6) or magenta (Movie S7) single-colored control colonies. When both labelled single-celled populations are mixed in a 1:1 ratio they form chimeric, dual-labelled colonies (Movie S8). Movies related to Figure 2.2B-C and Figure 2.S2A.

Movies S9-S13. Multicellularity in *C. flexa* can be established uniquely by aggregation. 3D reconstruction movies from Airyscan microscopy images of fixed colonies 10 minutes (Movie S6), 30 minutes (Movie S7), 2 hours (Movie S8), 6 hours (Movie S9), and 24 hours (Movie S10) post-dissociation. Cells were stained with a membrane (FM^{TM} 4-64FX, magenta) and filamentous actin (phalloidin 488, green) markers. Movies related to Figure 2.2D-E and Figure 2.S2B.

Movie S14. Splash pools can get refilled by splash from the sea. Movie of several splash pools near Boka Wandomi being refilled by splash from the sea.

Movie S15. *C. flexa* sheets can be observed in natural splash pool samples. Brightfield timelapse movie of a *C. flexa* sheet observed in a splash pool sample responding to light-to-dark transitions.

Movie S16. Collection of soil samples from desiccated splash pools for rehydration experiments. Movie showing the collection procedures of a soil sample from a dry splash pool, that was later rehydrated in the laboratory. Movie related to Figure 2.3I-J and Figure 2.S7.

Movie S17. *C. flexa* loses multicellularity and dissociates into single cells upon gradual evaporation. Binary mask of a brightfield timelapse movie of a multicellular culture of *C. flexa* starting at 1X salinity and later undergoing gradual evaporation. Movie related to Figure 2.4A-B and Figure 2.S10.

Movies S18. *C. flexa* regains multicellularity both by clonal division and aggregation after rehydration. Brightfield timelapse movie of cells 30.17 hours post-rehydration. Movie related to Figure 2.4A-B and Figure 2.S10.

Chapter 3

Nitric oxide signaling controls collective contractions in a colonial choanoflagellate

The results presented here were published as part of the following paper:

Reyes-Rivera, J. et al. Nitric Oxide Signaling Controls Collective Contractions in a Colonial Choanoflagellate. *Current Biology.* (2022) doi:10.1016/j.cub.2022.04.017

Table S1 and Video S1 are available in the published online version.

Summary

Although signaling by the gaseous molecule nitric oxide (NO) regulates key physiological processes in animals, including contractility (Ellwanger and Nickel 2006; Elliott and Leys 2010; Musser et al. 2021), immunity (Bogdan 2015; Hillyer and Estevez-Lao 2010), development (Tomankova, Abaffy, and Sindelka 2017; Ueda et al. 2016; Gibbs et al. 2001; Estephane and Anctil 2010) and locomotion (Pirtle and Satterlie 2021; Moroz et al. 2004), the early evolution of animal NO signaling remains unclear. To reconstruct the role of NO in the animal stem lineage, we set out to study NO signaling in choanoflagellates, the closest living relatives of animals (Carr et al. 2008). In animals, NO produced by the nitric oxide synthase (NOS) canonically signals through cGMP by activating soluble guanylate cyclases (sGCs) (Denninger and Marletta 1999; Andreakis et al. 2011). We surveyed the distribution of the NO signaling pathway components across the diversity of choanoflagellates and found three species that express NOS (of either bacterial or eukaryotic origin), sGCs, and downstream genes previously shown to be involved in the NO/cGMP pathway. One of the species co-expressing sGCs and a bacterial-type NOS, *Choanoeca flexa*, forms multicellular sheets that undergo collective contractions controlled by cGMP(Brunet et al. 2019). We found that treatment with NO induces cGMP synthesis and contraction in *C. flexa*. Biochemical assays show that NO directly binds *C. flexa* sGC1 and stimulates its cyclase activity. The NO/cGMP pathway acts independently from other inducers of *C. flexa* contraction, including mechanical stimuli and heat, but sGC activity is required for contractions induced by light-to-dark transitions. The output of NO signaling in *C. flexa* – contractions resulting in a switch from feeding to swimming – resembles the effect of NO in sponges (Elliott and Leys 2010; Musser et al. 2021; Ellwanger and Nickel 2006) and cnidarians (Colasanti et al. 1997; Moroz et al. 2004; Anctil, Poulain, and Pelletier 2005), where it interrupts feeding and activates contractility. These data provide insights into the biology of the first animals and the evolution of NO signaling.

Results

C. flexa encodes both NOS and sGC

C. flexa is a colonial choanoflagellate that forms concave sheets capable of global inversion of their curvature through collective contractility (Brunet et al. 2019). *C. flexa* inversion mediates a trade-off between feeding and swimming: relaxed colonies (with their flagella pointing inside) are slow swimmers and efficient feeders, while contracted colonies (with their flagella pointing outside) are inefficient feeders but fast swimmers (Brunet et al. 2019) (Figure 3.1A). Inversion has been shown to be induced by light-to-dark transitions through inactivation of a rhodopsin-phosphodiesterase (Rho-PDE) and accumulation of cGMP (Brunet et al. 2019) (Figure 3.1B). The involvement of cGMP in collective contraction in *C. flexa* and the connection between NO/cGMP signaling and tissue contraction in non-bilaterian animals (Colasanti, Persichini, and Venturini 2010) led us to investigate whether NO signaling might exist and regulate sheet inversion in *C. flexa* (Figure 3.1B).

By examining the genomes of two choanoflagellates (*Monosiga brevicollis* (Robertson 2009) and *Salpingoeca rosetta* (Fairclough et al. 2013)) and the transcriptomes of *C. flexa* (Brunet et al. 2019) and 19 other choanoflagellates(Richter et al. 2018), we found that five choanoflagellate species encode NOS homologs and that nine choanoflagellate species encode sGC homologs (Figure 3.2A). Of these, three species – *Salpingoeca infusionum, Choanoeca perplexa,* and *C. flexa* – express both NOS and sGCs, suggesting that some aspect of the physiology of these organisms might be regulated by NO/cGMP signaling.

Like metazoan NOS genes, choanoflagellate NOS genes encode the canonical oxygenase and reductase domains (Figure 3.2B). Phylogenetic analysis revealed that one choanoflagellate NOS gene, that from *S. infusionum,* is closely related to those from metazoans and fungi (Figure 3.S1A). In contrast, all other choanoflagellate NOSs (including those from *C. flexa*) cluster with cyanobacterial NOSs, suggesting they might have been acquired through horizontal gene transfer from a cyanobacterial ancestor early in the evolution of choanoflagellates (Figure 3.S1A). Current uncertainties surrounding the choanoflagellate phylogeny (Carr et al. 2008; Carr et al. 2017) make it difficult to pinpoint exactly when this horizontal gene transfer event occurred, and whether it followed or preceded the loss of the ancestral eukaryotic NOS in most or all choanoflagellates. These choanoflagellate NOS genes, like those of cyanobacteria, differ from metazoan NOS in that they encode an upstream globin domain with unknown function and lack the calmodulin-binding domain that mediates regulation of metazoan NOSs by Ca^{2+}, suggesting that calcium signaling does not regulate NO synthesis in *C. flexa*. The *C. flexa* transcriptome also encodes complete biosynthetic pathways for the NOS cofactors BH_4, FMN, FAD and NADPH (Figure 3.S2A) as well as downstream genes in the NO/cGMP signaling pathway: cGMP-dependent kinase (PKG), cGMP-gated ion channels (CNG) and cGMP-dependent phosphodiesterase (PDEG) (Figure 3.S2B), providing additional evidence that *C. flexa* employs NO signaling as part of its physiology.

Nearly all sGC genes from choanoflagellates, including *C. flexa,* encode the canonical domains observed in animal sGCs: the heme NO/O_2-binding domain (HNOB or H-NOX), the HNOB associated domain (HNOBA) and the C-terminal catalytic domain (guanylate cyclase) (Derbyshire and Marletta 2009) (Figure 3.2C). Phylogenetic analysis revealed that all animal and most choanoflagellate sGCs (including those of *C. flexa*) evolved from a single ancestral sGC found in the last common ancestor of choanoflagellates and metazoans which diversified separately into multiple paralogs in these two lineages (Figure 3.S1B). In contrast, the predicted sGC from one choanoflagellate species, *S. helianthica*, more closely resembles the sGCs of chlorophyte algae (which are the only protist group previously known to encode sGC proteins with a metazoan-like domain architecture (Horst, Stewart, et al. 2019); Figure 3.S1B).

Importantly, not all animal sGCs are regulated by nitric oxide: in *Drosophila melanogaster* and *Caenorhabditis elegans*, so-called "atypical sGCs" preferentially bind soluble O_2 instead of NO and are thought to be involved in the regulation of feeding by oxygen concentration (Gray et al. 2004; Huang, Rio, and Marletta 2007; Cheung et al. 2004). Discrimination between NO and O_2 is mediated by the presence of a hydrogen-bonding network, where a distal pocket tyrosine residue is critical for stabilizing the heme-O_2 complex (Boon and Marletta 2005). We generated preferential binding predictions based on this motif (Boon, Huang, and Marletta 2005; Boon and Marletta 2005) and found that both NO and O_2-preferential binding sGCs are widely distributed among choanoflagellates with no obvious pattern (Figure 3.2A; Figure 3.S2D). Interestingly, predicted NO-selective sGCs are present in choanoflagellate species in which NOS was not detected, suggesting that these species might detect NO from an exogenous source (i.e. environmental bacteria or other protists), might possess an alternative NO-producing mechanism, or might encode an NOS that was not detected in the transcriptome. In *C. flexa*, one out of four sGC transcripts was predicted to be selective for NO and was named *Cf* sGC1 (Figure 3.S2D). The other two choanoflagellate species found to possess both an NOS and sGCs, *C. perplexa* and *S. infusionum,* were also predicted to encode at least one NO-sensitive sGC (Figure 3.2A).

NO/cGMP signaling controls colony contraction in *C. flexa*

To test whether NO signaling regulates collective contractions in *C. flexa*, we treated *C. flexa* cultures with several NO donors (Cheng et al. 2019), compounds capable of releasing NO in solution. We found that treatment of *C. flexa* with the NO donors proliNONOate and DEANONOate led to an increase in intracellular NO as detected by the NO-sensitive fluorescent probe DAF-FM, demonstrating that they could be effective reagents for studying NO signaling in *C. flexa in vivo* (Figure 3.3A, 3.S3A-C). Treatment of *C. flexa* with proliNONOate (Figure 3.3B,C) induced colony contraction within one to two minutes (although the inversion process itself only lasted a few seconds, as previously described for darkness-induced inversion(Brunet et al. 2019); see Video S1). The inversion response of *C. flexa* to proliNONOate was concentration-dependent (Figure 3.3D), reaching a plateau of nearly 100% inversion at a concentration of 0.1 µM. As a negative control, *C. flexa* did not invert in response to proline, the molecular backbone of proliNONOate and the end product of NO release (Figure 3.3D). Moreover, treatment with

two other NO donors, DEANONOate or NOC-12, also induced inversion (Figure 3.S3D). Taken together, these results indicate that NO is sufficient to induce colony contraction.

We next investigated whether NO triggers cGMP synthesis in *C. flexa*. We found that a pan-inhibitor of sGCs, ODQ (Zhao et al. 2000), had no detectable effect on the percentage of contracted colonies 5 minutes after treatment with NO relative to cultures not treated with ODQ. However, a difference between the two conditions became evident 10 minutes after NO treatment, with nearly all ODQ-treated colonies relaxing into the uncontracted form, while all ODQ-untreated colonies remained contracted at least twice as long (Figure 3.3E). This premature relaxation of ODQ-treated colonies was concentration-dependent (Figure 3.3F).

These results suggest that the maintenance of NO-induced colony contraction requires sGC activity. However, the pan-sGC inhibitor ODQ does not allow us to discriminate between NO or O_2-sensitive sGCs. If NO does indeed signal through the sGC/cGMP pathway, we predicted that treatment of colonies with an NO donor should increase intracellular cGMP concentration. We found that NO-treated cells contained consistently higher intracellular cGMP levels than untreated cells (~2-fold increase on average, p=0.0237; Figure 3.3G). Importantly, prior work has demonstrated that treatment of *C. flexa* with a cell-permeant form of cGMP (8-Br-cGMP) is sufficient to induce inversion(Brunet et al. 2019). These results further support the hypothesis that NO activates sGCs and stimulates the production of cGMP, which might contribute to maintaining *C. flexa* colony contraction.

C. flexa sGC1 is an NO-selective and catalytically active component of the *C. flexa* NO/cGMP signaling pathway

Of the four sGCs expressed by *C. flexa*, only one (*Cf* sGC1) was predicted to be selective for NO (Figure 3.S2D). To directly test the existence of a canonical NO/sGC/cGMP pathway in *C. flexa*, we characterized ligand binding and activity of *Cf* sGC1 that had been heterologously expressed in and purified from *E. coli* (Figure 3.3H). The ligand specificity of sGCs can be determined by comparing the "Soret peak" maxima of the ultraviolet/visible (UV/vis) absorption after incubation with different gases, including NO, O_2 or CO. The Fe(II), unliganded form of *Cf* sGC1 exhibited a Soret peak at 429 nm and a single broad plateau in the α/β region (500-600 nm), consistent with that of an NO-selective sGC (Boon, Huang, and Marletta 2005) (Figure 3I; Table S1). In the presence of NO, the Soret peak shifted to 399 nm with two peaks in the α/β region, as characteristic for a 5-coordinate, high-spin NO-heme complex (Boon, Huang, and Marletta 2005) (Figure 3.3I; Table S1). On the other hand, when exposed to atmospheric oxygen in the absence of NO, the UV-vis absorption spectrum of *Cf* sGC1 did not change (Figure 3.3I; Figure 3.S4B), consistent with our prediction that *Cf* sGC1 is an NO-selective sGC and does not bind O_2. Moreover, like previously characterized animal sGCs, *Cf* sGC1 also binds CO to form a 6-coordinate, low spin CO-heme complex (Horst, Yokom, et al. 2019), evidenced by a Soret band maximum of 424 nm with two peaks in the α/β region (Figure 3.3I; Table S1). Thus, the UV-vis spectroscopy results indicate that *Cf* sGC1 binds diatomic gas ligands in a manner that resembles other well-characterized NO-selective sGCs. Finally, size exclusion chromatography

showed that *Cf* sGC1 formed a homodimer (Figure 3.S4A), reminiscent of the dimeric structure of animal sGCs.

In animals, NO-selective sGCs display three levels of activity: 1) in the absence of NO, the protein has a low basal guanylate cyclase activity; 2) when one NO molecule is bound at the heme moiety, the protein is partially activated (to several-fold the basal activity); and 3) in the presence of excess NO, the protein reaches maximal activation (Horst and Marletta 2018). To characterize the enzymatic activity of *Cf* sGC1, we measured cGMP production by purified *Cf* sGC1 under unliganded, equimolar NO, and excess NO conditions using an endpoint activity assay. We found that *Cf* sGC1 has an activity profile similar to that of animal sGCs, with a 2-fold increase in activity under equimolar NO concentration, and ~6-fold increase under excess NO (Figure 3.3J). Overall, *Cf* sGC1 exhibits similar ligand binding properties and NO-stimulated activity profile to animal NO-specific sGCs (Horst, Yokom, et al. 2019). These results further support the existence of NO/cGMP signaling in *C. flexa* and is consistent with it being mediated (at least in part) by *Cf* sGC1.

NO/cGMP signaling acts independently from most other inducers of colony contraction

In animals, NO signaling can be induced by a broad range of stimuli, which include chemical signals (for example, acetylcholine in mammalian blood vessels (Doyle and Duling 1997)), mechanical cues (for example, shear stress in blood vessels(Sriram et al. 2016)), or heat shocks (L. Zhang et al. 2013; Dulce et al. 2015; Rai, Pandey, and Rai 2020; Giovine et al. 2001). Interestingly, collar contractions in choanoflagellates can often be induced by mechanical stimuli, such as flow and touch (B.S. Leadbeater 1983a; James-Clark 1868; Nguyen et al. 2020; Andrews 1897). We thus set out to test whether NO signaling in *C. flexa* responds to or intersects with environmental inducers of inversion.

We observed that *C. flexa* colonies invert in a matter of seconds in response to agitation of culture flasks (which presumably combines the effect of flow and shocks with other colonies or the walls of the flask) and to heat shocks (Figure 3.4A,B). To test whether mechanically or heat-induced contraction requires NO/cGMP signaling, we incubated the colony cultures with the pan-sGC inhibitor ODQ and exposed them to either of the two different stressors. We found that inhibition of sGCs did not abolish mechanically induced or heat shock-induced contraction (Figure 3.4A,B). Taken together, these findings suggest that the mechanosensitive and thermosensitive pathways that induce inversion in *C. flexa* are independent of sGCs, and hint at complex behavioral regulation in this choanoflagellate.

Previous work has shown that *C. flexa* colonies invert in response to light-to-dark transitions which they detect through a rhodopsin-cGMP pathway (Brunet et al. 2019). In the presence of light, a rhodopsin-phosphodiesterase hydrolyzes cGMP into 5'GMP, thus preventing cGMP signaling. In darkness, the rhodopsin-phosphodiesterase is inactivated, which allows cGMP to accumulate and trigger colony inversion (Figure 3.1B). Interestingly, this pathway requires the presence of cGMP, which is presumably synthesized by either particulate (i.e. membrane-bound) or soluble (i.e. cytosolic) guanylate cyclases (X. Zhang and Cote 2005), both of which are

predicted to be encoded by the *C. flexa* transcriptome (Figure 3.S2C). A third family of guanylate cyclases, NIT-GCs, recently discovered in animals, could not be detected in choanoflagellates (Moroz et al. 2020).

We next set out to answer whether sGCs are necessary for synthesizing the cGMP required for phototransduction. To address this, we treated light-sensitive colonies with ODQ and found that this entirely abolished darkness-induced inversion (Figure 3.4C). These results suggest that sGCs (either NO-dependent or O_2-dependent) are responsible for synthesizing baseline levels of cGMP that are then used during phototransduction. Even though ODQ-treated light-sensitive colonies did not invert in response to darkness, we confirmed that they could still respond to NO by undergoing brief contractions (which were sustained for a much shorter time than in controls; Figure 3.4D), consistently with earlier results (Figure 3.3E).

Discussion

Here we report the presence of NOS, sGCs and downstream components of NO/cGMP signaling in three choanoflagellate species, at least two of which (*C. flexa* and *C. perplexa*) are capable of collective contractions (Brunet et al. 2019; B.S.C. Leadbeater 1983b). To our knowledge, this is the first observation of both NOS and sGCs in a non-animal. We found that NO causes sustained colony contraction in *C. flexa* and an increase in cGMP concentration in live cells, while inhibition of sGCs (and thereby reduction in cGMP concentration) accelerated colony relaxation. Moreover, *in vitro* experiments confirmed that NO directly binds *Cf* sGC1, which it activates with a two-step profile in response to different NO concentration, as in animal sGCs (Horst and Marletta 2018).

The observation that colonies treated with the sGC inhibitor initially contracted in response to NO at levels matching untreated colonies, only to relax much more quickly was unexpected. We hypothesize that NO-induced contractions are mediated through at least two different pathways: a slow pathway (described above) that maintains contraction and requires sGC/cGMP and an (unidentified) fast pathway independent of sGC/cGMP. Moreover, treatment of light-sensitive colonies with the sGC inhibitor abolished darkness-induced contractions (which are known to be mediated by cGMP (Brunet et al. 2019)) but did not prevent NO-induced contractions, further supporting the existence of a second pathway. In other organisms, cGMP-independent NO signaling can involve S-nitrosation, the modification of proteins through the formation of an S-NO covalent bond (Broniowska, Diers, and Hogg 2013; Smith and Marletta 2012), although the direct targets and functions of S-nitrosation in animals are less well understood than NO/cGMP signaling. It is possible that this mechanism explains the cGMP-independent pathway underlying NO-induced colony contraction in *C. flexa*.

The control of multicellular behavior by NO/cCMP signaling in *C. flexa* is reminiscent of its function in animals, most notably in sponges (Simion et al. 2017). In the demosponges *Tethya wilhelma* (Ellwanger and Nickel 2006), *Ephydatia muelleri* (Elliott and Leys 2010), and *Spongilla lacustris (Musser et al. 2021)*, NO induces global contractions and stops flagellar beating in choanocyte chambers, which interrupts feeding, allows expulsion of clumps of waste, and flushes the aquiferous canal system (a behavior sometimes called “sneezing”) (Elliott and Leys 2007). Recently, single-cell RNA sequencing in *Spongilla lacustris* revealed that pinacocytes (epithelial cells that cover and shape the sponge body) co-express NOS and sGC (Nickel et al. 2011; Musser et al. 2021), the actomyosin contractility module and the transcription factor *Serum response factor* (Srf), a master regulator of contractility (Musser et al. 2021; Miano, Long, and Fujiwara 2007; Brunet et al. 2016).

Control of motor and feeding behavior by NO/cGMP is also observed in cnidarians and some bilaterians. In the jellyfish *Aglantha digitale*, NO/cGMP signaling in neurons induces a switch from slow swimming (associated with feeding) to fast swimming (associated with escape) and inhibits tentacular ciliary beating (Moroz et al. 2004). In the sea pansy (a type of colonial cnidarian) *Renilla koellikeri*, NO/cGMP increases the amplitude of peristaltic contractions associated with the movement of body fluids through the gastrovascular cavity (Anctil, Poulain,

and Pelletier 2005). Finally, in the nudibranch *Clione limacine* and the snail *Lymnaea stagnalis,* NO activates both feeding and locomotory neural circuits (Moroz et al. 2000; Moroz and Kohn 2011; Moroz, Park, and Winlow 1993; Kobayashi et al. 2000). Thus, as in *C. flexa*, the ancient functions of NO/cGMP signaling in animals may include the regulation of feeding and contraction (Colasanti, Persichini, and Venturini 2010; Colasanti et al. 1997; Yabumoto et al. 2008; Cristino et al. 2008; Moroz and Kohn 2011; Jacklet 1997). Interestingly, NO signaling also controls metamorphosis in sponges (Ueda et al. 2016; Song, Hewitt, and Degnan 2021), gastropods (Froggett and Leise 1999), annelids (Biggers et al. 2012), echinoderms (Bishop and Brandhorst 2003, 2007) and ascidians (Bishop and Brandhorst 2003; Ueda and Degnan 2013; Comes et al. 2007), thus regulating a switch from swimming to feeding during irreversible developmental programs.

In the future, identifying the function of *Cf*NOS and *C. flexa* NO or O_2-selective sGCs will require gene knock-out, which is not yet possible in *C. flexa.* Moreover, studies on *Trichoplax* (in which NO/cGMP signaling has been predicted to exist based on genomic data (Moroz et al. 2020)), additional animal phyla, and other choanoflagellates will help flesh out reconstitutions of the early evolution of animal NO signaling.

Acknowledgments

We thank Daniel J. Richter for sharing the *Ministeria* predicted proteome, and the whole King and Marletta labs for stimulating discussions. This work was supported by an EMBO long-term fellowship (ALTF 1474–2016) to TB, a Human Frontier Science Program long-term fellowship (000053/2017 L) to TB, the Institut Pasteur (G5 package; TB), the Howard Hughes Medical Institute (NK), the National Institute of Health (NIH R01GM127854; MM, YW, BG)), and the National Science Foundation Graduate Research Fellowship Program (Grant No. 1752814; JRR).

Materials and Methods

Resource Availability

Lead contact

Further information and requests for resources and reagents should be directed to and will be fulfilled by the lead contact, Thibaut Brunet (thibaut.brunet@pasteur.fr).

Data and code availability

All NOS and sGC sequences from *C. flexa* were deposited onto GenBank (accession numbers below). All other data reported in this paper will be shared by lead contact upon request. This paper does not report original code. Any additional information required to reanalyze the data reported in this paper is available from the lead contact upon request.

Experimental Model and Subject Details

Culture of *Choanoeca flexa*

Colonies were cultured in 1% to 15% Cereal Grass Medium (CGM3) in artificial seawater (ASW). Polyxenic cultures (continuously passaged from a previously described environmental isolate (Brunet et al. 2019)) were maintained at 22°C under a light-dark cycle of 12:12 hours in a Caron low temperature incubator equipped with a lamp (Venoya Full Spectrum 150W Plant Growth LED) controlled by a programmable timer (Leviton VPT24^{-1}PZ Vizia). Polyxenic cultures used in most experiments were not light-sensitive, possibly due to progressive loss of bacterial diversity during serial passaging (as bacterially provided retinal is known to be required for photosensation in *C. flexa*(Brunet et al. 2019)). Light-sensitive sheets used in photosensation experiments (Figure 3.4C,D) were thawed from stocks that had been frozen immediately after clonal isolation from a Curaçao isolate and cultured as described above.

Method Details

Light microscopy – Imaging

Colonies were imaged in FluoroDishes (World Precision Instruments FD35-100) by differential interference contrast (DIC) microscopy using a 20x Zeiss objective mounted on a Zeiss Observer Z.1 with Hamamatsu Orca Flash 4.0 V2 CMOS camera (C1140-22CU).

Compound treatments and colony inversion assays

Small molecule inhibitor treatments and colony inversion assays were performed in 24-well plates (Fischer Scientific 09-761-146) containing 1 mL *C. flexa* culture per well. ODQ (pan-soluble guanylate cyclase inhibitor, BioVision 2051) was added 1 hour before behavioral assays.

Addition of each small molecule compound was followed by a gentle swirl of the 24-well plate to ensure mixing. For each assay, all colonies visible within a well were counted (at least 30 colonies per biological replicate). All behavioral experiments were conducted under ambient light in the laboratory, unless indicated otherwise.

NO donor-induced inversion: The NO donors proliNONOate (Cayman Chemical Company 82145) and DEANONOate (Cayman Chemical Company 82100) were dissolved according to provider's instructions and stored as single-use aliquots at -80°C. Addition of NO donor proliNONOate induced inversion within 1-2 minutes. Prior to counting, colonies were fixed by addition of 16% ice-cold PFA in a 1:3 volumetric ratio, resulting in a final concentration of 4% PFA. Contracted and relaxed colonies were then manually counted by observation under a Leica DMIL LED transmitted light microscope.

Light-induced sheet inversion: After treatment with small molecule compounds, light-to-dark transitions were performed by manually switching off the light source of the DMIL LED microscope. The "light off" condition lasted for one minute before sheets were fixed and scored as described above.

Mechanically induced sheet inversion: 3 mL of *C. flexa* culture were transferred to T12.5 culture flasks (Fisher Scientific 353107) and mechanically stimulated by vortexing on a Vortex Genie 2 (Scientific industries) on "Slow" setting for 5 seconds. Sheets were immediately fixed and scored as above.

Heat shock-induced sheet inversion: colonies in 24-well plates were treated with inhibitors as described above and placed at the surface of a 37°C warm bath for one minute. Sheets were immediately fixed and scored as above.

<u>cGMP ELISA</u>

For *in vivo* quantification of cGMP was performed with an ENZO Direct cGMP ELISA kit (ADI-900-014, 96 wells) as directed by the manufacturer. For each biological replicate, 90 mL of dense (>10^6 cells/mL) *C. flexa* culture was centrifuged for 5 minutes at 3000 x g and resuspended in 25 mL of ASW to wash the bacteria away. After the third wash, the cells were resuspended in 200 µL of ASW and split into one control (100 µL) and one treated sample (100 µL). The samples were lysed and quantified in parallel in each assay. Colonies from the "NO donor" group were treated with 0.25 µM proliNONOate 5 minutes before lysis. Values were read on a SpectraMax M3 plate reader (Molecular Devices).

<u>NO labeling, imaging, and image analysis</u>

C. flexa cultures were transferred into 15 mL Falcon tubes and vortexed in "fast" setting on a Vortex Genie 2 for one minute to dissociate colonies into single cells. Cells were washed 3 times with artificial seawater (ASW) by centrifuging them for 5 minutes at 3000 x g and resuspending them in 25 mL of ASW. After the last wash, cells were resuspended in 1.5 mL ASW and

transferred into a 1.5 mL Eppendorf tube. Cells were incubated in 10 µM DAF-FM (Invitrogen, D-23844) for 1 hour and rinsed twice with ASW to wash away the unincorporated dye. Cells were then transferred into a FluoroDish charged with a Corona surface treater and coated with poly-D-lysine, following a previously published protocol(Brunet et al. 2019). We let the cells adhere to the bottom of the dish for 30 minutes before imaging on a Z.1 Zeiss Imager with a Hamamatsu Orca Flash 4.0 V2 CMOS camera (C11440-22CU) and a 40x water immersion objective (C-Apochromat, 1.1 NA) for DIC and green epifluorescence imaging with a frame rate of 1 frame per minute. The NO donors (0.25 µM proliNONOate or 0.5 µM DEANONOate) were added 5 minutes after imaging began. We quantified intracellular fluorescence intensity using ImageJ. Change in fluorescence intensity was calculated by subtracting the fluorescence intensity at minute 1 from fluorescence intensity at minute 30.

Phylogenetic analysis and protein domain identification

We screened a selection of fully sequenced genomes for homologs of sGC and NOS with the following strategy: the protein sequences of *Homo sapiens* sGC-α1 and brain nitric oxide synthase (NOS1) were used as BLASTp queries against the NCBI database restricted to the following list of species:

- Eukaryotes: *Homo sapiens* (Hsa), *Branchiostoma floridae* (Bfl)*, Drosophila melanogaster* (Dme)*, Capitella teleta* (Cte)*, Nematostella vectensis* (Nve)*, Amphimedon queeslandica* (Amq)*, Mnemiopsis leidyi, Trichoplax adhaerens* (Tadh)*, Salpingoeca rosetta* (Sro)*, Capsaspora owczarzaki, Sphaereoforma arctica* (Sphac)*, Abeoforma whisleri, Creolimax fragrantissima, Pirum gemmata, Aspergillus oryzae* (Asory)*, Jimgerdemannia flammicorona* (Jifla)*, Rhizoctonia solani* (Rhiso)*, Pterula gracilis* (Ptegra)*, Schizosaccharomyces pombe, Tuber melanosporum, Cryptococcus neoformans, Ustilago maydis, Cryptococcus neoformans, Ustilago maydis, Rhizopus oryzae, Allomyces macrogynus, Batrachochytrium dendrobatidis, Spizellomyces punctatus, Thecamonas trahens, Dictyostelium discoideum, Polysphondylium pallidum, Entamoeba histolytica, Arabidopsis thaliana, Selaginella moellendorffii, Physcomitrella patens, Chlamydomonas reinhardtii, Volvox carteri* (Vcar)*, Chlorella variabilis* (Chl)*, Ostreococcus tauri* (Ostau)*, Ectocarpus siliculosus, Phaeodactylum tricornutum, Thalassiossira pseudonana, Phytophthora infestans, Toxoplasma gondii, Tetrahymena thermophila, Perkinsus marinus, Guillardia theta, Naegleria gruberi* (Ngru)*, Trypanosoma cruzi, Leishmania major, Trichomonas vaginalis, Giardia lamblia, Bigelowiella natans, Emiliania huxleyi*
- Archaea: *Nanoarchaeum equitans, Ignicoccus islandicus, Natronolimnobius baerhuensis, Halorientalis regularis, Halostagnicola kamekurae, Halalkalicoccus subterraneus, Halobiforma nitratireducens* (Halob)*, Natronobacterium gregoryi* (Natr)*, Haloplanus natans, Halovenus aranensis* (Halar)*, Halonotius pteroides* (Halo)
- Bacteria: *Actinocrispum wychmicini* (Actin)*, Kibdelosporangium aridum* (Kibd)*, Crossiella equi* (Cross)*, Lentzea xinjiangensis* (Lentz)*Nocardioides speluncae* (Noc)*, Saccharopolyspora spinosa* (Sspi)*, Synechococcus sp. PCC 7335* (Syn)*, Nostoc cycadae* (Nocyc)*, Anabaenopsis circularis* (Ancir)*, Planktothrix paucivesiculata* (Plank)*, Crinalium epipsammum* (Crinep)*, Spirosoma radiotolerans* (Spiro)*, Roseinatronobacter monicus* (Rose)

Additional BLASTp searches were conducted against a published dataset of 19 choanoflagellate transcriptomes (Richter et al. 2018), the *C. flexa* transcriptome(Brunet et al. 2019) and the *Ministeria vibrans* transcriptome (Torruella et al. 2015) (and courtesy of Daniel J. Richter). The *C. flexa* NOS and sGC predicted protein sequences were deposited onto GenBank with the following accession numbers: ON075806 (for *Cf* NOS), ON075810 (for *Cf* sGC1), ON075809 (for *Cf* sGC2), ON075808 (for *Cf* sGC3), and ON075807 (for *Cf* sGC4).

Domain architectures were predicted using the CD-search tool from NCBI. For phylogenetic reconstructions, sequences were aligned using Clustal implemented in Geneious Prime (2021 version). The NOS sequence alignment was manually trimmed to be restricted to the oxygenase domain and the sGC alignment was trimmed using Gblocks with minimally stringent parameters. Phylogenetic trees were reconstructed using PhyML and BMGE implemented on http://phylogeny.lirmm.fr/phylo_cgi/index.cgi (Dereeper et al. 2008). Trees were visualized using iTOL (https://itol.embl.de/) (Letunic and Bork 2021) and further edited in Adobe Illustrator (2021 version). Species silhouettes were added from PhyloPic (http://phylopic.org/).

Construction of expression plasmid

First-strand *C. flexa* cDNA (extracted as in (Brunet et al. 2019)) was used as the template for cloning *Cf* sGC1. Forward and reverse primers were designed against 5' and 3' ends of the target transcript (transcript name: TRINITY_DN6618_c0_g1_i1 in the published transcriptome(Brunet et al. 2019)). Forward: TAAGAAGGAGATATACCATG TATGGCTTGGTGCACGAAGC; reverse: TAATGGTGATGATGGTGATG AACTATAGTCTGCTTGCCAACG. Underlined portions anneal to the sequence template. The PCR product was inserted into a pET28b vector using Gibson assembly, and the cloning product was verified by sequencing (UC Berkeley sequencing facility).

Protein expression and purification

pET_*Cf*sGC1 was transformed into *E. coli* BL21star (DE3) cells co-expressing the chaperone GroEL/ES from the pGro7 plasmid (Takara Biosciences). After overnight incubation at 37 °C in LB Miller media supplemented with 50 µg/mL kanamycin, 20 µg/mL chloramphenicol and 500 µM iron (III) chloride, cells were subcultured 1:200 into TB media supplemented with 50 µg/mL kanamycin, 20 µg/mL chloramphenicol, 500 µM iron (III) chloride, 0.5 mg/mL L-arabinose, and 2 mg/mL glucose, grown at 37 °C. Once cell density reached OD_{600} = 0.6, 1 mM 5-aminolevulinic acid was added to the culture, and culturing temperature was lowered to 18 °C. After 15 minutes of incubation, protein production was induced by addition of 500 µM isopropyl β-D-1-thiogalactopyranoside and cultures were incubated for an additional 18 hours. Cell culture was harvested by centrifuging at 4200 g for 25 min. Cells were collected, flash frozen in liquid nitrogen, and stored at -80 °C until purification.

All protein purification steps were done at 4 °C unless otherwise noted. Cells were resuspended in equal volume of buffer A (50 mM sodium phosphate, 150 mM NaCl, 5 mM imidazole, 5% glycerol, pH 8.0) supplemented with 110 mM benzamidine, 0.4 mM AEBSF, and 0.3 mg/mL

DNase. Cell resuspension was lysed using an Avestin EmulsiFlex-C5 homogenizer. Cell lysate was collected and clarified by centrifugation at 32,913 g for 55 min, and the supernatant was collected and loaded onto a His60 Ni Superflow gravity column (Takara Bio). The column was washed twice, first with 10 CV buffer A, and then with 10 CV of a 9:1 mixture of buffer A and buffer B (50 mM sodium phosphate, 150 mM NaCl, 400 mM imidazole, 5% glycerol, pH 8.0). Protein was eluted with 5 CV buffer B in 1 mL fractions. Fractions with heme absorbance were pooled and concentrated using a 50kDa cutoff spin concentrator and supplemented with 5 mM DTT and 1 mM EDTA for overnight storage. Subsequently, protein was passed over a POROS HQ2 anion exchange column (Applied Biosystems). After loading, the column was washed with 5 CV of buffer C (25 mM triethanolamine, 25 mM NaCl, 5 mM DTT, pH 7.4) and developed over a gradient of 100 mM – 300 mM NaCl over 17 CV. The protein absorption spectrum was measured using a Nanodrop 2000 microvolume spectrophotometer (ThermoFisher Scientific). Subsequently, protein was aliquoted, flash frozen in liquid nitrogen, and stored at -80 °C for future use.

Analytical size exclusion chromatography

Purified *Cf* sGC1 and the protein standard mixture were injected onto a Superdex 200 Increase 10/300 GL column (GE healthcare) equilibrated with buffer F (50 mM triethanolamine, 150 mM NaCl, 5 mM DTT, 5% glycerol). Protein elution was monitored by UV absorbance at 280 nm.

Gas ligand binding of bacterial-produced *Cf* sGC1

Cf sGC1 was handled in an argon-filled glove bag. Protein-bound heme was reduced by adding sodium dithionite (~500-fold excess over the protein conc.). Excess dithionite was removed by gel filtration of the protein into Buffer E (50 mM HEPES, 150 mM NaCl, 5% glycerol, pH 7.4) using a pre-equilibrated Zeba spin desalting column. A ferrous, ligand-free UV-vis absorption spectrum was collected on a Cary 300 UV-vis Spectrophotometer. Fe(II)-NO bound *Cf* sGC1 was generated by adding the NO-releasing molecule proliNONOate (~10-fold excess) to the protein sample, and Fe(II)-CO bound *Cf* sGC1 was generated by adding CO-sparged Buffer E to the protein sample before collecting a spectrum.

Extinction coefficient of *Cf* sGC1

The extinction coefficient of the Soret maximum of reduced *Cf* sGC1 was measured using two assays performed in tandem: heme concentration in a sample of *Cf* sGC1 was determined using pyridine hemochromagen assay, and the heme Soret absorption of the protein sample was measured using UV-vis spectroscopy as described above. The pyridine hemochromagen assay was carried out following a reported protocol (Barr and Guo 2015). Briefly, a reduced protein sample with a known Soret band absorbance was diluted 5-fold in Buffer E, and then further diluted 2-fold in Solution I (0.2 M NaOH, 40% pyridine, 500 µM potassium ferricyanide) to yield the oxidized pyridine hemochromagen. An aliquot (10 µL) of Solution III (0.5 M sodium dithionite, 0.5 mM NaOH) was then added to the oxidized pyridine hemochromagen sample to yield the reduced pyridine hemochromagen. The UV-vis absorption spectrum of the reduced

pyridine hemochromagen was measured on a Cary 300 UV-vis spectrophotometer. Absorption at 557 nm(ε = 34,700 $mM^{-1}cm^{-1}$) was used to calculate the heme concentration in the pre-dilution sample, and the extinction coefficient of the heme cofactor of *Cf* sGC1 was calculated by dividing the reduced heme absorption by the heme concentration.

Activity assays and quantification

Specific activity for *Cf* sGC1 was measured by quantifying the amount of cGMP produced in duplicate end-point activity assays, done in biological triplicate. *Cf* sGC1 from previously frozen aliquots was thawed and reduced in an anaerobic chamber as described above. The reduced protein was used without further treatment for the basal (unliganded) activity assay. A UV-vis spectrum for the unliganded sample was obtained using a Nanodrop 2000 microvolume spectrophotometer, and the Soret maximum was used to quantify heme-bound protein concentration (ε_{428} = 101,000 $M^{-1}cm^{-1}$). Only protein with a Soret:280 ratio > 1 was used for activity assays. To the remaining reduced protein, proliNONOate was added to a final concentration of 400 µM by the addition of 1 µL of a stock solution of 10 mM proliNONOate in 10 mM NaOH, and the protein sample was incubated at 4 °C for 5 min to yield the xsNO sample. The xsNO-bound UV-vis spectrum was then collected. The protein concentration of the xsNO sample was assumed to be the same as the unliganded sample. The xsNO sample was then buffer exchanged by gel filtration using a Zeba spin column into buffer E to yield the 1-NO sample, and the UV-vis spectrum was collected. The concentration of the 1-NO sample was calculated based on the NO-bound Soret absorbance at 399 nm compared to that of the xsNO sample. Activity assays were carried out at 25 °C in Buffer E supplemented with 5 mM DTT and 3 mM $MgCl_2$ with *Cf* sGC1 concentration at 40 nM. To obtain the xsNO state, 70 µM proliNONOate was added. The reaction was initiated by addition of 1.5 mM GTP, and timepoints were quenched by diluting the reaction mixture 1:4 to a solution of 125 mM zinc acetate, and pH adjusted by adding equal volume of 125 mM sodium carbonate. Assay samples were stored at -80 °C until analyzed. Quenched assay samples were thawed at room temperature, centrifuged at 21,130 x g at 4 °C to remove zinc precipitate. Supernatant was collected and diluted 250-fold for the analysis. cGMP content of each assay sample was quantified in duplicate using an enzyme-linked immunosorbent assay (Enzo Life Sciences) following the manufacturer's protocol. Initial rate of the reaction was calculated using the linear phase of the time course, where <10% of substrate has been depleted.

Quantification And Statistical Analysis

Information about the quantification and statistical details of experiments can be found in the corresponding figure legends.

Figures

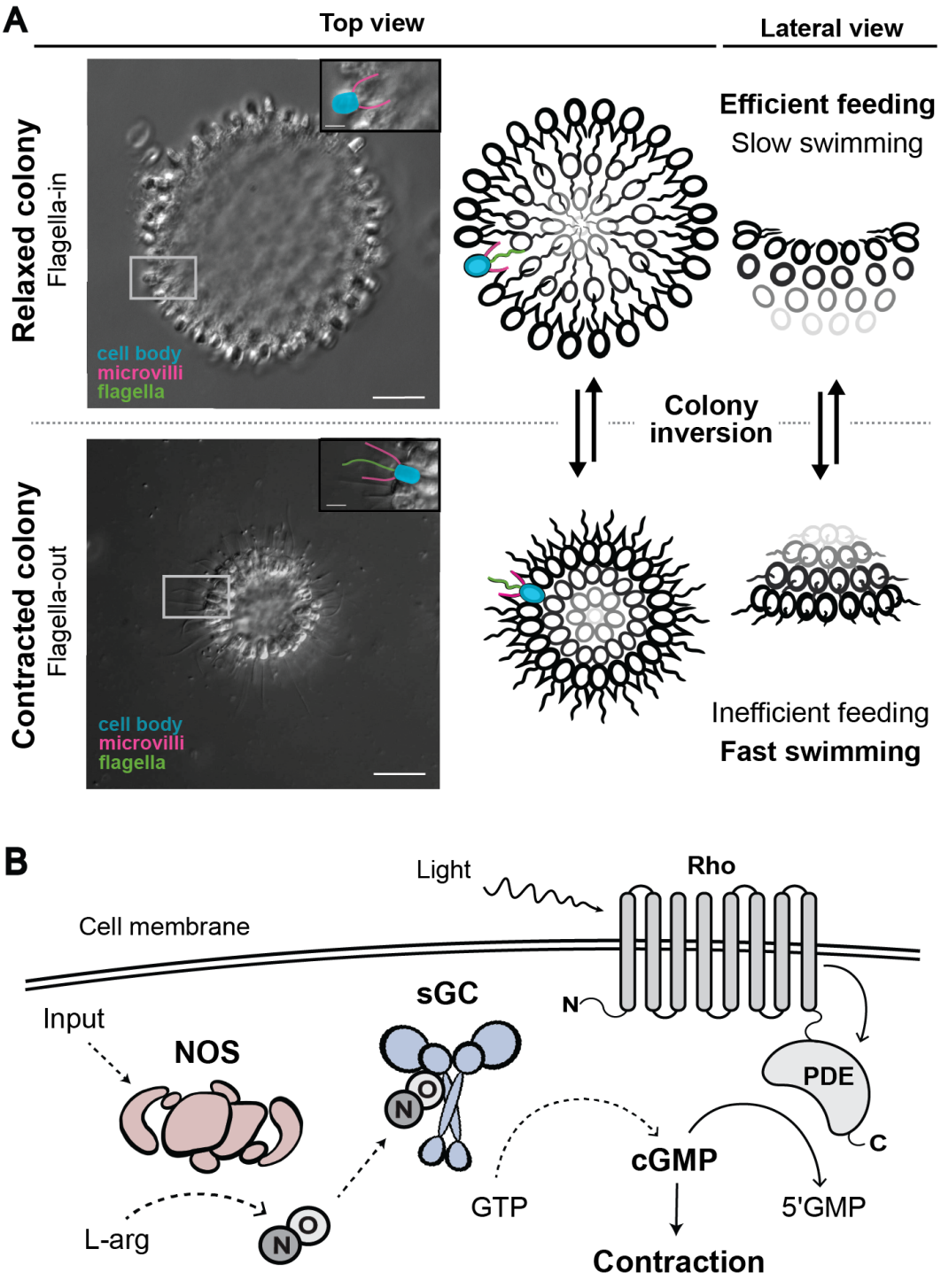
A
Top view
Lateral view
Relaxed colony
Flagella-in
cell body
microvilli
flagella
Efficient feeding
Slow swimming
Colony inversion
Contracted colony
Flagella-out
cell body
microvilli
flagella
Inefficient feeding
Fast swimming
B
Light
Rho
Cell membrane
Input
NOS
sGC
N
PDE
C
cGMP
GTP
5'GMP
L-arg
Contraction

Figure 3.1. The inversion behavior of *C. flexa*, its control by light and hypothesized control by NO.

(**A**) Micrograph (left) and schematic depiction (right) of *C. flexa* inversion behavior. Cells are linked by their collars and form a cup-shaped monolayer or sheet; scale bar: 15 µM. Relaxed colonies (top half) have their flagella pointing towards the inside of the colony and are efficient feeders and slow swimmers. (Flagella from relaxed colony are not in focus in the micrograph; see schematic for flagellum orientation.) Contracted colonies (bottom half) have their flagella pointing towards the outside of the colony and are inefficient feeders but fast swimmers. Insets: Pseudo-colors highlight the characteristic morphological features of choanoflagellates: flagella (green), cell body (blue), and microvilli (magenta). Inset scale bar: 5 µm. (**B**) *C. flexa* colony inversion is controlled by light-to-dark transitions, mediated by a rhodopsin-phosphodiesterase fusion protein (Rho-PDE) upstream cGMP signaling. In the presence of light, Rho-PDE is active and constantly converting cGMP into 5'GMP. We hypothesized that NO/cGMP signaling might also be able to induce inversion. Mechanisms tested in this paper are indicated with dashed lines: a primary input activates the nitric oxide synthase (NOS), which converts L-arginine into NO and L-citrulline. NO diffuses away and activates soluble guanylate cyclase (sGC) which convert GTP into cGMP, causing colony contraction.

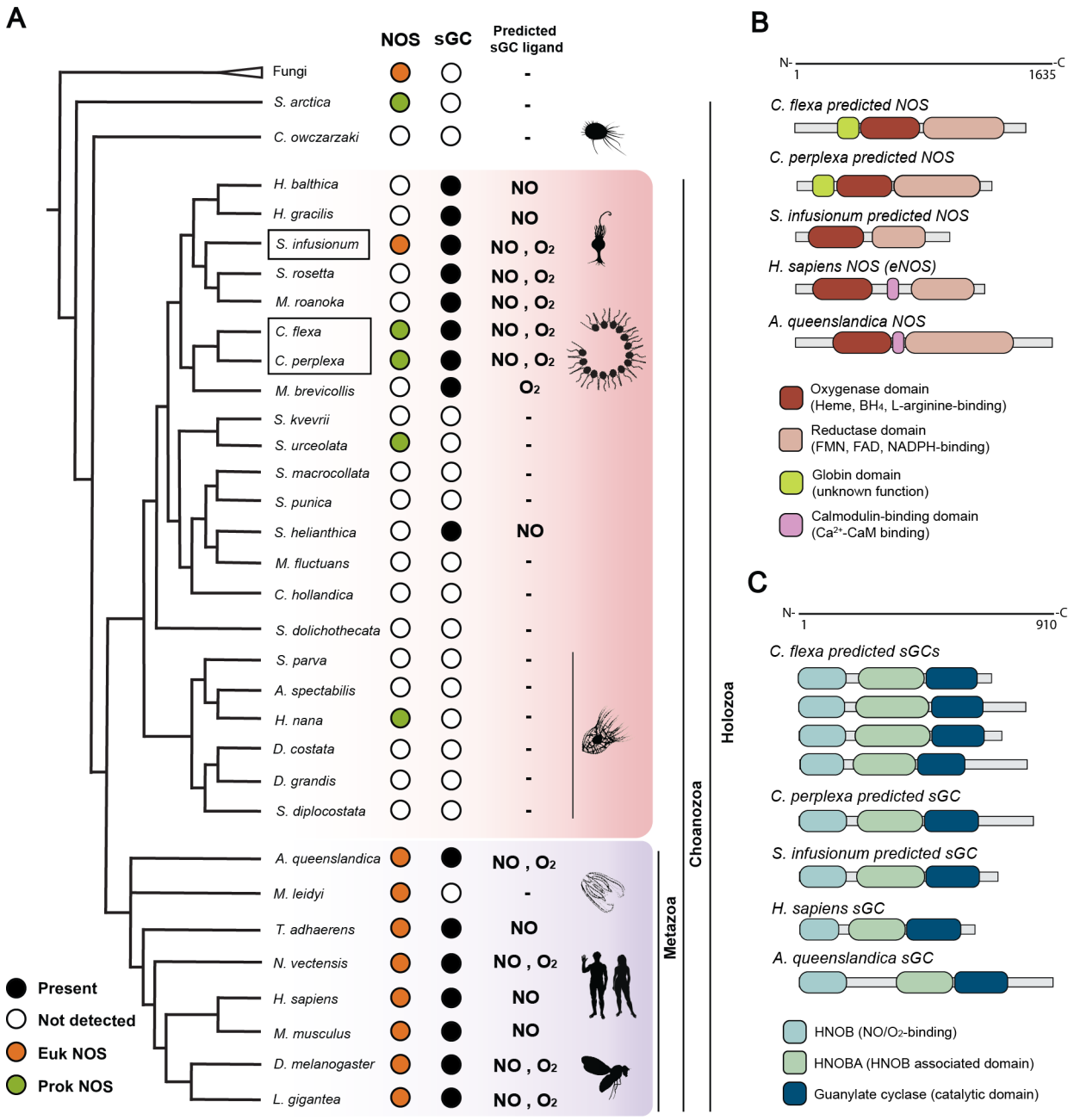

Figure 3.2. NO synthase (NOS) and soluble guanylate cyclases (sGC) predicted to bind either NO or O_2 are broadly distributed across choanozoans, and all three are present in *C. flexa*. (**A**) Phylogenetic distribution of NOS and sGC across opisthokonts. *C. flexa*, its sister species *C. perplexa*, and *S. infusionum* encode both NOS and NO-sensitive sGCs, as do animals. (**B**) Choanoflagellate NOSs have the metazoan canonical oxygenase and reductase domain but lack the calcium-calmodulin binding domain. *C. flexa* and other choanoflagellate NOS encode an upstream globin domain with unknown function, also observed in cyanobacterial NOS. (**C**) *C. flexa* sGCs have the same domain architecture as animal sGCs. See Figure S1 for phylogenetic analysis and Figure 3.S2 for phylogenetic distribution of NO/cGMP downstream components.

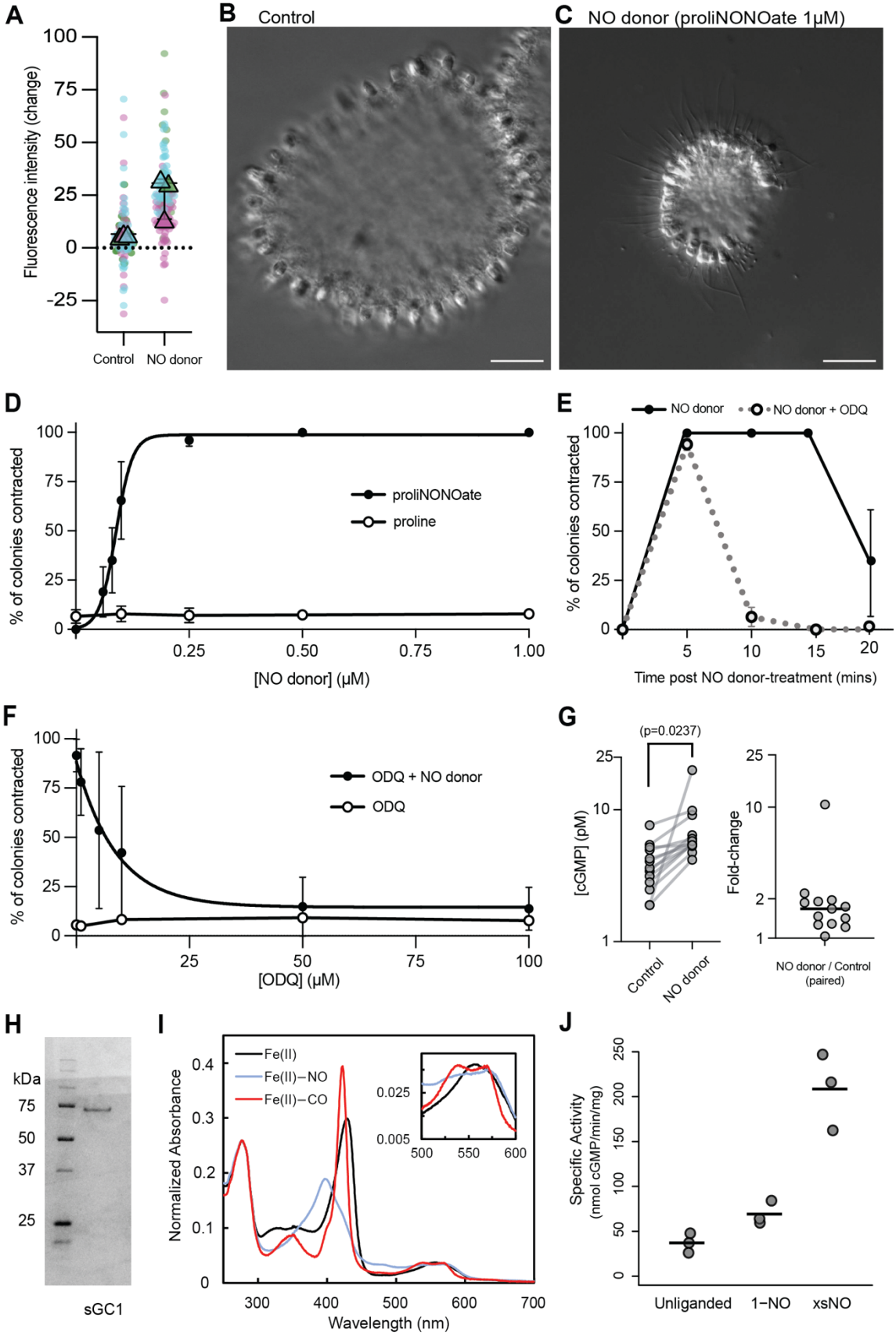
A
Fluorescence intensity (change)
100
75
50
25
0
-25
Control
NO donor
B
Control
C
NO donor (proliNONOate 1µM)
D
% of colonies contracted
proliNONOate
proline
0.25
0.50
0.75
1.00
[NO donor] (µM)
E
NO donor
NO donor + ODQ
% of colonies contracted
5
10
15
20
Time post NO donor-treatment (mins)
F
% of colonies contracted
ODQ + NO donor
ODQ
25
50
75
100
[ODQ] (µM)
G
(p=0.0237)
[cGMP] (pM)
Control
NO donor
Fold-change
NO donor / Control
(paired)
H
kDa
75
50
37
25
sGC1
I
Fe(II)
Fe(II)−NO
Fe(II)−CO
Normalized Absorbance
0.4
0.3
0.2
0.1
0
0.025
0.005
500
550
600
300
400
500
600
700
Wavelength (nm)
J
Specific Activity
(nmol cGMP/min/mg)
250
200
150
100
50
0
Unliganded
1−NO
xsNO

Figure 3.3. NO induces sustained colony contraction in *C. flexa* and activates *Cf* sGC1.
(**A**) NO release by proliNONOate was visualized by loading cells with the NO-sensitive fluorescent probe DAF-FM and measuring the change in intracellular fluorescence intensity over 30 minutes. Cells treated with NO donor showed a higher increase in fluorescence. Graph is a SuperPlot(Lord et al. 2020) of N=3 biological replicates per condition, with sample sizes n=27, 33, 47 for the three control groups and n=26, 57, 42 for the three treated groups. *p*=0.0331 by an unpaired t-test. See Figure S3A-C for a similar analysis using the NO donor DEANONOate. (**B-C**) NO induces colony contraction. While colonies treated with a negative control compound (proline) remained relaxed, colonies treated with 0.25 µM of the NO donor proliNONOate contracted within 1-2 minutes. (**D**) The NO donor proliNONOate induces contractions within ~1-2 minutes in a dose-dependent manner. A closely related molecule incapable of releasing NO (proline) had no effect over the same concentration range. Figure S3D shows NO-induced contractions using different NO donors. (**E**) Inhibition of sGCs with 50 µM ODQ did not abolish NO-induced contraction at early time points but greatly reduced its duration. ODQ-treated colonies were contracted within 5 minutes post-treatment with NO donor but relaxed soon after, while untreated colonies remain contracted for at least 5 more minutes. (**F**) Inhibition of sustained contraction by ODQ is dose-dependent. Colonies were incubated with different concentrations of ODQ for 1 hour before treatment with 0.25 µM of the NO donor proliNONOate. We quantified the percentage of contracted colonies 10 minutes after NO treatment. In (**D-F**) each point represents the mean value of N=3 biological replicates with at least 30 colonies scored per biological replicate. Error bars are standard deviations. (**G**) Treatment of cells with a NO donor increased intracellular cGMP concentration almost 2-fold as quantified by ELISA. N=13 pairs of control/treated samples, *p*=0.024 by a paired T-test. (**H-J**) Purification, ligand binding properties and specific activity of *Cf* sGC1. (**H**) Coomassie-stained SDS-PAGE gel of recombinant *Cf* sGC1 expressed in *E. coli* and purified. Band in lane "sGC1" represents *Cf* sGC1 with a monomeric molecular weight of 75.7 kDa. Left lane, molecular weight ladder. (**I**) UV-visible absorption spectra of *Cf* sGC1 under unliganded (black), NO-bound (blue), and CO-bound (red) conditions. Soret maxima: NO-bound: 429 nm; CO-bound: 423 nm; NO-bound: 399 nm. Inset, α/β bands show increased splitting upon ligand binding. (**J**) Specific activity of *Cf* sGC1 under unliganded, equimolar quantities of NO (1-NO) and excess NO (xsNO) conditions. Initial rates were measured from activity assays performed at 25°C, pH 7.5 with 1.5 mM Mg^{2+}-GTP substrate and 40 nM enzyme. Horizontal bars represent mean of three biological replicates.

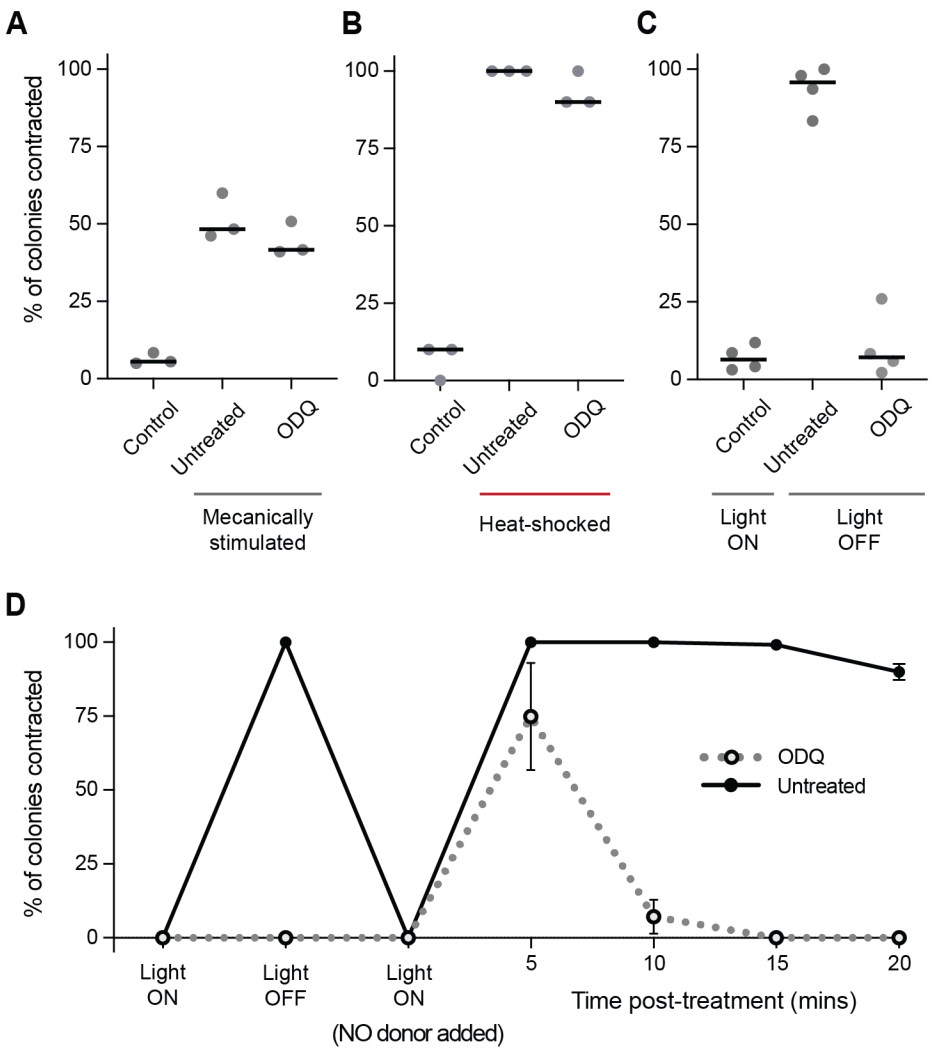

Figure 3.4. NO/cGMP acts independently of most other inducers of contraction in *C. flexa*. (**A-B**) Mechanical stimuli and heat-shock induce *C. flexa* colony contraction. Inhibition of sGC (50 µM ODQ) did not have an effect on mechanically or heat shock-induced contractions. (**C**) Inhibition of sGC (50 µM ODQ) abolished darkness-induced inversion ($p<0.0001$ by an unpaired t-test). (**D**) Colonies treated with ODQ did not respond to on/off changes in light but briefly contracted when exposed to NO donor, consistent with earlier results (Figure 3D-F). 10 minutes after treatment, ODQ-treated colonies were relaxed, while untreated colonies remained contracted for a longer period. In (**A-D**) each point is the average of N=3 (**A-B**) or N=4 (**C-D**) biological replicates with at least n=30 colonies scored per biological replicate. Error bars are standard deviations.

Supplementary Materials

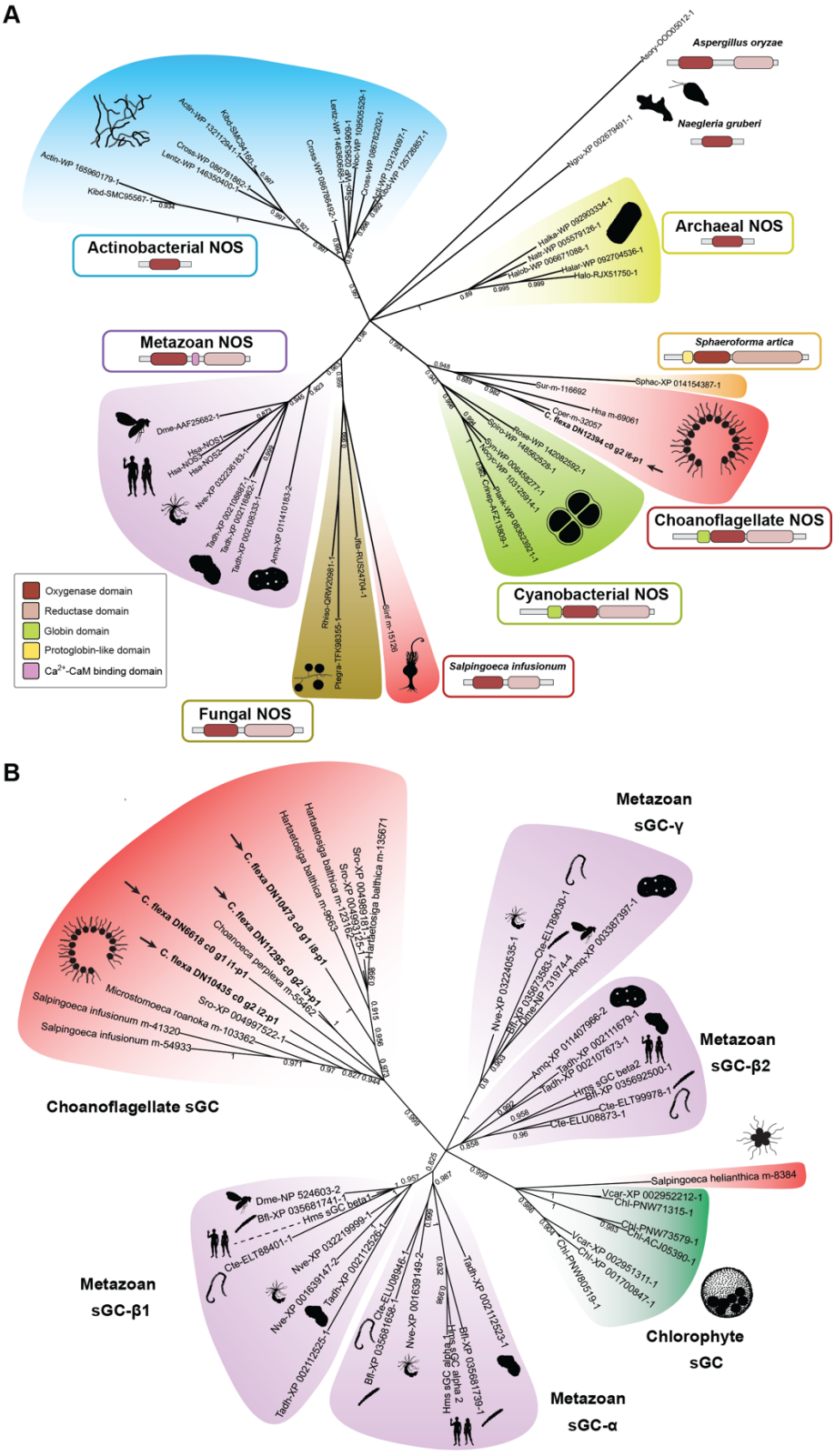

Figure 3.S1. Phylogenetic tree of NOS and sGC, related to Figure 2.
(**A**) Phylogenetic tree of NOS from a selection of fully sequenced eukaryotic, archaeal, and bacterial genomes. Alignments and phylogenetic reconstruction were performed on the oxygenase domain only. The clades recovered tend to share common domain architectures out of the oxygenase domain (such as the reductase domain in eukaryotic NOSs and the globin domain in choanoflagellate and cyanobacterial NOSs), providing independent support to the phylogeny. The sister-group relationship between choanoflagellate and cyanobacterial NOSs as well as the shared domain architecture suggest a history of horizontal gene transfer. See Material and Methods for species name abbreviations. (**B**) Phylogenetic tree of sGC from a selection of fully sequenced animal and chlorophyte genomes, and choanoflagellate genomes and transcriptomes. Analysis was performed based on the full protein sequence. See Material and Methods for species name abbreviations.

A

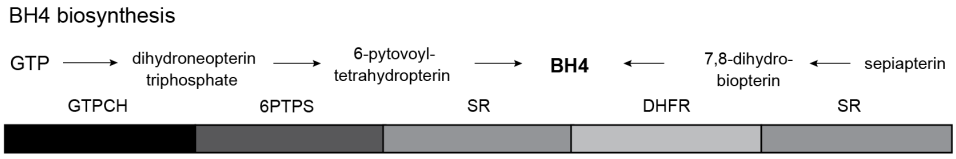
BH4 biosynthesis
GTP
dihydroneopterin triphosphate
6-pytovoyl-tetrahydropterin
BH4
7,8-dihydro-biopterin
sepiapterin
GTPCH
6PTPS
SR
DHFR
SR

B

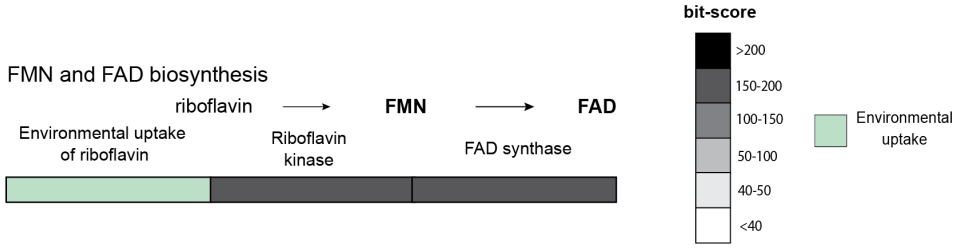
FMN and FAD biosynthesis
riboflavin
FMN
FAD
Environmental uptake of riboflavin
Riboflavin kinase
FAD synthase
bit-score
>200
150-200
100-150
50-100
40-50
<40
Environmental uptake

C

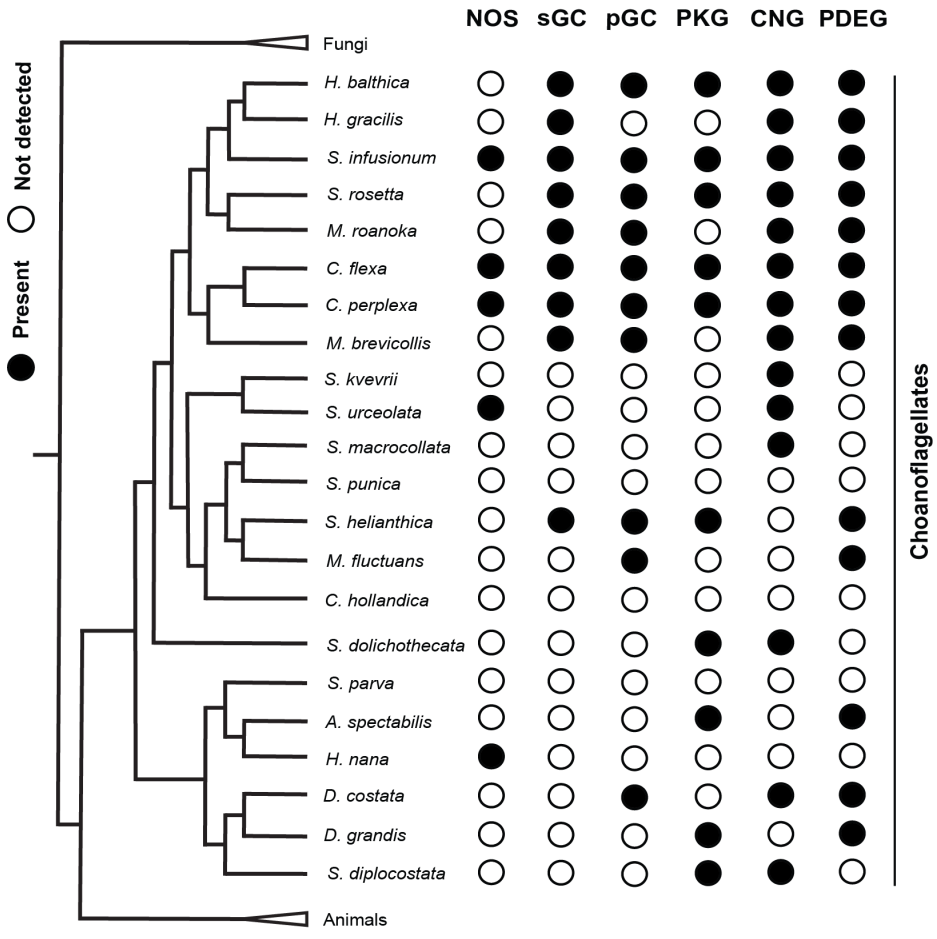
NOS
sGC
pGC
PKG
CNG
PDEG
Not detected
Present
Fungi
H. balthica
H. gracilis
S. infusionum
S. rosetta
M. roanoka
C. flexa
C. perplexa
M. brevicollis
S. kvevrii
S. urceolata
S. macrocollata
S. punica
S. helianthica
M. fluctuans
C. hollandica
S. dolichothecata
S. parva
A. spectabilis
H. nana
D. costata
D. grandis
S. diplocostata
Animals
Choanoflagellates

D

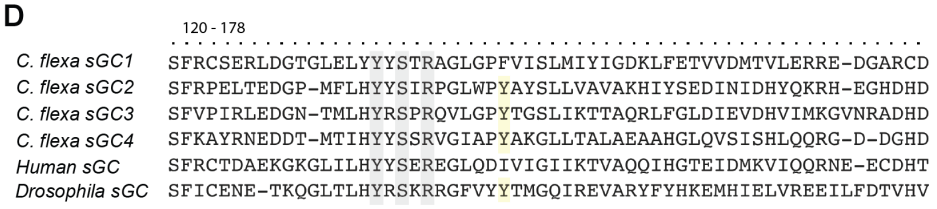
120 - 178
C. flexa sGC1 SFRCSERLDGTGLELYYYSTRAGLGPFVISLMIYIGDKLFETVVDMTVLERRE-DGARCD
C. flexa sGC2 SFRPELTEDGP-MFLHYYSIRPGLWPYAYSLLVAVAKHIYSEDINIDHYQKRH-EGHDHD
C. flexa sGC3 SFVPIRLEDGN-TMLHYRSPRQVLGPYTGSLIKTTAQRLFGLDIEVDHVIMKGVNRADHD
C. flexa sGC4 SFKAYRNEDDT-MTIHYYSSRVGIAPYAKGLLTALAEAAHGLQVSISHLQQRG-D-DGHD
Human sGC SFRCTDAEKGKGLILHYYSEREGLQDIVIGIIKTVAQQIHGTEIDMKVIQQRNE-ECDHT
Drosophila sGC SFICENE-TKQGLTLHYRSKRRGFVYYTMGQIREVARYFYHKEMHIELVREEILFDTVHV

Figure 3.S2. *C. flexa* encodes the complete biosynthetic pathways for the NOS cofactors and downstream NO/cGMP signaling components, related to Figure 3.2.
(**A-B**) The *C. flexa* transcriptome was searched for genes encoding enzymes in the tetrahydrobiopterin (BH4; A) and FMN/FAD (**B**) biosynthesis pathways using BLASTP. For each step in the pathway, multiple bacterial, plant, fungal and/or animal genes were used as queries (see Methods), and the highest returned bit-score is shown. *C. flexa* encodes the complete biosynthetic pathway. Riboflavin is assumed to be uptaken from the environment[S1]. (**C**) Phylogenetic distribution of guanylate cyclases (soluble: sGC, and membrane-bound: pGC), and cGMP signaling downstream components. In animals, cGMP is known to signal through cGMP-dependent kinases (PKG), cGMP-gated ion channels (CNG) and cGMP-dependent phosphodiesterases (PDEG). The three choanoflagellate species detected to express a NOS and sGC (*C. flexa*, *C. perplexa* and *S. infusionum*) also express PKG, CNG and PDEG. (**D**) Preferential binding predictions were made for *C. flexa* sGCs based on NO-sensitive and O_2-binding metazoan sGCs[S2,S3,S4]. *C. flexa* sGC partial alignment with human sGC (NO-sensitive) and *Drosophila* sGC (O_2-binding). Amino acids important for heme binding are highlighted in grey. A distal tyrosine residue is highlighted in yellow, previously shown to be highly important for O_2 binding[S5]. One NO-sensitive (sGC1) and three O_2-binding sGCs (sGC2, sGC3, sGC4) were predicted.

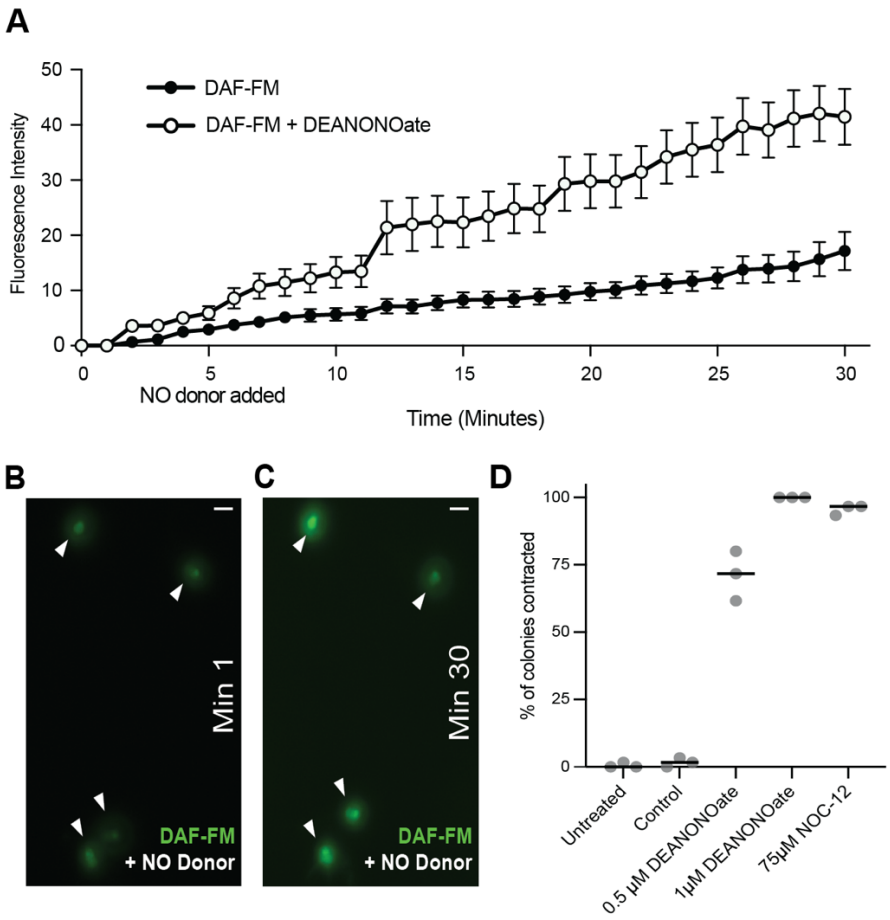

Figure 3.S3. Treatment with NO donors increase intracellular NO levels and induce colony contraction, related to Figure 3.3.

(**A-C**) Intracellular NO levels over time. NO was labeled with the fluorescent probe DAF-FM and the fluoresce intensity was measured every minute for 30 minutes. NO donor DEANONOate was added at minute five. Intracellular fluorescence in NO donor-treated cells display a higher increase over time compared to control. Small increase in fluorescence in control group may be explained by unwashed dye incorporating inside of the cells and/or basal physiological NO levels. Intracellular intensity was measured using Image J software. (**B-C**) Representative micrographs are shown on the right. White arrows are pointing individual cells. Scale bar: 5 µM. NO donor was added at minute five. (**D**) NO donors DEANONOate and NOC-12 also induce colony contraction. Colonies from control group were treated with DMSO.

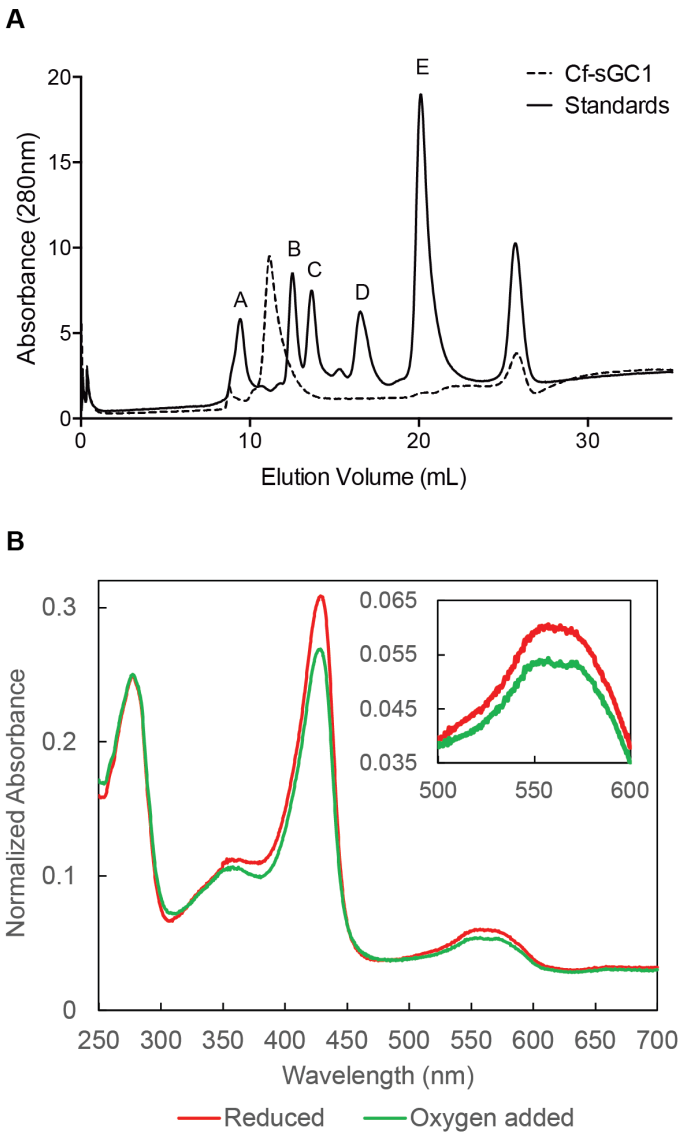

Figure 3.S4. Analytical size exclusion chromatography of *Cf* sGC1 and UV-vis spectrum of *Cf* sGC1 upon exposure to O_2, related to Figure 3.4.

(**A**) *Cf* sGC1 eluted at ~150 kDa during the analytical size exclusion chromatography, consistent with being a homodimer of 75.7 kDa monomers. Protein standards: A, thyroglobulin, 670 kDa; B, alcohol dehydrogenase, 150 kDa; C, bovine serum albumin, 66.5 kDa; D, DNAse I, 31 kDa; E, lysozyme, 14 kDa. (**B**) The UV-vis spectrum of *Cf* sGC1 upon exposure to O_2, normalized to A_{280}. The Soret to A_{280} ratio decreased when oxygen was added to the sample, which could indicate oxidation of the heme and loss of the heme through the process. There was no observable formation of a low-spin 6-coordinate Fe(II)-O_2 complex (as indicated by the lack of shift of the Soret peak).

Supplementary Table S1, and Movie S1 can be found online at https://doi.org/10.1016/j.cub.2022.04.017

Table S1. *Cf* sGC1 UV-vis absorption wavelengths; *Rattus norvegicus* sGC is a well characterized, NO-selective sGC, related to Figure 3.3.

Video S1. NO-induced *C. flexa* colony contraction, related to Figure 3.2.

References

Adl, Sina M., David Bass, Christopher E. Lane, Julius Lukeš, Conrad L. Schoch, Alexey Smirnov, Sabine Agatha, et al. 2019. “Revisions to the Classification, Nomenclature, and Diversity of Eukaryotes.” *Journal of Eukaryotic Microbiology* 66 (1): 4–119.

Aizawa, Hiroyuki, Maiko Katadae, Mikako Maruya, Masazumi Sameshima, Kimiko Murakami-Murofushi, and Ichiro Yahara. 1999. “Hyperosmotic Stress-Induced Reorganization of Actin Bundles in Dictyostelium Cells over-Expressing Cofilin.” *Genes to Cells* 4 (6): 311–24.

Anctil, M., I. Poulain, and C. Pelletier. 2005. 'Nitric oxide modulates peristaltic muscle activity associated with fluid circulation in the sea pansy Renilla koellikeri', *J Exp Biol*, 208: 2005-17.

Andreakis, N., S. D'Aniello, R. Albalat, F. P. Patti, J. Garcia-Fernandez, G. Procaccini, P. Sordino, and A. Palumbo. 2011. 'Evolution of the nitric oxide synthase family in metazoans', *Mol Biol Evol*, 28: 163-79.

Andrews, G. F. 1897. 'The living substance as such and as organism', *Supplement to Journal of Morphology*, XII N. 2.

Amsalem, Eyal, and Gil Rilov. 2021. “High Thermal Plasticity, and Vulnerability, in Extreme Environments at the Warm Distributional Edge: The Case of a Tidepool Shrimp.” *Journal of Experimental Marine Biology and Ecology* 545 (December): 151641.

Arendt, Detlev, Elia Benito-Gutierrez, Thibaut Brunet, and Heather Marlow. 2015. “Gastric Pouches and the Mucociliary Sole: Setting the Stage for Nervous System Evolution.” *Philosophical Transactions of the Royal Society B: Biological Sciences* 370 (1684): 20150286.

Atkins, Michael S., O. Roger Anderson, and Carl O. Wirsen. 1998. “Effect of Hydrostatic Pressure on the Growth Rates and Encystment of Flagellated Protozoa Isolated from a Deep-Sea Hydrothermal Vent and a Deep Shelf Region.” *Marine Ecology Progress Series* 171 (October): 85–95.

Balachandra, Shruthi, Sharanya Sarkar, and Amanda A. Amodeo. 2022. “The Nuclear-to-Cytoplasmic Ratio: Coupling DNA Content to Cell Size, Cell Cycle, and Biosynthetic Capacity.” *Annual Review of Genetics* 56 (November): 165–85.

Barr, I., and F. Guo. 2015. 'Pyridine Hemochromagen Assay for Determining the Concentration of Heme in Purified Protein Solutions', *Bio Protoc*, 5.

Barrere, Julien, Piyush Nanda, and Andrew W. Murray. 2023. “Alternating Selection for Dispersal and Multicellularity Favors Regulated Life Cycles.” *Current Biology* 33 (9): 1809-1817.e3.

Benabentos, Rocio, Shigenori Hirose, Richard Sucgang, Tomaz Curk, Mariko Katoh, Elizabeth A. Ostrowski, Joan E. Strassmann, et al. 2009. “Polymorphic Members of the Lag Gene Family Mediate Kin Discrimination in Dictyostelium.” *Current Biology* 19 (7): 567–72.

Biernaskie, Jay M., and Stuart A. West. 2015. “Cooperation, Clumping and the Evolution of Multicellularity.” *Proceedings of the Royal Society B: Biological Sciences* 282 (1813): 20151075.

Biggers, William J., Anthony Pires, Jan A. Pechenik, Eric Johns, Priyam Patel, Theresa Polson, and John Polson. 2012. 'Inhibitors of nitric oxide synthase induce larval settlement and metamorphosis of the polychaete annelidCapitella teleta', *Invertebrate Reproduction & Development*, 56: 1-13.

Bishop, C. D., and B. P. Brandhorst. 2003. 'On nitric oxide signaling, metamorphosis, and the evolution of biphasic life cycles', *Evol Dev*, 5: 542-50.

Bishop, C. D., and B. P. Brandhorst . 2007. 'Development of nitric oxide synthase-defined neurons in the sea urchin larval ciliary band and evidence for a chemosensory function during metamorphosis', *Dev Dyn*, 236: 1535-46.

Black, Andrew J., Pierrick Bourrat, and Paul B. Rainey. 2020. “Ecological Scaffolding and the Evolution of Individuality.” *Nature Ecology & Evolution* 4 (3): 426–36.

Bogdan, C. 2015. 'Nitric oxide synthase in innate and adaptive immunity: an update', *Trends Immunol*, 36: 161-78.

Bonner, J T. 1971. “Aggregation and Differentiation in the Cellular Slime Molds.” *Annual Review of Microbiology* 25 (1): 75–92.

Bonner, John Tyler. 1998. “The Origins of Multicellularity.” *Integrative Biology* 1 (1): 27–36.

Boon, E. M., S. H. Huang, and M. A. Marletta. 2005. 'A molecular basis for NO selectivity in soluble guanylate cyclase', *Nat Chem Biol*, 1: 53-9.

Boon, E. M., and M. A. Marletta. 2005. 'Ligand discrimination in soluble guanylate cyclase and the H-NOX family of heme sensor proteins', *Curr Opin Chem Biol*, 9: 441-6.

Booth, David S. and King, Nicole. 2020. "Genome editing enables reverse genetics of multicellular development in the choanoflagellate Salpingoeca rosetta." eLife: 9:e56193

Booth, David S., and King Nicole. 2022. “The History of Salpingoeca Rosetta as a Model for Reconstructing Animal Origins.” In *Current Topics in Developmental Biology*, 147:73–91.

Boraas, MARTIN E., DIANNE B. Seale, and JOSEPH E. Boxhorn. 1998. “Phagotrophy by a Flagellate Selects for Colonial Prey: A Possible Origin of Multicellularity.” *Evolutionary Ecology* 12 (2): 153–64.

Bowers, Blair, and Edward D. Korn. 1969. “THE FINE STRUCTURE OF ACANTHAMOEBA CASTELLANII (NEFF STRAIN) : II. Encystment.” *Journal of Cell Biology* 41 (3): 786–805.

Broersma, Cathleen, and Elizabeth A. Ostrowski. 2022. “Group Transformation: Fruiting Body and Stalk Formation.” In *The Evolution of Multicellularity*. CRC Press.

Broniowska, K. A., A. R. Diers, and N. Hogg. 2013. 'S-nitrosoglutathione', *Biochim Biophys Acta*, 1830: 3173-81.

Brown, Matthew W., Martin Kolisko, Jeffrey D. Silberman, and Andrew J. Roger. 2012. “Aggregative Multicellularity Evolved Independently in the Eukaryotic Supergroup Rhizaria.” *Current Biology: CB* 22 (12): 1123–27. https://doi.org/10.1016/j.cub.2012.04.021.

Brown, Matthew W., and Jeffrey D. Silberman. 2013. “The Non-Dictyostelid Sorocarpic Amoebae.” In *Dictyostelids*, edited by Maria Romeralo, Sandra Baldauf, and Ricardo Escalante, 219–42. Berlin, Heidelberg: Springer Berlin Heidelberg.

Brown, Matthew W., Frederick W. Spiegel, and Jeffrey D. Silberman. 2009. “Phylogeny of the ‘Forgotten’ Cellular Slime Mold, Fonticula Alba, Reveals a Key Evolutionary Branch within Opisthokonta.” *Molecular Biology and Evolution* 26 (12): 2699–2709.

Brunet, T., A. H. Fischer, P. R. Steinmetz, A. Lauri, P. Bertucci, and D. Arendt. 2016. 'The evolutionary origin of bilaterian smooth and striated myocytes', *Elife*, 5.

Brunet, Thibaut, Marvin Albert, William Roman, Maxwell C Coyle, Danielle C Spitzer, and Nicole King. 2021. "A Flagellate-to-Amoeboid Switch in the Closest Living Relatives of Animals." Edited by Patricia J Wittkopp, Iñaki Ruiz-Trillo, and Purificación López-García. *eLife* 10 (January): e61037.

Brunet, Thibaut, and David S. Booth. 2023. "Cell Polarity in the Protist-to-Animal Transition." In *Current Topics in Developmental Biology*, S0070215323000455. Elsevier.

Brunet, Thibaut, and Nicole King. 2017. "The Origin of Animal Multicellularity and Cell Differentiation." *Developmental Cell* 43 (2): 124–40.

Brunet, Thibaut and Nicole King. 2022. "The Single-Celled Ancestors of Animals: A History of Hypotheses." In *The Evolution of Multicellularity*, 1st ed. CRC Press. https://www.preprints.org/manuscript/202011.0302/v1.

Brunet, Thibaut, Ben T. Larson, Tess A. Linden, Mark J. A. Vermeij, Kent McDonald, and Nicole King. 2019. "Light-Regulated Collective Contractility in a Multicellular Choanoflagellate." *Science* 366 (6463): 326–34. https://doi.org/10.1126/science.aay2346.

Carr, M., B. S. C. Leadbeater, R. Hassan, M. Nelson, and S. L. Baldauf. 2008. "Molecular Phylogeny of Choanoflagellates, the Sister Group to Metazoa." *Proceedings of the National Academy of Sciences* 105 (43): 16641–46.

Carr, M., D. J. Richter, P. Fozouni, T. J. Smith, A. Jeuck, B. S. C. Leadbeater, and F. Nitsche. 2017. 'A six-gene phylogeny provides new insights into choanoflagellate evolution', *Mol Phylogenet Evol*, 107: 166-78.

Castresana, J. 2000. "Selection of Conserved Blocks from Multiple Alignments for Their Use in Phylogenetic Analysis." *Molecular Biology and Evolution* 17 (4): 540–52.

Cavalier-Smith, Thomas. 2017. "Origin of Animal Multicellularity: Precursors, Causes, Consequences—the Choanoflagellate/Sponge Transition, Neurogenesis and the Cambrian Explosion." *Philosophical Transactions of the Royal Society B: Biological Sciences* 372 (1713): 20150476.

Chen, Fenfen, Yanyan Xue, Nan Pan, Muhammad Zeeshan Bhatti, Tao Niu, and Jiwu Chen. 2018. "New Contribution to the Morphology and Molecular Mechanism of Euplotes Encysticus Encystment." *Scientific Reports* 8 (1): 12795.

Cheng, J., K. He, Z. Shen, G. Zhang, Y. Yu, and J. Hu. 2019. 'Nitric Oxide (NO)-Releasing Macromolecules: Rational Design and Biomedical Applications', *Front Chem*, 7: 530.

Cheung, B. H., F. Arellano-Carbajal, I. Rybicki, and M. de Bono. 2004. 'Soluble guanylate cyclases act in neurons exposed to the body fluid to promote C. elegans aggregation behavior', *Curr Biol*, 14: 1105-11.

Chin, Nicole E., Tiffany C. Wu, J. Michael O'Toole, Kevin Xu, Tom Hata, and Mimi A. R. Koehl. 2023. "Formation of Multicellular Colonies by Choanoflagellates Increases Susceptibility to Capture by Amoeboid Predators." *Journal of Eukaryotic Microbiology* 70 (3): e12961.

Colasanti, M., T. Persichini, and G. Venturini. 2010. 'Nitric oxide pathway in lower metazoans', *Nitric Oxide*, 23: 94-100.

Colasanti, M., G. Venturini, A. Merante, G. Musci, and G. M. Lauro. 1997. 'Nitric oxide involvement in Hydra vulgaris very primitive olfactory-like system', *J Neurosci*, 17: 493-9.

Comes, S., A. Locascio, F. Silvestre, M. d'Ischia, G. L. Russo, E. Tosti, M. Branno, and A. Palumbo. 2007. 'Regulatory roles of nitric oxide during larval development and metamorphosis in Ciona intestinalis', *Dev Biol*, 306: 772-84.

Corliss, John O., and Stephen C. Esser. 1974. “Comments on the Role of the Cyst in the Life Cycle and Survival of Free-Living Protozoa.” *Transactions of the American Microscopical Society* 93 (4): 578–93.

Cristino, L., V. Guglielmotti, A. Cotugno, C. Musio, and S. Santillo. 2008. 'Nitric oxide signaling pathways at neural level in invertebrates: functional implications in cnidarians', *Brain Res*, 1225: 17-25.

Curtis, Patrick D., Rion G. Taylor, Roy D. Welch, and Lawrence J. Shimkets. 2007. “Spatial Organization of Myxococcus Xanthus during Fruiting Body Formation.” *Journal of Bacteriology* 189 (24): 9126–30.

Davison, Ian R., and Gareth A. Pearson. 1996. “Stress Tolerance in Intertidal Seaweeds.” *Journal of Phycology* 32 (2): 197–211.

Dayel, Mark J., Rosanna A. Alegado, Stephen R. Fairclough, Tera C. Levin, Scott A. Nichols, Kent McDonald, and Nicole King. 2011. “Cell Differentiation and Morphogenesis in the Colony-Forming Choanoflagellate *Salpingoeca Rosetta*.” *Developmental Biology*, Experimental and historical aspects of evolutionary bioscience, 357 (1): 73–82.

Denninger, J. W., and M. A. Marletta. 1999. 'Guanylate cyclase and the .NO/cGMP signaling pathway', *Biochim Biophys Acta*, 1411: 334-50.

Derbyshire, E. R., and M. A. Marletta. 2009. 'Biochemistry of soluble guanylate cyclase', *Handb Exp Pharmacol*: 17-31.

Dereeper, A., V. Guignon, G. Blanc, S. Audic, S. Buffet, F. Chevenet, J.-F. Dufayard, et al. 2008. “Phylogeny.Fr: Robust Phylogenetic Analysis for the Non-Specialist.” *Nucleic Acids Research* 36 (Web Server issue): W465-469.

Di Ciano, Caterina, Zilin Nie, Katalin Szászi, Alison Lewis, Takehito Uruno, Xi Zhan, Ori D. Rotstein, Alan Mak, and András Kapus. 2002. “Osmotic Stress-Induced Remodeling of the Cortical Cytoskeleton.” *American Journal of Physiology-Cell Physiology* 283 (3): C850–65.

Doyle, M. P., and B. R. Duling. 1997. 'Acetylcholine induces conducted vasodilation by nitric oxide-dependent and -independent mechanisms', *Am J Physiol*, 272: H1364-71.

Dulce, R. A., V. Mayo, E. B. Rangel, W. Balkan, and J. M. Hare. 2015. 'Interaction between neuronal nitric oxide synthase signaling and temperature influences sarcoplasmic reticulum calcium leak: role of nitroso-redox balance', *Circ Res*, 116: 46-55.

Du, Qingyou, Yoshinori Kawabe, Christina Schilde, Zhi-hui Chen, and Pauline Schaap. 2015a. “The Evolution of Aggregative Multicellularity and Cell–Cell Communication in the Dictyostelia.” *Journal of Molecular Biology*, Cooperative Behaviour in Microbial Communities, 427 (23): 3722–33.

Du, Qingyou, Yoshinori Kawabe, Christina Schilde, Zhi-Hui Chen, and Pauline Schaap. 2015b. “The Evolution of Aggregative Multicellularity and Cell-Cell Communication in the Dictyostelia.” *Journal of Molecular Biology* 427 (23): 3722–33.

Dudin, Omaya, Andrej Ondracka, Xavier Grau-Bové, Arthur AB Haraldsen, Atsushi Toyoda, Hiroshi Suga, Jon Bråte, and Iñaki Ruiz-Trillo. 2019. “A Unicellular Relative of Animals Generates a Layer of Polarized Cells by Actomyosin-Dependent Cellularization.” Edited by Mukund Thattai, K VijayRaghavan, and Mukund Thattai. *eLife* 8 (October): e49801.

Elliott, G. R., and S. P. Leys. 2007. 'Coordinated contractions effectively expel water from the aquiferous system of a freshwater sponge', *J Exp Biol*, 210: 3736-48.
Elliott, G. R., and S. P. Leys. 2010. 'Evidence for glutamate, GABA and NO in coordinating behaviour in the sponge, Ephydatia muelleri (Demospongiae, Spongillidae)', *J Exp Biol*, 213: 2310-21.
Ellwanger, K., and M. Nickel. 2006. 'Neuroactive substances specifically modulate rhythmic body contractions in the nerveless metazoon Tethya wilhelma (Demospongiae, Porifera)', *Front Zool*, 3: 7.
Elsas, Jan Dirk van, Jack T. Trevors, Alexandre Soares Rosado, and Paolo Nannipieri. 2019. *Modern Soil Microbiology, Third Edition*. CRC Press.
Espinosa, Avelina, and Guillermo Paz-y-Miño-C. 2014. “Evidence of Taxa-, Clone-, and Kin-Discrimination in Protists: Ecological and Evolutionary Implications.” *Evolutionary Ecology* 28 (6): 1019–29.
Estephane, D., and M. Anctil. 2010. 'Retinoic acid and nitric oxide promote cell proliferation and differentially induce neuronal differentiation in vitro in the cnidarian Renilla koellikeri', *Dev Neurobiol*, 70: 842-52.
Fairclough, Stephen R., Zehua Chen, Eric Kramer, Qiandong Zeng, Sarah Young, Hugh M. Robertson, Emina Begovic, et al. 2013. “Premetazoan Genome Evolution and the Regulation of Cell Differentiation in the Choanoflagellate Salpingoeca Rosetta.” *Genome Biology* 14 (2): R15.
Fairclough, Stephen R., Mark J. Dayel, and Nicole King. 2010. “Multicellular Development in a Choanoflagellate.” *Current Biology* 20 (20): R875–76.
Fenchel, Tom. 2019. “Filter-Feeding in Colonial Protists.” *Protist* 170 (3): 283–86.
Ferrer-Bonet, Maria, and Iñaki Ruiz-Trillo. 2017. “Capsaspora Owczarzaki.” *Current Biology* 27 (17): R829–30.
Fisher, Roberta M., Charlie K. Cornwallis, and Stuart A. West. 2013. “Group Formation, Relatedness, and the Evolution of Multicellularity.” *Current Biology* 23 (12): 1120–25.
Froggett, S. J., and E. M. Leise. 1999. 'Metamorphosis in the Marine Snail Ilyanassa obsoleta, Yes or NO?', *Biol Bull*, 196: 57-62.
Fung L., A. Konkol, T. Ishikawa, B. T. Larson, T. Brunet, R. E. Goldstein. 2023. "Swimming, Feeding, and Inversion of Multicellular Choanoflagellate Sheets". Phys. Rev. Lett. (131): 168401.
Garbary, David. 2007. “The Margin of the Sea.” In *Algae and Cyanobacteria in Extreme Environments*, edited by Joseph Seckbach, 173–91. Cellular Origin, Life in Extreme Habitats and Astrobiology. Dordrecht: Springer Netherlands.
Gibbs, S. M., A. Becker, R. W. Hardy, and J. W. Truman. 2001. 'Soluble guanylate cyclase is required during development for visual system function in Drosophila', *J Neurosci*, 21: 7705-14.
Giovine, M., M. Pozzolini, A. Favre, G. Bavestrello, C. Cerrano, F. Ottaviani, L. Chiarantini, A. Cerasi, M. Cangiotti, E. Zocchi, S. Scarfi, M. Sara, and U. Benatti. 2001. 'Heat stress-activated, calcium-dependent nitric oxide synthase in sponges', *Nitric Oxide*, 5: 427-31.
Gray, J. M., D. S. Karow, H. Lu, A. J. Chang, J. S. Chang, R. E. Ellis, M. A. Marletta, and C. I. Bargmann. 2004. 'Oxygen sensation and social feeding mediated by a C. elegans guanylate cyclase homologue', *Nature*, 430: 317-22.

Gong, Zhi-Wei, Xin-Peng Fan, Rui Ma, and Bing Ni. 2018. “Ultrastructure of Vegetative Cells and Resting Cysts, and Live Observations of the Encystation and Excystation Processes in Diophrys Oligothrix Borror, 1965 (Protista, Ciliophora).” *Journal of Morphology* 279 (10): 1397–1407.

Grau-Bové, Xavier, Guifré Torruella, Stuart Donachie, Hiroshi Suga, Guy Leonard, Thomas A. Richards, and Iñaki Ruiz-Trillo. 2017. “Dynamics of Genomic Innovation in the Unicellular Ancestry of Animals.” *eLife* 6 (July): e26036.

Griffiths, A. J. 1969. “Encystment in Amoebae.” In *Advances in Microbial Physiology*, edited by A. H. Rose and J. F. Wilkinson, 4:105–29. Academic Press.

Grimes, Gary W. 1973. “Differentiation During Encystment and Excystment in Oxytricha Fallax*.” *The Journal of Protozoology* 20 (1): 92–104.

Grosberg, Richard K., and Richard R. Strathmann. 2007. “The Evolution of Multicellularity: A Minor Major Transition?” *Annual Review of Ecology, Evolution, and Systematics* 38 (1): 621–54.

Gruenheit, Nicole, Katie Parkinson, Balint Stewart, Jennifer A. Howie, Jason B. Wolf, and Christopher R. L. Thompson. 2017. “A Polychromatic ‘Greenbeard’ Locus Determines Patterns of Cooperation in a Social Amoeba.” *Nature Communications* 8 (1): 14171.

Guindon, Stéphane, Jean-François Dufayard, Vincent Lefort, Maria Anisimova, Wim Hordijk, and Olivier Gascuel. 2010. “New Algorithms and Methods to Estimate Maximum-Likelihood Phylogenies: Assessing the Performance of PhyML 3.0.” *Systematic Biology* 59 (3): 307–21.

Guindon, Stéphane, and Olivier Gascuel. 2003. “A Simple, Fast, and Accurate Algorithm to Estimate Large Phylogenies by Maximum Likelihood.” *Systematic Biology* 52 (5): 696–704.

H. James-Clark A. B. 1867. “IV. Conclusive Proofs of the Animality of the Ciliate Sponges, and of Their Affinities with the Infusoria Flagellata.” *Annals and Magazine of Natural History*, January.

Haag, C. R., M. Riek, J. W. Hottinger, V. I. Pajunen, and D. Ebert. 2006. “Founder Events as Determinants of Within-Island and among-Island Genetic Structure of Daphnia Metapopulations.” *Heredity* 96 (2): 150–58.

Haeckel, Ernst, and E. Perceval Wright F.L.S. 1874. “Memoirs: The Gastraea-Theory, the Phylogenetic Classification of the Animal Kingdom and the Homology of the Germ-Lamellæ.” *Journal of Cell Science* s2-14 (55): 223–47.

Hammerschmidt, Katrin, Caroline J. Rose, Benjamin Kerr, and Paul B. Rainey. 2014. “Life Cycles, Fitness Decoupling and the Evolution of Multicellularity.” *Nature* 515 (7525): 75–79.

Hehenberger, Elisabeth, Denis V. Tikhonenkov, Martin Kolisko, Javier Del Campo, Anton S. Esaulov, Alexander P. Mylnikov, and Patrick J. Keeling. 2017. “Novel Predators Reshape Holozoan Phylogeny and Reveal the Presence of a Two-Component Signaling System in the Ancestor of Animals.” *Current Biology: CB* 27 (13): 2043-2050.e6.

Herron, Matthew D., Joshua M. Borin, Jacob C. Boswell, Jillian Walker, I-Chen Kimberly Chen, Charles A. Knox, Margrethe Boyd, Frank Rosenzweig, and William C. Ratcliff. 2019. “De Novo Origins of Multicellularity in Response to Predation.” *Scientific Reports* 9 (1): 2328.

Hibberd, D. J. 1975. “Observations on the Ultrastructure of the Choanoflagellate Codosiga Botrytis (Ehr.) Saville-Kent with Special Reference to the Flagellar Apparatus.” *Journal of Cell Science* 17 (1): 191–219.

Hillyer, J. F., and T. Y. Estevez-Lao. 2010. 'Nitric oxide is an essential component of the hemocyte-mediated mosquito immune response against bacteria', *Dev Comp Immunol*, 34: 141-9.

Horst, B. G., and M. A. Marletta. 2018. 'Physiological activation and deactivation of soluble guanylate cyclase', *Nitric Oxide*, 77: 65-74.

Horst, B. G., E. M. Stewart, A. A. Nazarian, and M. A. Marletta. 2019. 'Characterization of a Carbon Monoxide-Activated Soluble Guanylate Cyclase from Chlamydomonas reinhardtii', *Biochemistry*, 58: 2250-59.

Horst, B. G., A. L. Yokom, D. J. Rosenberg, K. L. Morris, M. Hammel, J. H. Hurley, and M. A. Marletta. 2019. 'Allosteric activation of the nitric oxide receptor soluble guanylate cyclase mapped by cryo-electron microscopy', *Elife*, 8.

Huang, S. H., D. C. Rio, and M. A. Marletta. 2007. 'Ligand binding and inhibition of an oxygen-sensitive soluble guanylate cyclase, Gyc-88E, from Drosophila', *Biochemistry*, 46: 15115-22.

Huggett, J, and Cl Griffiths. 1986. “Some Relationships between Elevation, Physico-Chemical Variables and Biota of Intertidal Rock Pools.” *Marine Ecology Progress Series* 29: 189–97.

Jacklet, J. W. 1997. 'Nitric oxide signaling in invertebrates', *Invert Neurosci*, 3: 1-14.

James-Clark, H. 1868. 'XXII.—On the Spongiæ ciliatæ as Infusoria flagellata; or observations on the structure, animality, and relationship of Leucosolenia botryoides, Bowerbank', *Annals and Magazine of Natural History*, 1: 133-42.

Jeuck, Alexandra, Hartmut Arndt, and Frank Nitsche. 2014. “Extended Phylogeny of the Craspedida (Choanomonada).” *European Journal of Protistology* 50 (4): 430–43.

Keller, Evelyn F., and Lee A. Segel. 1970. “Initiation of Slime Mold Aggregation Viewed as an Instability.” *Journal of Theoretical Biology* 26 (3): 399–415.

Kessin, R H, G G Gundersen, V Zaydfudim, and M Grimson. 1996. “How Cellular Slime Molds Evade Nematodes.” *Proceedings of the National Academy of Sciences* 93 (10): 4857–61.

Khan, Naveed Ahmed, Junaid Iqbal, and Ruqaiyyah Siddiqui. 2015. “Stress Management in Cyst-Forming Free-Living Protists: Programmed Cell Death and/or Encystment.” *BioMed Research International* 2015 (January): e437534.

King, Nicole, M. Jody Westbrook, Susan L. Young, Alan Kuo, Monika Abedin, Jarrod Chapman, Stephen Fairclough, et al. 2008. “The Genome of the Choanoflagellate Monosiga Brevicollis and the Origin of Metazoans.” *Nature* 451 (7180): 783–88.

Kirkegaard, Julius B., and Raymond E. Goldstein. 2016a. “Filter-Feeding, near-Field Flows, and the Morphologies of Colonial Choanoflagellates.” *Physical Review E* 94 (5): 052401.

Kirkegaard, Julius B., and Raymond E. Goldstein. 2016b. “Filter-Feeding, near-Field Flows, and the Morphologies of Colonial Choanoflagellates.” *Physical Review E* 94 (5): 052401.

Kjerfve, Björn. 1998. “CARICOMP: Caribbean Coral Reef, Seagrass and Mangrove Sites.” https://policycommons.net/artifacts/9792097/caricomp/10696997/.

Kobayashi, S., H. Sadamoto, H. Ogawa, Y. Kitamura, K. Oka, K. Tanishita, and E. Ito. 2000. 'Nitric oxide generation around buccal ganglia accompanying feeding behavior in the pond snail, Lymnaea stagnalis', *Neurosci Res*, 38: 27-34.

Knoll, Andrew H. 2011. “The Multiple Origins of Complex Multicellularity.” *Annual Review of Earth and Planetary Sciences* 39 (1): 217–39.
Koehl, M. a. R. 2021. “Selective Factors in the Evolution of Multicellularity in Choanoflagellates.” *Journal of Experimental Zoology Part B: Molecular and Developmental Evolution* 336 (3): 315–26.
Komis, G., P. Apostolakos, and B. Galatis. 2002. “Hyperosmotic Stress-induced Actin Filament Reorganization in Leaf Cells of Chlorophyton Comosum.” *Journal of Experimental Botany* 53 (375): 1699–1710.
Kożyczkowska, Aleksandra, Sebastián R. Najle, Eduard Ocaña-Pallarès, Cristina Aresté, Victoria Shabardina, Patricia S. Ara, Iñaki Ruiz-Trillo, and Elena Casacuberta. 2021. “Stable Transfection in Protist *Corallochytrium Limacisporum* Identifies Novel Cellular Features among Unicellular Animals Relatives.” *Current Biology* 31 (18): 4104-4110.e5.
Kumler, William E., Justin Jorge, Paul M. Kim, Noama Iftekhar, and M. a. R. Koehl. 2020. “Does Formation of Multicellular Colonies by Choanoflagellates Affect Their Susceptibility to Capture by Passive Protozoan Predators?” *Journal of Eukaryotic Microbiology* 67 (5): 555–65.
Lamża, Łukasz. 2023. “Diversity of ‘Simple’ Multicellular Eukaryotes: 45 Independent Cases and Six Types of Multicellularity.” *Biological Reviews* 98 (6): 2188–2209.
Leadbeater, B. S. 1983a. 'Distribution and chemistry of microfilaments in choanoflagellates, with special reference to the collar and other tentacle systems', *Protistologica*, 19: 157-66.
Leadbeater, Barry S. C. 1983b. “Life-History and Ultrastructure of a New Marine Species of Proterospongia (Choanoflagellida).” *Journal of the Marine Biological Association of the United Kingdom* 63 (1): 135–60.
Leadbeater, Barry S.C. 2015. *The Choanoflagellates: Evolution, Biology and Ecology*. Cambridge: Cambridge University Press.
Leadbeater, Barry S. C., and Serguei A. Karpov. 2000. “Cyst Formation in a Freshwater Strain of the Choanoflagellate Desmarella Moniliformis Kent.” *Journal of Eukaryotic Microbiology* 47 (5): 433–39.
Lemoine, Frédéric, Damien Correia, Vincent Lefort, Olivia Doppelt-Azeroual, Fabien Mareuil, Sarah Cohen-Boulakia, and Olivier Gascuel. 2019. “NGPhylogeny.Fr: New Generation Phylogenetic Services for Non-Specialists.” *Nucleic Acids Research* 47 (W1): W260–65.
L’Etoile, Nathan J., and Christina King-Smith. 2020. “Rosette Colonies of Choanoflagellates (Salpingoeca Rosetta) Show Increased Food Vacuole Formation Compared with Single Swimming Cells.” *Journal of Eukaryotic Microbiology* 67 (2): 263–67.
Letunic, I., and P. Bork. 2021. 'Interactive Tree Of Life (iTOL) v5: an online tool for phylogenetic tree display and annotation', *Nucleic Acids Res*, 49: W293-W96.
Li, Rubiao, Neundorf, Ines, Nitsche Frank. 2018. "First Efficient Transfection in Choanoflagellates using Cell-Penetrating Peptides." bioRxiv: 10.1101/260190.
Li, Si I., and Michael D. Purugganan. 2011. “The Cooperative Amoeba: Dictyostelium as a Model for Social Evolution.” *Trends in Genetics* 27 (2): 48–54.
Li, Yuqing, Yurui Wang, Shijing Zhang, Xyrus X. Maurer-Alcalá, and Ying Yan. 2022. “How Ciliated Protists Survive by Cysts: Some Key Points During Encystment and Excystment.” *Frontiers in Microbiology* 13.

Little, Colin, and J. A. Kitching. 1996. *The Biology of Rocky Shores*. Oxford University Press. Lord, S. J., K. B. Velle, R. D. Mullins, and L. K. Fritz-Laylin. 2020. 'SuperPlots: Communicating reproducibility and variability in cell biology', *J Cell Biol*, 219.

Márquez-Zacarías, Pedro, Peter L. Conlin, Kai Tong, Jennifer T. Pentz, and William C. Ratcliff. 2021. "Why Have Aggregative Multicellular Organisms Stayed Simple?" *Current Genetics* 67 (6): 871–76.

Marshall, Wyth L., and Mary L. Berbee. 2011. "Facing Unknowns: Living Cultures (*Pirum Gemmata* Gen. Nov., Sp. Nov., and *Abeoforma Whisleri*, Gen. Nov., Sp. Nov.) from Invertebrate Digestive Tracts Represent an Undescribed Clade within the Unicellular Opisthokont Lineage Ichthyosporea (Mesomycetozoea)." *Protist* 162 (1): 33–57.

Mendoza, Alex de, Hiroshi Suga, Jon Permanyer, Manuel Irimia, and Iñaki Ruiz-Trillo. 2015. "Complex Transcriptional Regulation and Independent Evolution of Fungal-like Traits in a Relative of Animals." Edited by Alejandro Sánchez Alvarado. *eLife* 4 (October): e08904.

Miano, J. M., X. Long, and K. Fujiwara. 2007. 'Serum response factor: master regulator of the actin cytoskeleton and contractile apparatus', *Am J Physiol Cell Physiol*, 292: C70-81.

Michod, Richard E. 2007. "Evolution of Individuality during the Transition from Unicellular to Multicellular Life." *Proceedings of the National Academy of Sciences of the United States of America* 104 Suppl 1 (May): 8613–18.

Mizuno, Kouhei, Mais Maree, Toshihiko Nagamura, Akihiro Koga, Satoru Hirayama, Soichi Furukawa, Kenji Tanaka, and Kazuya Morikawa. 2022. "Novel Multicellular Prokaryote Discovered next to an Underground Stream." *eLife* 11 (October): e71920.

Moroz, L. L., and A. B. Kohn. 2011. 'Parallel evolution of nitric oxide signaling: diversity of synthesis and memory pathways', *Front Biosci (Landmark Ed)*, 16: 2008-51.

Moroz, L. L., R. W. Meech, J. V. Sweedler, and G. O. Mackie. 2004. 'Nitric oxide regulates swimming in the jellyfish Aglantha digitale', *J Comp Neurol*, 471: 26-36.

Moroz, L. L., T. P. Norekian, T. J. Pirtle, K. J. Robertson, and R. A. Satterlie. 2000. 'Distribution of NADPH-diaphorase reactivity and effects of nitric oxide on feeding and locomotory circuitry in the pteropod mollusc, Clione limacina', *J Comp Neurol*, 427: 274-84.

Moroz, L. L., J. H. Park, and W. Winlow. 1993. 'Nitric oxide activates buccal motor patterns in Lymnaea stagnalis', *Neuroreport*, 4: 643-6.

Moroz, L. L., D. Y. Romanova, M. A. Nikitin, D. Sohn, A. B. Kohn, E. Neveu, F. Varoqueaux, and D. Fasshauer. 2020. 'The diversification and lineage-specific expansion of nitric oxide signaling in Placozoa: insights in the evolution of gaseous transmission', *Sci Rep*, 10: 13020.

Musser, J. M., K. J. Schippers, M. Nickel, G. Mizzon, A. B. Kohn, C. Pape, P. Ronchi, N. Papadopoulos, A. J. Tarashansky, J. U. Hammel, F. Wolf, C. Liang, A. Hernandez-Plaza, C. P. Cantalapiedra, K. Achim, N. L. Schieber, L. Pan, F. Ruperti, W. R. Francis, S. Vargas, S. Kling, M. Renkert, M. Polikarpov, G. Bourenkov, R. Feuda, I. Gaspar, P. Burkhardt, B. Wang, P. Bork, M. Beck, T. R. Schneider, A. Kreshuk, G. Worheide, J. Huerta-Cepas, Y. Schwab, L. L. Moroz, and D. Arendt. 2021. 'Profiling cellular diversity in sponges informs animal cell type and nervous system evolution', *Science*, 374: 717-23.

Mylnikov, Alexander P., Denis V. Tikhonenkov, Sergey A. Karpov, and Claudia Wylezich. 2019. “Microscopical Studies on *Ministeria Vibrans* Tong, 1997 (Filasterea) Highlight the Cytoskeletal Structure of the Common Ancestor of Filasterea, Metazoa and Choanoflagellata.” *Protist* 170 (4): 385–96.

Nagy, László G., Torda Varga, Árpád Csernetics, and Máté Virágh. 2020. “Fungi Took a Unique Evolutionary Route to Multicellularity: Seven Key Challenges for Fungal Multicellular Life.” *Fungal Biology Reviews* 34 (4): 151–69.

Nguyen, Ngoc Minh, Tatiana Merle, Florence Broders, Anne-Christine Brunet, Florian Sarron, Aditya Jha, Jean-Luc Genisson, Eric Rottinger, and Emmanuel Farge. 2020. "Evolutionary Emergence of First Animal Organisms Triggered by Environmental Mechano-Biochemical Marine Stimulation", *bioRxiv*: 2020.12.03.407668.

Nickel, M., C. Scheer, J. U. Hammel, J. Herzen, and F. Beckmann. 2011. 'The contractile sponge epithelium sensu lato--body contraction of the demosponge Tethya wilhelma is mediated by the pinacoderm', *J Exp Biol*, 214: 1692-8.

Nielsen, Claus. 2008. “Six Major Steps in Animal Evolution: Are We Derived Sponge Larvae?” *Evolution & Development* 10 (2): 241–57.

Ocaña-Pallarès, Eduard, Tom A. Williams, David López-Escardó, Alicia S. Arroyo, Jananan S. Pathmanathan, Eric Bapteste, Denis V. Tikhonenkov, Patrick J. Keeling, Gergely J. Szöllősi, and Iñaki Ruiz-Trillo. 2022. “Divergent Genomic Trajectories Predate the Origin of Animals and Fungi.” *Nature* 609 (7928): 747–53.

Ogawa, Takumi, Koyama, Shuji, Toshihiro, Omori, and Kikuchi, Kenji. 2024. "The Architecture of Sponge Choanocyte Chambers Maximizes Mechanical Pumping Efficiency", *bioRxiv*: 2024.02.22.581376.

Pentz, Jennifer T, Kathryn MacGillivray, James G DuBose, Peter L Conlin, Emma Reinhardt, Eric Libby, and William C Ratcliff. 2023. “Evolutionary Consequences of Nascent Multicellular Life Cycles.” *eLife* 12 (October): e84336.

Pentz, Jennifer T., Pedro Márquez-Zacarías, G. Ozan Bozdag, Anthony Burnetti, Peter J. Yunker, Eric Libby, and William C. Ratcliff. 2020. “Ecological Advantages and Evolutionary Limitations of Aggregative Multicellular Development.” *Current Biology* 30 (21): 4155-4164.e6.

Pettitt, Michala E., Belinda A. A. Orme, John R. Blake, and Barry S. C. Leadbeater. 2002. “The Hydrodynamics of Filter Feeding in Choanoflagellates.” *European Journal of Protistology* 38 (4): 313.

Pichugin, Yuriy, Hye Jin Park, and Arne Traulsen. 2019. “Evolution of Simple Multicellular Life Cycles in Dynamic Environments.” *Journal of The Royal Society Interface* 16 (154): 20190054.

Pirtle, T. J., and R. A. Satterlie. 2021. 'Cyclic Guanosine Monophosphate Modulates Locomotor Acceleration Induced by Nitric Oxide but not Serotonin in Clione limacina Central Pattern Generator Swim Interneurons', *Integr Org Biol*, 3: obaa045.

Queller, David C., Eleonora Ponte, Salvatore Bozzaro, and Joan E. Strassmann. 2003. “Single-Gene Greenbeard Effects in the Social Amoeba Dictyostelium Discoideum.” *Science* 299 (5603): 105–6.

Rai, K. K., N. Pandey, and S. P. Rai. 2020. 'Salicylic acid and nitric oxide signaling in plant heat stress', *Physiol Plant*, 168: 241-55.

Reess, Max, and Carl Fisch. 1887. *Untersuchungen über bau und Lebensgeschichte der Hirschtrüffel, Elaphomyces*. T. Fischer.

Reyes-Rivera, Josean, Yang Wu, Benjamin G.H. Guthrie, Michael A. Marletta, Nicole King, and Thibaut Brunet. 2022. "Nitric Oxide Signaling Controls Collective Contractions in a Colonial Choanoflagellate." *Current Biology* 32 (11): 2539-2547.e5.

Richter, Daniel J., and Nicole King. 2013. "The Genomic and Cellular Foundations of Animal Origins." *Annual Review of Genetics* 47 (1): 509–37.

Richter, D. J., P. Fozouni, M. B. Eisen, and N. King. 2018. 'Gene family innovation, conservation and loss on the animal stem lineage', *Elife*, 7.

Riisgård, Hans U., Kelay, Rachael A., Goldstein, Josephine, Brewer, Jonathan R., Solovyeva, Vita, Frunch, Peter. 2023. "Choanocyte dimensions and pumping rates in the demosponge Halichondria panicea."*J Exp Mar Bio and Eco* 569: 151957.

Rivero, Francisco, Bernd Köppel, Barbara Peracino, Salvatore Bozzaro, Florian Siegert, Cornelis J. Weijer, Michael Schleicher, Richard Albrecht, and Angelika A. Noegel. 1996. "The Role of the Cortical Cytoskeleton: F-Actin Crosslinking Proteins Protect against Osmotic Stress, Ensure Cell Size, Cell Shape and Motility, and Contribute to Phagocytosis and Development." *Journal of Cell Science* 109 (11): 2679–91.

Robertson, H. M. 2009. 'The choanoflagellate Monosiga brevicollis karyotype revealed by the genome sequence: telomere-linked helicase genes resemble those of some fungi', *Chromosome Res*, 17: 873-82.

Roper, Marcus, Mark J. Dayel, Rachel E. Pepper, and M. a. R. Koehl. 2013. "Cooperatively Generated Stresslet Flows Supply Fresh Fluid to Multicellular Choanoflagellate Colonies." *Physical Review Letters* 110 (22): 228104.

Ros-Rocher, Núria, and Thibaut Brunet. 2023. "What Is It like to Be a Choanoflagellate? Sensation, Processing and Behavior in the Closest Unicellular Relatives of Animals." *Animal Cognition* 26 (6): 1767–82.

Ros-Rocher, Núria, Ria Q. Kidner, Catherine Gerdt, W. Sean Davidson, Iñaki Ruiz-Trillo, and Joseph P. Gerdt. 2023. "Chemical Factors Induce Aggregative Multicellularity in a Close Unicellular Relative of Animals." *Proceedings of the National Academy of Sciences* 120 (18): e2216668120.

Ros-Rocher, Núria, Alberto Pérez-Posada, Michelle M. Leger, and Iñaki Ruiz-Trillo. 2021. "The Origin of Animals: An Ancestral Reconstruction of the Unicellular-to-Multicellular Transition." *Open Biology* 11 (2): 200359.

R Core Team. n.d. "R: A Language and Environment for Statistical Computing. Vienna, Austria: R Foundation for Statistical Computing." *R Foundation for Statistical Computing*. https://www.R-project.org/.

S.a, Karpov, and Coupe S.j. 1998. "A Revision of Choanoflagellate Genera Kentrosiga Schiller, 1953 and Desmarella Kent, 1880." *Acta Protozoologica* 1 (37).

Sauer, Karin, Paul Stoodley, Darla M. Goeres, Luanne Hall-Stoodley, Mette Burmølle, Philip S. Stewart, and Thomas Bjarnsholt. 2022. "The Biofilm Life Cycle: Expanding the Conceptual Model of Biofilm Formation." *Nature Reviews Microbiology* 20 (10): 608–20.

Saville-Kent, William. 1880. *A Manual of the Infusoria : Including a Description of All Known Flagellate, Ciliate, and Tentaculiferous Protozoa, British and Foreign, and an Account of the Organization and the Affinities of the Sponges*. London: D. Bogue.

Schaap, Pauline, and Christina Schilde. 2018. “Encystation: The Most Prevalent and Underinvestigated Differentiation Pathway of Eukaryotes.” *Microbiology* 164 (5): 727–39.

Schindelin, Johannes, Ignacio Arganda-Carreras, Erwin Frise, Verena Kaynig, Mark Longair, Tobias Pietzsch, Stephan Preibisch, et al. 2012a. “Fiji: An Open-Source Platform for Biological-Image Analysis.” *Nature Methods* 9 (7): 676–82.

Sebé-Pedrós, Arnau, Manuel Irimia, Javier del Campo, Helena Parra-Acero, Carsten Russ, Chad Nusbaum, Benjamin J Blencowe, and Iñaki Ruiz-Trillo. 2013. “Regulated Aggregative Multicellularity in a Close Unicellular Relative of Metazoa.” Edited by Diethard Tautz. *eLife* 2 (December): e01287.

Shah, Hiral, Marine Olivetta, Chandni Bhickta, Paolo Ronchi, Monika Trupinić, Eelco C. Tromer, Iva M. Tolić, Yannick Schwab, Omaya Dudin, and Gautam Dey. 2023. “Life Cycle-Coupled Evolution of Mitosis in Close Relatives of Animals.” Preprint. Cell Biology.

Simion, P., H. Philippe, D. Baurain, M. Jager, D. J. Richter, A. Di Franco, B. Roure, N. Satoh, E. Queinnec, A. Ereskovsky, P. Lapebie, E. Corre, F. Delsuc, N. King, G. Worheide, and M. Manuel. 2017. 'A Large and Consistent Phylogenomic Dataset Supports Sponges as the Sister Group to All Other Animals', *Curr Biol*, 27: 958-67.

Short, Martin B., Cristian A. Solari, Sujoy Ganguly, Thomas R. Powers, John O. Kessler, and Raymond E. Goldstein. 2006. “Flows Driven by Flagella of Multicellular Organisms Enhance Long-Range Molecular Transport.” *Proceedings of the National Academy of Sciences* 103 (22): 8315–19.

Smith, B. C., and M. A. Marletta. 2012. 'Mechanisms of S-nitrosothiol formation and selectivity in nitric oxide signaling', *Curr Opin Chem Biol*, 16: 498-506.

Smith, Jeff, Joan E. Strassmann, and David C. Queller. 2016. “Fine-Scale Spatial Ecology Drives Kin Selection Relatedness among Cooperating Amoebae.” *Evolution* 70 (4): 848–59.

Song, H., O. H. Hewitt, and S. M. Degnan. 2021. 'Arginine Biosynthesis by a Bacterial Symbiont Enables Nitric Oxide Production and Facilitates Larval Settlement in the Marine-Sponge Host', *Curr Biol*, 31: 433-37 e3.

Sriram, K., J. G. Laughlin, P. Rangamani, and D. M. Tartakovsky. 2016. 'Shear-Induced Nitric Oxide Production by Endothelial Cells', *Biophys J*, 111: 208-21.

Stanley, Steven M. 1973. “An Ecological Theory for the Sudden Origin of Multicellular Life in the Late Precambrian.” *Proceedings of the National Academy of Sciences* 70 (5): 1486–89.

Staps, Merlijn, Jordi Van Gestel, and Corina E. Tarnita. 2019. “Emergence of Diverse Life Cycles and Life Histories at the Origin of Multicellularity.” *Nature Ecology & Evolution* 3 (8): 1197–1205.

Staps, Merlijn, Jordi Van Gestel, and Corina E. Tarnita. 2022. “Life Cycles as a Central Organizing Theme for Studying Multicellularity.” In *The Evolution of Multicellularity*. CRC Press.

Stein, Friedrich. 1859. *Der Organismus Der Infusionsthiere*. Leipzig: W. Engelmann. https://doi.org/10.5962/bhl.title.3933.

Stoupin, Daniel, Aron K. Kiss, Hartmut Arndt, Anastasia V. Shatilovich, David A. Gilichinsky, and Frank Nitsche. 2012. “Cryptic Diversity within the Choanoflagellate Morphospecies

Complex *Codosiga Botrytis* – Phylogeny and Morphology of Ancient and Modern Isolates." *European Journal of Protistology* 48 (4): 263–73.
Strassmann, J. E., Y. Zhu, and D. C. Queller. 2000. "Altruism and Social Cheating in the Social Amoeba Dictyostelium Discoideum." *Nature* 408 (6815): 965–67.
Stratford, Malcolm. 1992. "Lectin-Mediated Aggregation of Yeasts — Yeast Flocculation." *Biotechnology and Genetic Engineering Reviews* 10 (1): 283–342.
Suga, Hiroshi, and Iñaki Ruiz-Trillo. 2013. "Development of Ichthyosporeans Sheds Light on the Origin of Metazoan Multicellularity." *Developmental Biology* 377 (1): 284–92.
Tang, Si, Yuriy Pichugin, and Katrin Hammerschmidt. 2023. "An Environmentally Induced Multicellular Life Cycle of a Unicellular Cyanobacterium." *Current Biology* 33 (4): 764-769.e5.
Tarnita, Corina E., Clifford H. Taubes, and Martin A. Nowak. 2013. "Evolutionary Construction by Staying Together and Coming Together." *Journal of Theoretical Biology* 320 (March): 10–22.
Tikhonenkov, Denis V., Kirill V. Mikhailov, Elisabeth Hehenberger, Sergei A. Karpov, Kristina I. Prokina, Anton S. Esaulov, Olga I. Belyakova, et al. 2020. "New Lineage of Microbial Predators Adds Complexity to Reconstructing the Evolutionary Origin of Animals." *Current Biology* 30 (22): 4500-4509.e5.
Tomankova, S., P. Abaffy, and R. Sindelka. 2017. 'The role of nitric oxide during embryonic epidermis development of Xenopus laevis', *Biol Open*, 6: 862-71.
Tong, Kai, G Ozan Bozdag, and William C Ratcliff. 2022. "Selective Drivers of Simple Multicellularity." *Current Opinion in Microbiology* 67 (June): 102141.
Toret, Christopher, Andrea Picco, Micaela Boiero-Sanders, Alphee Michelot, and Marko Kaksonen. 2022. "The Cellular Slime Mold *Fonticula Alba* Forms a Dynamic, Multicellular Collective While Feeding on Bacteria." *Current Biology* 32 (9): 1961-1973.e4.
Torruella, Guifré, Alex de Mendoza, Xavier Grau-Bové, Meritxell Antó, Mark A. Chaplin, Javier del Campo, Laura Eme, et al. 2015. "Phylogenomics Reveals Convergent Evolution of Lifestyles in Close Relatives of Animals and Fungi." *Current Biology: CB* 25 (18): 2404–10.
Trunk, Thomas, Hawzeen S. Khalil, and Jack C. Leo. 2018. "Bacterial Autoaggregation." *AIMS Microbiology* 4 (1): 140–64. https://doi.org/10.3934/microbiol.2018.1.140.
Ueda, N., and S. M. Degnan. 2013. 'Nitric oxide acts as a positive regulator to induce metamorphosis of the ascidian Herdmania momus', *PLoS One*, 8: e72797.
Ueda, N., G. S. Richards, B. M. Degnan, A. Kranz, M. Adamska, R. P. Croll, and S. M. Degnan. 2016. 'An ancient role for nitric oxide in regulating the animal pelagobenthic life cycle: evidence from a marine sponge', *Sci Rep*, 6: 37546.
Velicer, Gregory J., Lee Kroos, and Richard E. Lenski. 2000. "Developmental Cheating in the Social Bacterium Myxococcus Xanthus." *Nature* 404 (6778): 598–601.
Velicer, Marco La Fortezza, Kaitlin A. Schaal, Gregory J. 2022. "Group Formation: On the Evolution of Aggregative Multicellularity." In *The Evolution of Multicellularity*. CRC Press.
Venter, Paul Christiaan, Frank Nitsche, and Hartmut Arndt. 2018. "The Hidden Diversity of Flagellated Protists in Soil." *Protist* 169 (3): 432–49.
Verni, F., and G. Rosati. 2011. "Resting Cysts: A Survival Strategy in Protozoa Ciliophora." *Italian Journal of Zoology* 78 (2): 134–45.

West, S. A., A. S. Griffin, and A. Gardner. 2007. “Social Semantics: Altruism, Cooperation, Mutualism, Strong Reciprocity and Group Selection.” *Journal of Evolutionary Biology* 20 (2): 415–32.

Woznica, Arielle, Kumar, Ashwani, Sturge, Carolyn R, Xing, Chao, King, Nicole, Pfeiffer, Julie K. 2021. "STING mediates immune responses in the closest living relatives of animals." eLife 10:e70436.

Yabumoto, T., F. Takanashi, Y. Kirino, and S. Watanabe. 2008. 'Nitric oxide is involved in appetitive but not aversive olfactory learning in the land mollusk Limax valentianus', *Learn Mem*, 15: 229-32.

Zhang, L., Q. Liu, X. Yuan, T. Wang, S. Luo, H. Lei, and Y. Xia. 2013. 'Requirement of heat shock protein 70 for inducible nitric oxide synthase induction', *Cell Signal*, 25: 1310-7.

Zhang, X., and R. H. Cote. 2005. 'cGMP signaling in vertebrate retinal photoreceptor cells', *Front Biosci*, 10: 1191-204.

Zhao, Y., P. E. Brandish, M. Di Valentin, J. P. Schelvis, G. T. Babcock, and M. A. Marletta. 2000. 'Inhibition of soluble guanylate cyclase by ODQ', *Biochemistry*, 39: 10848-54.